

UNIVERSITY OF GENOVA
Department of Civil, Chemical and Environmental
Engineering

PhD Thesis

Mixing Processes in Compound Channel

Author:

Sonia Angiolani

Supervisors:

Dr. Alessandro Stocchino

Dr. Giovanni Besio

External Referee:

Prof. Ian Guymer

*Doctoral School in Science and Technology for Engineering
Phd in Fluid Dynamics and Processes of Environmental Engineering*

March 20th 2014

Abstract

The aim of the present work is the study of turbulence and mixing processes in river flows applying a two-dimensional analysis, focussing, in particular, on processes of transport of momentum and mass. The latter will be investigated in a Lagrangian framework. The analysis of mixing processes that occur in a uniform compound channel are described starting from an experimental investigation based on Particle Image Velocimetry (PIV) analysis of free-surface velocities. The experimental campaign has been made to reveal the fundamental features of the flow characterizing a straight compound channel and forms the basis for an investigation of the dynamics of two-dimensional large-scale vortices with vertical axis evolving under quasi-uniform flow conditions. Dynamical properties are found strongly dependent on the ratio r_h between the main channel flow depth (h_{mc}) and the floodplain depth (h_{fp}), and three flow classes can be identified, namely “Shallow Flows” ($r_h > 3$), “Intermediate Flows” ($2 \leq r_h \leq 3$) and “Deep Flows” ($r_h < 2$). “Shallow flows” are dominated by strong shearing and large macro-vortices populating a transitional region between the main channel and the floodplains. The mean streamwise velocity induced in “Intermediate flows” is characterized by a dip in the transition region, while it closely resembles that occurring in a rectangular channel in the case of “Deep flows”. For both the latter cases the shear in the transition region decreases and the macro-vortices are also generated in the wall boundary layer of the floodplains.

In the second stage, starting from time-resolved Eulerian surface velocity fields, a Lagrangian analysis of the dispersive processes that occur in compound channels when the controlling physical parameters, i.e. the flow depth ratio (r_h) and the Froude number (Fr) are changed, is performed. Lagrangian mixing is studied by means of various approaches based either on single particle or multiple particle statistics (relative and absolute statistics and probability density functions of relative displacements). Absolute statistics reveal that transitional macro-vortices, typical of shallow flow conditions, strongly

influence the growth in time of the absolute dispersion, after the initial ballistic regime, leading to a non-monotonic behaviour. In deep flow conditions, on the contrary, the absolute dispersion displays a monotonic growth due to the fact that the generation of transitional macro-vortices does not take place. Multiple-particle dynamics is controlled by r_h and Fr . Different growth regimes of the relative diffusivity have been found depending on the flow conditions.

Finally, the large-time asymptotic behavior of the mixing characteristics is analyzed in terms of the absolute diffusivity, in order to characterize typical values of longitudinal and transversal diffusivity coefficients.

Contents

Abstract	iii
List of Figures	vii
List of Tables	xiii
1 Compound channel flow	1
1.1 Introduction	1
1.2 Conceptual models	4
1.2.1 Integral model	4
1.2.2 Shear layer analysis	6
1.2.3 Hydrodynamic stability analysis	8
1.3 Experimental investigations	10
1.4 Outline of the Thesis	13
2 Mixing in 2D turbulence	15
2.1 Theory	15
2.1.1 Formulation of the problem: the conservation equations	15
2.1.2 Quadratic invariants	17
2.1.3 Velocity spectra: the enstrophy cascade and the inverse energy cascade	17
2.2 Absolute and relative dispersion	20
2.2.1 Single-particle statistics	21
2.2.2 Multiple-particle statistics	24
2.3 Conclusions	27
3 The experiments	29
3.1 Experimental set-up	29
3.1.1 PIV system	34
3.2 Experimental approach: the Particle Image Velocimetry system	35
3.2.1 Fundamental principles of PIV	36
3.2.2 Image recording techniques	38

3.2.3	Post-processing of PIV data	39
4	PIV results : experimental observation of Eulerian Flow fields	45
4.1	Mean Flow velocity profiles	45
4.1.1	2D velocity fields	45
4.1.2	Mean streamwise velocity profiles	46
4.2	Main properties of the macro-vortices	48
4.2.1	Vortex identification	48
4.2.2	Main features of the macro-vortices	54
5	Lagrangian statistics	61
5.1	Absolute properties	61
5.1.1	Time scales and growth law	62
5.1.2	Absolute dispersion and diffusivity	64
5.2	Relative properties	67
5.2.1	Shallow flows	67
5.2.2	Intermediate flows	73
5.2.3	Deep flows	77
6	Mixing characteristics	81
6.1	Previous laboratory experiments and state of the art	81
6.1.1	Transverse mixing coefficient	83
6.1.2	Longitudinal mixing coefficient	85
6.2	Transverse and Longitudinal Diffusivity	86
6.2.1	Zonal diffusivities for main channel and floodplains	90
6.2.2	Global diffusivities for the whole channel	93
7	Conclusion	103
A	Lagrangian and Eulerian integral quantities of the whole set of experiments	109
	Bibliography	115
	Acknowledgements	123

List of Figures

1.1	Flow structures in a compound channel [Shiono and Knight, 1991].	3
1.2	Large scale vortices observed at the transition region between the main channel and the floodplains of a compound channel [Sellin, 1964].	3
1.3	Divided Channel Method : example of a cross section of a compound channel divided in subsection.	5
1.4	Top view of the shallow flow facility used by van Prooijen and Uijttewaal [2002], large coherent structures are visualized by dye injection.	6
1.5	Velocity profiles modelled by a (a) hyperbolic-tangent function and by a (d) hyperbolic-secant function analysed by Chu et al. [1991];the velocity profiles are created varying friction coefficient (b, e) or by varying depth (c, f).	9
1.6	Sketch of the equivalent bore built by Soldini et al. [2004]. . .	10
1.7	Sketch of the original flow condition occurring in a compound channel (upper panel) and equivalent mound of water (lower panel) [Soldini et al., 2004].	10
1.8	General view of SERC Flood Channel Facility [Knight and Shiono, 1990].	11
1.9	Structures in a compound channel [Nezu and Nakagawa, 1997].	13
2.1	The energy spectrum in 2D turbulence. β indicates the injected flux, k_d is wavenumber and the wavenumber k_E is characteristic of the spectrum maximum.	18
2.2	Steps of the vortex merging process shown by Melander et al. [1988].	19
3.1	Cross-section of the compound channel.	29
3.2	General view of the DICCA compound channel flume.	30
3.3	Sketch of the cross section of the flume.	30
3.4	Cathetometer used to measure bed longitudinal slope and channel inlet.	31

3.5	(a)High-speed digital camera and (b)sketch of digital camera and lighting system.	34
3.6	Example of recorded image.	35
3.7	Pictorial sketch of a generic PIV system.	37
3.8	Modes of particles image density:(a)Low density, (b)Mean density, (c)High density, from Raffel et al. [1998].	37
3.9	Single frame recording technique, from Raffel et al. [1998].	38
3.10	Multi frame recording technique, from Raffel et al. [1998].	39
3.11	Cross-correaltion function on the cross correlation plane, from Raffel et al. [1998].	42
4.1	2D free-surface velocity field for (from top to bottom) : (a)“Shallow Flows”($r_h = 3.43$, $Fr = 0.46$) , (b)“Intermediate Flows”($r_h = 2.39$, $Fr = 0.54$), (c)“Deep Flows”($r_h = 1.76$, $Fr = 0.58$). $V3$ indicates the time-averaged velocity.	47
4.2	Mean streamwise surface velocity (a) and turbulence intensity (b,c,d) for different value of r_h	49
4.3	Left: velocity fluctuation by galilean decomposition $u'(x, y, t) = u(x, y, t) - \overline{u(t)}$ and swirling strength for “Shallow Flows” (panel (a)), “Intermediate Flows” (panel (c)) and “Deep Flows” (panel (e)) . Right: the corresponding vorticity field (panels(b,d,f)).	50
4.4	Examples of 2D maps of the positive Hua and Kline eigenvalue λ_+^* : (a) Shallow flow conditions (EXP201, $r_h = 4.16$, $Fr = 0.60$), (b) Intermediate flow conditions (EXP205, $r_h = 2.04$, $Fr = 0.76$) and (c) Deep flow conditions (EXP112, $r_h = 1.28$, $Fr = 0.142$). The dotted-white lines indicate the transition regions of the compound channel. For the Deep flow the contour range has been reduced.	53
4.5	Swirling strength of a single vortex core with maximum Radius R_{max} and inclination angle θ	55
4.6	PDFs of macro-vortex size and shape. PDF of the equivalent radius R_{eq} , vortex eccentricity ϵ and the alignment angle θ for different depth ratios.	56
4.7	Top panel: normalized mean vortex radius R_{eq} over normalized downstream distance $x[-]$ for all discharges and experiments of van Prooijen and Uijttewaal [2002] Bottom panel: Shear layer thickness δ as a function of discharge Q and downstream distance x	58
5.1	Eulerian and Lagrangian kinetic energy (respectively E_E^* and E_L^*) for Shallow flows (panel a: EXP101 ($r_h = 3.69$, $Fr = 0.88$); panel c: EXP201 ($r_h = 4.16$, $Fr = 0.60$)) and Deep flows (panels b: EXP213 ($r_h = 1.68$, $Fr = 0.82$); panel d: EXP112 ($r_h = 1.28$, $Fr = 0.14$)).	63

5.2	Autocorrelation for: (a) Shallow flows (EXP201, $r_h = 4.16$, $Fr = 0.60$) and (b) Deep flows (EXP112, $r_h = 1.28$, $Fr = 0.14$).	63
5.3	a) Absolute dispersion; b) Absolute diffusivity. EXP201: $Fr = 0.6$, $r_h = 4.16$; EXP205: $Fr = 0.69$, $r_h = 5.57$; EXP112: $Fr = 0.14$, $r_h = 1.28$.	65
5.4	Plots of $A_x^{(2)}$, $A_y^{(2)}$, $K_x^{(1)}$ and $K_y^{(1)}$ for the Shallow flow of EXP201, panels a) and b), and for the Deep flow EXP112, panels c) and d).	68
5.5	Relative diffusivity as function of the dimensionless separation r for Shallow flow conditions ($r_h > 3$): a) EXP101; b) EXP201.	69
5.6	Contours of the Okubo-Weiss eigenvalue λ_0 showing vortex merging in the case of a Shallow flow (EXP201, $r_h = 4.16$, $Fr = 0.60$). Merging events are highlighted by solid ellipses and occur around $(x, y) = (1, -1)$ and $(x, y) = (9, 1)$ at two subsequent times, panels a) and c), and around $(x, y) = (3, 1)$ and $(x, y) = (13, 1)$ at two subsequent times, panels b) and d). The dotted-black lines indicate the transition regions of the compound channel. Note that only negative values of λ_0 have been displayed.	70
5.7	Normalized Eulerian Power Spectral Density function S_u corresponding to the Shallow flows experiments of figure 5.5.	71
5.8	Top: kurtosis of different initial relative separations (r_0) as function of time. The dash-dotted line indicates the value of the kurtosis for a Gaussian distribution, i.e. $ku = 3$. Bottom: PDF of relative displacements for dimensionless time ($t = 2$). Shallow flow (EXP201).	72
5.9	Finite Scale Lyapunov Exponents (FSLEs) for Shallow flow conditions	73
5.10	Relative diffusivity as a function of the dimensionless separation r for Intermediate conditions ($2 < r_h < 3$) in different regimes: a) subcritical flows, $Fr < 1$ (EXP205) and b) supercritical flows, $Fr > 1$ (EXP12).	74
5.11	Normalized Eulerian Power Spectral Density function S_u corresponding to the Intermediate flow experiments of figure 5.10.	75
5.12	Subcritical (case EXP205) and supercritical (case EXP12) Intermediate flows. First (subcritical flow) and third (supercritical flow) panels: kurtosis of different initial relative separations (r_0) as function of time. The dash-dotted line indicates the value of the kurtosis for a Gaussian distribution, i.e. $ku = 3$. Second (subcritical flow) and fourth (supercritical flow) panels: PDFs of relative displacements for dimensionless time ($t = 2$).	76

5.13	Finite Scale Lyapunov Exponents (FSLEs) for Intermediate flow conditions. a) Subcritical flow ($Fr < 1$); b) Supercritical flow $Fr > 1$	77
5.14	Relative diffusivity as a function of the dimensionless separation r for Deep conditions ($r_h < 2$) in different regimes. Panel a) subcritical flows ($Fr < 1$) EXP112; panel b) supercritical flows ($Fr > 1$) EXP17.	77
5.15	Finite Scale Lyapunov Exponents (FSLEs) for Deep flow conditions. a) Subcritical flow ($Fr < 1$); b) Supercritical flow $Fr > 1$	78
5.16	Normalized Eulerian Power Spectral Density function S_u corresponding to Deep flows experiments of figure 5.14.	79
5.17	Subcritical (case EXP213) and supercritical (case EXP17) Deep flows. First (subcritical flow) and third (supercritical flow) panels: kurtosis of different initial relative separations (r_0) as function of time. The dash-dotted line indicates the value of the kurtosis for a Gaussian distribution, i.e. $ku = 3$. Second (subcritical flow) and fourth (supercritical flow) panels: PDFs of relative displacements for dimensionless time ($t = 2$).	80
6.1	Single-particle statistics for experiment 503, shallow-flow conditions. Absolute dispersion and absolute diffusivity, panel (a) and panel (b) respectively.	89
6.2	Single-particle statistics for experiment 509, deep-flow conditions. Absolute dispersion and absolute diffusivity, panel (a) and panel (b) respectively.	89
6.3	Single particle statistics for experiment 511, deep-flow conditions. Absolute dispersion, panel (a) and absolute diffusivity, panel (b).	90
6.4	Dependence of the dimensionless absolute diffusivity $K_y^{*(1)}/u_S^*R^*$ on r_h for data collected in the main channel, (a) and floodplains (b). Lines indicate linear regression of the data.	91
6.5	Dependence of the dimensionless absolute diffusivity $K_x^{*(1)}/u_S^*R^*$ on r_h for data collected in the main channel (a) and floodplains (b). Lines indicate linear regression of the data.	91
6.6	Dependence of the dimensionless absolute diffusivity $K_y^{*(1)}/u_S^*R^*$ on Fr for data collected in the main channel (a) and floodplains (b). Lines indicate linear regression of the data.	92
6.7	Dependence of the dimensionless absolute diffusivity $K_x^{*(1)}/u_S^*R^*$ on Fr for data collected in the main channel (a) and floodplains (b). Lines indicate linear regression of the data.	92
6.8	Distribution of the dimensionless absolute diffusivity $K_x^{*(1)}/u_S^*R^*$ in the $(r_h; Fr)$ -parameter space.	94

6.9	Distribution of the dimensionless absolute diffusivity $K_y^{*(1)}/u_S^*R^*$ in the $(r_h; Fr)$ -parameter space.	95
6.10	Dependence of the dimensionless absolute diffusivity $K_y^{*(1)}/u_S^*R^*$ on r_h (a) and Fr (b). Lines indicate linear regression of the data.	96
6.11	Dependence of the dimensionless absolute diffusivity $K_x^{*(1)}/u_S^*R^*$ on r_h (a) and Fr (b). Lines indicate linear regression of the data.	97
6.12	Dependence of the ratio $K_x^{*(1)}/K_y^{*(1)}$ on the flow depth ratio r_h . Gray shaded zone indicates intermediate flow conditions.	98
6.13	Dependence of $K_x^{*(1)}/u_S^*R^*$ on Fr , compared with available literature results.	98
6.14	Dependence of $K_y^{*(1)}/u_S^*R^*$ on Fr , compared with available literature results. Gray markers: previous works, (empty for rectangular channel, fill for compound channels). Black markers: present campaign.	99

List of Tables

3.1	Main experimental parameters	33
6.1	Experimental measurements of absolute diffusivity coefficients	89
A.1	Relevant Lagrangian and Eulerian integral quantities of the whole set of experiments	110

Chapter 1

Compound channel flow

1.1 Introduction

In riverine and watercourse management it is very important to understand and, possibly, predict the transport and mixing processes of contaminants, nutrients and, eventually, fine sediments. The preservation and the defence of wildlife and environmental values in natural streams is strongly dependent on the capability of modeling and analysing the ecological impact of accidental spills or industrial dumping. Recent rapid developments in modeling water quality allowed a better description and a deeper understanding of pollutant behaviour. The analysis of mixing processes in natural streams is not a simple task as flow dynamics is strongly affected by channel irregularities.

Indeed, natural rivers and artificial channels not only commonly exhibit an irregular planar configuration, but they are also often characterized by complex cross-stream sections composed of a deep main central channel and shallow floodplains. These types of channels are commonly classified as “compound channels”. The typical geometry of compound channels is such that the topography has a sharp discontinuity in the transition region between the main channel and the floodplains.

The understanding of mixing and transport processes is of particular interest for this configuration: in natural streams floodplains are often wetlands with abundant wildlife and the knowledge of the mass transport processes is

vital to preserve the environmental conditions. Related fundamental issues are both the estimate of the water discharge under flood conditions and the prediction of the overbank front speed during short duration floods.

The flow velocity in the floodplains is lower than in the main channel, due to the water shallowness and to the high bed roughness in often more vegetation-covered areas. As a result of the velocity gradient, shearing occurs at the interface between the main channel and the floodplains, leading to various flow patterns most of which are characterized by large-scale vortical structures with vertical axes (macro-vortices).

Mixing and transport processes of solutes in compound channels are mainly controlled and regulated by the exchange of mass and momentum between the main channel and the lateral floodplains. Coherent structures are commonly recognized as major agents of mass transport (e.g. pollutants, nutrients), also owing to their ability to trap mass and to inhibit exchanges among different flow regions. Interesting reviews on this subject are those of Provenzale [1999], Boffetta et al. [2001] and LaCasce [2008].

Uniform compound channel flows are often studied using the conceptual scheme of Shiono and Knight [1991] (see figure 1.1 for a graphical illustration of the flow). Although the overall flow is, in general, a complex 3D turbulent flow, in a wide range of shallow free surface flows two-dimensional coherent structures with a length scale greater than the water depth are observed (see a.o. Socolofsky and Jirka [2004]). Secondary flows are, usually, disregarded since they have a major effect in a confined region, close to the bottom, of the main channel. For this reason many authors have chosen to apply a two-dimensional analysis based on the shallow-water approximation [Nezu et al., 1999, Sellin, 1964, Shiono and Knight, 1991, van Prooijen and Uijttewaai, 2002].

Among studies on the evolution of quasi-two-dimensional vortices with vertical axes (macro-vortices) in compound channels important are those of Sellin [1964], Shiono and Knight [1991] and Nezu et al. [1999] (see figure 1.2). The different mechanisms that may lead to the production of vorticity in shallow streams and, ultimately, macro-vortices have been recently described by Jirka [2001] and Nikora et al. [2007].

Among them, the topographic forcing that imposes an abrupt gradient in

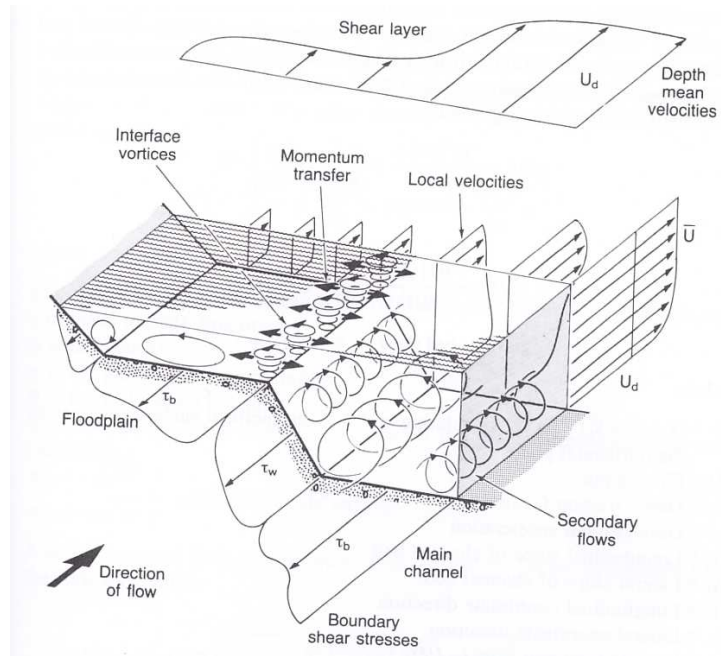


FIGURE 1.1: Flow structures in a compound channel [Shiono and Knight, 1991].

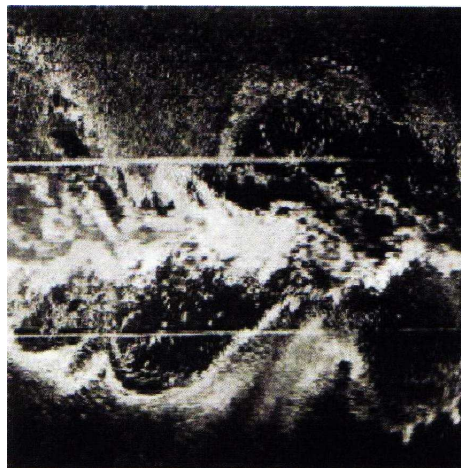


FIGURE 1.2: Large scale vortices observed at the transition region between the main channel and the floodplains of a compound channel [Sellin, 1964].

the flow evolution has been recognized as the main agent for the generation of macro-vortices. In the same vein Soldini et al. [2004], using the classic shallow-water approach (details of such simulation will be provided in the next section), have illustrated the mechanism by which depth discontinuities at the transition between the main channel and the floodplains are able to produce potential vorticity and, thus, sustain the generation of macro-vortices. As suggested by Nezu et al. [1999] and verified by Stocchino and Brocchini [2010], the dynamics of the flow field and, hence, of the vorticity, strongly depends on the flow characteristics in terms of the flow-depth ratio r_h , between the depth in the main channel (h_{mc}^*) and the depth in the floodplains (h_{fp}^*) as first introduced by Shiono and Knight [1991] and later modified by Nezu et al. [1999], and on the flow regime (Froude number).

1.2 Conceptual models

In this section some of the conceptual models used to study the evolution of macro-vortices, mentioned in the previous section, are briefly described. Since the early works by Sellin [1964], great efforts have been made to investigate compound channel flow and several computational models have been proposed. These models can be classified as:

- Integral models;
- Shear layer models;
- Hydrodynamic stability models.

1.2.1 Integral model

Until recently very simple conceptual models have been used to analyse compound channel flows and further works are based on so-called “*integral models*”.

The estimation of the stage-discharge relationship in compound channels is

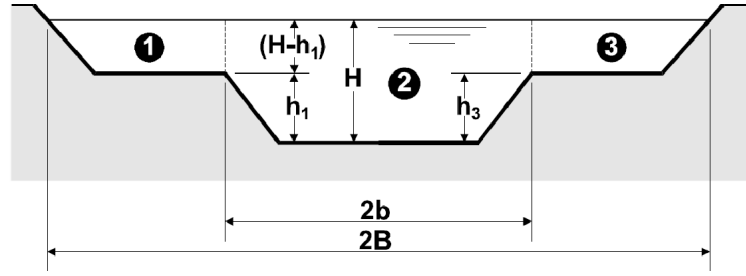


FIGURE 1.3: Divided Channel Method : example of a cross section of a compound channel divided in subsection.

based on the Divided Channel Method (DCM) that assumes steady and uniform flow. The method divides the channel cross-section in subsections where the velocities are more homogeneous (see figure 1.3 for cross-section subdivision). The whole section discharge is then obtained by addition of the subsection discharges, using the empirical Manning formula :

$$Q = \sum_i Q_i = \sum_i \frac{A_i R_i^{2/3}}{n_i} S_0^{1/2}, \quad (1.1)$$

where Q is the discharge, A is the sub-section area, R is the sub-section hydraulic radius, n is the Manning roughness coefficient, S_0 is the channel bed slope and subscript i stands for subsection i .

Various works have tried to improve and correct the Divided Channel Method and also some alternative methods have been proposed. Several studies have been based on the investigation of the relationship between the stage-discharge curve and the bed shear stress τ_b distribution in a compound channel section (a.o. Knight and Hamed [1984], Myers and Elsayy [1975]). On the basis of bed shear-stress measurements, Myers [1978] and Stephenson and Kolovopoulos [1990] defined an empirical apparent shear stress τ_a acting on the vertical division line between the main channel and the floodplain and performed a momentum balance analysis of subsection as defined by the Divided Channel Method. Several empirical relationships which link the apparent shear-stress to cross-section parameters were proposed, but such a perspective, only adequate for steady-state conditions and based on an integral modelling, is being replaced by an approach for which the major agents of transport of mass and momentum are the discrete flow structures defined

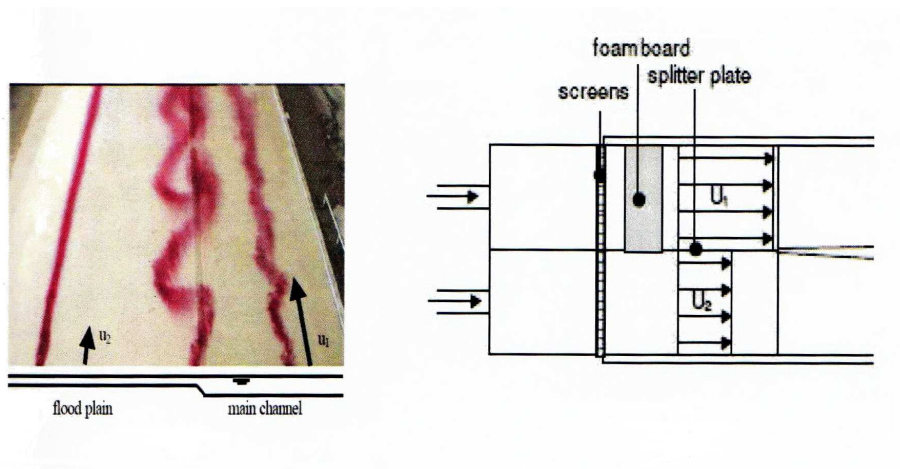


FIGURE 1.4: Top view of the shallow flow facility used by van Prooijen and Uijttewaal [2002], large coherent structures are visualized by dye injection.

as macro-vortices.

1.2.2 Shear layer analysis

A common theoretical approach used to describe uniform compound channel flows relies on the apparent close similarity between the flow at the “transition” and the flow generated at the interfaces of two free shallow streams with different velocities. [e.g. van Prooijen and Uijttewaal, 2002]. Such a similarity is based on the evidence that for both these configurations it is possible to use the same sort of stability analysis and also that mean velocity profiles can be, in both cases, well described by bell-shaped functions (e.g. hyperbolic-tangent/secant). The study of van Prooijen and Uijttewaal [2002] analyse the development of large horizontal structures in a shallow mixing layer. The results are validated with experimental data obtained from two different experiments (see figure 1.4) one concerning the development of a mixing layer downstream of the confluence of two flows of different velocity and the second the characteristics of a mixing layer between river and floodplains in a compound channel. The experiments clearly showed in both configuration the presence of the mixing layer and the large scale horizontal structures. A careful comparison reveals a difference between the behaviour

of large scale structures of mixing layers in shallow flow and in deep flow: in deep flow the large structures dissipate their energy through an energy cascade, in shallow flow the dissipation would be inhibited by the insufficient presence of intermediate turbulence scales due to the small depth.

Similarities and differences between flow characterizing a straight compound channel and a true free shear flow were pointed out by Stocchino and Brocchini [2010]. In this respect, a first difference is made evident by the non-monotonic behaviour of the mean streamwise velocity characterizing the fully-developed flow. Hence, bell-type function, typically used as self-similar solutions for free shear layers Chu et al. [1991], van Prooijen and Uijttewaai [2002], is inadequate to represent the mean flow in a compound channel.

Moreover, although horizontal mixing is governed by the quasi-2D macro-vortices in both flows, differences were expected, because the vortical structures of the two flows seem to have rather different properties. Such a difference was appreciated by observing the downstream growth of quasi-two-dimensional macro-vortices generated at the transition region of a compound channel and those measured in free shear flows by van Prooijen and Uijttewaai [2002]. While the former ones have a size almost constant, the latter ones grow in size at a considerable rate. This is consistent with the fact that the thickness of a free shear layer is expected to grow linearly in the streamwise direction, whereas in the case of compound channels it remains constant, as soon as the flow is fully developed. This is a reflection of the fundamental fact that the size of compound-channel macro-vortices scales with the crossflow size of the transition region, [Piattella et al., 2006, Soldini et al., 2004] whereas shear-layer macro-vortices scale with the shear layer width that increases downstream of the inception [van Prooijen and Uijttewaai, 2002]. Moreover, macro-vortices are also found to reside in different spatial regions in the two flows. In the case of a free shear layer the vortex position, coinciding with that of the shear layer, is seen to bend towards the low-velocity region of the shear layer [van Prooijen and Uijttewaai, 2002]. On the contrary, in a compound channel, not only the lateral walls provide an extra agent for vortex generation (mainly confined over the floodplains), but

also transition-region macro-vortices are found to reside over the transition region only.

1.2.3 Hydrodynamic stability analysis

The hydrodynamic stability analysis has been used by several authors to study the development of horizontal macro-vortices. The main purpose of this analysis is to determine the conditions under which a small perturbation of the basic flow can grow or can decay. Stability curves as function of parameters of the basic flow, define stable flows and unstable flows. Chu et al. [1991] first developed a model of stability analysis for an inviscid flow in a compound channel. Stability calculations were carried out using a linear theory for four groups of transverse shear flows (see figure 1.5). The bed friction number and the ambient-velocity parameter (depending on changes in depth and roughness across the open channel flow) were identified as the dimensionless parameters governing the stability of these groups of transverse shear flows. The stability calculation shown as, for a weak transverse shear flow, the bed friction number becomes the only dimensionless parameter governing the stability of the flow. Chu et al. [1991] used the rigid-lid assumption and thus did not allow for gravity waves to exist, thus an improvement of the analysis was proposed by Ghidaoui and Kolyshkin [1999]. This work removed the rigid-lid assumption from the study of linear stability of transverse shear flows in shallow open channels. Computational results have shown that the rigid-lid assumption is very good for weak shear flows and small Froude numbers but tends to overestimate the instability boundary. In addition, this work investigated the sensitivity of the size and shape of the stability domain of transverse shear flow in shallow waters to Froude number, Reynolds number, the velocity and length scales of velocity profile of basic flow and the type of resistance formula. This work also indicated that the size of the stability domain is strongly affected by the velocity, length scales and shape of the base velocity profile.

The generation and the evolution of large-scale eddies at the boundaries between the main channel and the floodplain were investigated by Soldini et al. [2004]. Channel flows were studied within the framework of the nonlinear

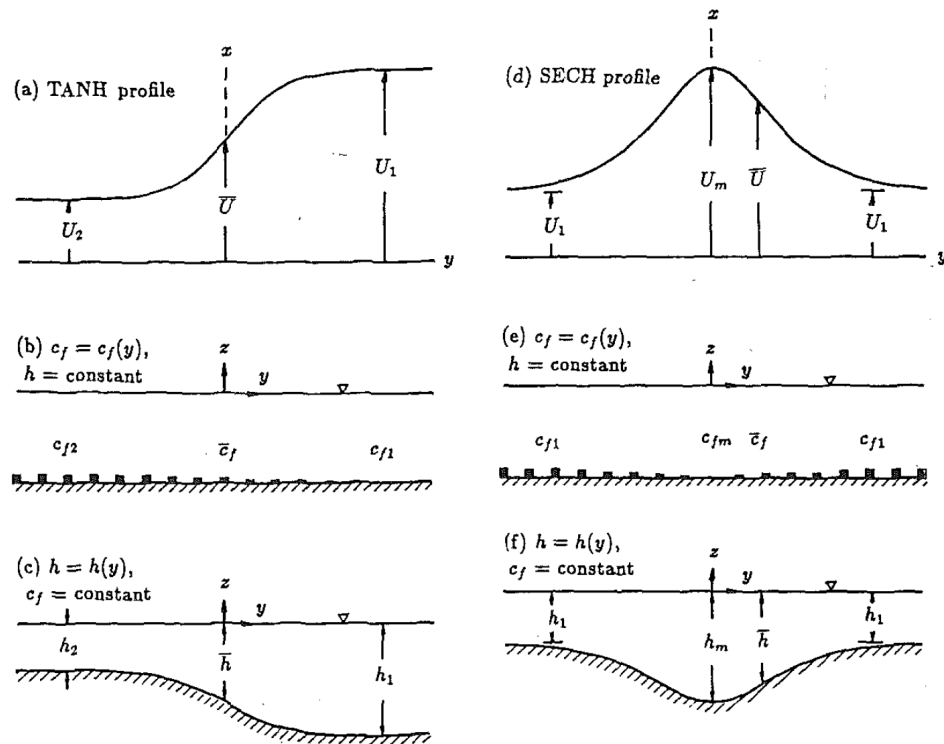


FIGURE 1.5: Velocity profiles modelled by a (a) hyperbolic-tangent function and by a (d) hyperbolic-secant function analysed by Chu et al. [1991]; the velocity profiles are created varying friction coefficient (b, e) or by varying depth (c, f).

shallow water equation (NSWE). Macro-vortices could be seen as pseudo-inviscid features of the NSWE which arise in the presence of discontinuous flow properties. In order to activate a generation mechanism of vorticity they assumed that a shock of straight, finite front propagates in the transverse direction of the cross-section of the channel flow. The unstable current is compared to an equivalent bore, i.e. to a breaking wave which injects in the flow the same amount of vorticity of an unstable current crossing the jump in depth at the transition region (see figure 1.6). To build such equivalent the original flow condition (upper panel of figure 1.7) was replaced with such a mound of water (lower panel of 1.7).

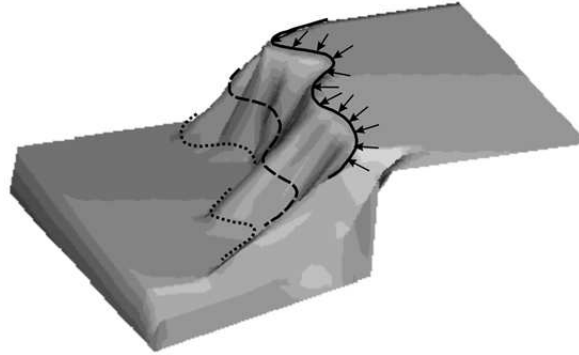


FIGURE 1.6: Sketch of the equivalent bore built by Soldini et al. [2004].

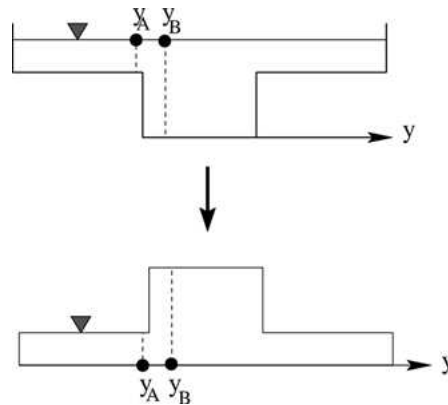


FIGURE 1.7: Sketch of the original flow condition occurring in a compound channel (upper panel) and equivalent mound of water (lower panel) [Soldini et al., 2004].

1.3 Experimental investigations

A great deal of experimental work has been undertaken in order to understand the structure of turbulent flows in compound open channel. In this section a briefly review of the main experimental campaigns is presented.

The first example of experimental facility that allowed experiments to be performed at large scale and for high Reynolds numbers was built by the U.K. Science and Engineering Research Council (SERC). The structure, named Flood Channel Facility (FCF), settled at Hydraulics Research Ltd., Wallingford [Knight and Sellin, 1987] and is shown in figure 1.8. The facility represents a large scale model of a river system with floodplains, it is 56 m long

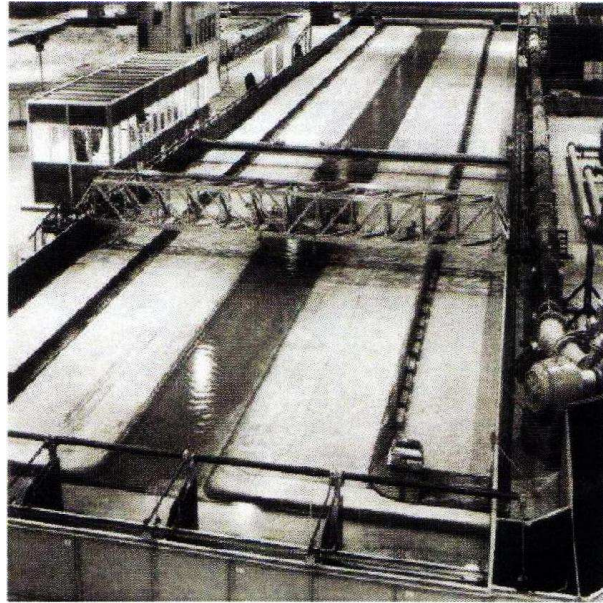


FIGURE 1.8: General view of SERC Flood Channel Facility [Knight and Shiono, 1990].

and 10 m wide, with a bed slope $S_0 = 10^{-3}$ and a maximum discharge of $1.08\text{m}^3/\text{s}$. In this channel were performed several experimental campaigns involving variation of floodplains width, floodplains roughness, main channel bank transverse slope and the number of floodplains. Among others Wormleaton and Merrett [1990] have analysed in detail the bed shear stress distribution, Myers and Brennan [1990] have studied the roughness coefficient variation when the river begins to flow overbank. Knight and Shiono [1990] focussed on measurements of local velocity, distribution of turbulence intensity, kinetic energy and Reynolds stresses in the region of transverse variation in depth, using a LDA (Laser Doppler Anemometer) system. The vertical distribution of primary velocity, defined as the ratio between the main velocity and the local bed shear velocity U/u_* , was found to be logarithmic in regions where the lateral shear stresses were low. On the contrary in regions where there was high shear, i.e. in the transition region between main channel and floodplains, the distribution of Reynolds stresses appeared highly non linear. In the transition region considerable temporal variations in local velocity and lateral shear stresses were observed, which produced large vortices with vertical axis that transfers momentum from the main channel and the floodplain.

In the last decades various experimental campaigns have been devoted to the analysis of the mixing processes focussing on the effects of the presence of floodplains on the mixing coefficients. These previous laboratory experiments will be treated in more detail in Chapter 6 in order to compare our analysis with results presented by these studies. The first attempt to analyze dispersion and diffusion processes due to composite sections, such as those of compound channels, was made by Wood and Liang [1989] employed the measurements performed for a rectangular channel by Nokes and Wood [1988] to compare an eigenvalue-eigenfunction solution for the dispersion of effluent in a compound-like channel with some experimental data of solute dispersion performed by Wood and Liang [1989] themselves. The same kind of approach has been followed by Spence et al. [1997] and Spence et al. [1998]. These investigated the transverse mixing of solute and suspended sediment within a trapezoidal compound channel under river flood conditions, focusing on the influence of the large scale horizontal eddies generated in the transition region between main channel and floodplains. The experimental campaign made by Fraselle et al. [2008] investigated fine sediment transport and deposition in a compound channel flume in order to analyse sediment exchanges between main channel and floodplains. The transverse mixing in a compound channel was also studied by Zeng et al. [2008]. In this work the estimation of lateral mixing coefficients was based on the measurement of turbulent velocity and solute concentration in a trapezoidal compound channel divided in different sub-section (main channel, side slope and floodplain).

Concerning the analysis of vortices, Sellin [1964] was the first to observe the effect of the large periodical structure at the surface of a compound channel flow. The presence of large vortices at the transition region has been identified through the use of aluminium powder scattered on the water surface and a camera (see figure 1.2). Meyer and Rehme [1994] experimentally investigated turbulent flow of air through compound rectangular channels, measuring axial mean velocity, wall shear stresses and Reynolds stresses. The most interesting result was the existence of a quasi-periodic large-scale turbulence structure

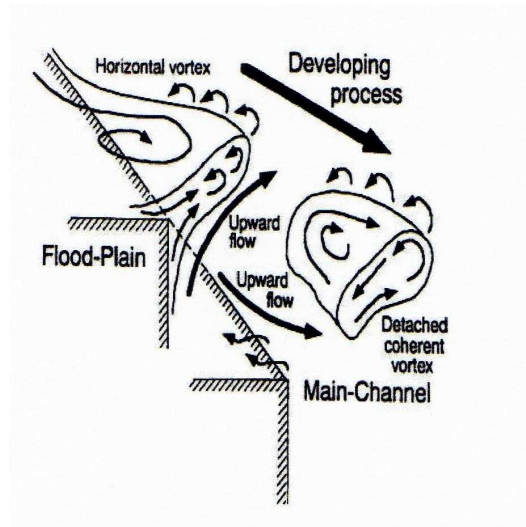


FIGURE 1.9: Structures in a compound channel [Nezu and Nakagawa, 1997].

in most of the geometries investigated. This structure was found stationary and independent of the axial position in the channel. In the study of Nezu and Nakagawa [1997] time-averaged structures of secondary currents were revealed experimentally by making use of Laser Doppler Anemometer (LDA) and the Particle Tracking Velocimetry (PTV). They investigated evolutionary patterns of horizontal large-scale vortices and clarified the interaction mechanism between the mainchannel and flood-plains induced by coherent vortices, called the intermittent upward secondary currents and the large-scale horizontal vortices, as shown in figure 1.9.

1.4 Outline of the Thesis

The main aim of this research is to analyse mixing processes which occur in a straight compound channel, through the results of a dedicated experimental campaign. The present work can be divided into three main parts. In a first stage the attention is dedicated to the study of the characteristics of the Eulerian turbulent flow that occurs in a compound channel from the inception to the fully developed flow conditions. Specific focus is on investigating the

dynamics of two-dimensional large-scale vortices with vertical axis generated at the transition region between main channel and floodplain.

In a second stage the Lagrangian properties of the flow are analyzed in details, studying both the single- and multiple-particle statistics, with the aim to describe the mixing regimes associated to the different flow conditions (sub- and super-critical regimes; deep, intermediate and shallow flows).

Finally, the large time asymptotic behaviour of the mixing characteristics is analyzed in terms of the absolute diffusivity in order to estimate typical values of longitudinal and transversal mixing coefficients, highlighting their dependence on the main physical parameters (the Froude number Fr and the flow depth ratio r_h).

The thesis is structured as follows:

Chapters 2 provides an overview on the fundamental mathematical issues related with the 2D turbulent theory and the results of absolute and relative dispersion of particles advected in a turbulent flow.

In **Chapter 3** the experimental set-up is described. In this chapter we provide also a short presentation of the general features of the experimental apparatus and of the mathematical concepts that are used in a generic PIV analysis.

In **Chapter 4** the analysis of both the specific features of macro-vortices and of the related mean flow characteristics is reported.

Chapter 5 is dedicated to the analysis of the Lagrangian mixing characteristic for different conditions described by the values of the main physical parameters.

Chapter 6 provides the evaluation of the mixing coefficients for uniform flows evolving in open compound channel. The results are then compared with several literature studies on flow dispersion.

Conclusions of the thesis are given in **Chapter 7**.

Chapter 2

Mixing in 2D turbulence

2.1 Theory

2.1.1 Formulation of the problem: the conservation equations

The evolution of the system in 2D turbulence is governed by the Navier-Stokes and continuity equations which read

$$\frac{\partial \mathbf{u}}{\partial t} + (\mathbf{u} \cdot \nabla) \mathbf{u} = -\frac{1}{\rho} \nabla p + \mathbf{f}_{\mathbf{u}} + \nu \nabla^2 \mathbf{u} \quad (2.1)$$

$$\nabla \cdot \mathbf{u} = 0 \quad (2.2)$$

where $\mathbf{u}(\mathbf{x}, t) = (u(x, y), v(x, y))$ is the velocity whose components are u, v in the x, y directions respectively, p is the pressure, ρ is the density, $\mathbf{f}_{\mathbf{u}}$ is the forcing term, ν is the molecular viscosity and ∇ is the operator defined by $\left(\frac{\partial}{\partial x}, \frac{\partial}{\partial y}\right)$.

The other fundamental law for the system is the equation of mechanical power, which is obtained starting from the Navier-Stokes equations (2.1) and written in indicial form reads:

$$\frac{\partial u_i}{\partial t} + u_j \frac{\partial u_i}{\partial x_j} = -\frac{1}{\rho} \frac{\partial p}{\partial x_i} + f_i + \nu \nabla^2 u_i \quad (2.3)$$

multiplied by u_i

$$\frac{1}{2} \frac{\partial}{\partial t} u_i^2 + \frac{1}{2} u_j \frac{\partial}{\partial x_j} u_i^2 = -\frac{1}{\rho} u_i \frac{\partial p}{\partial x_i} + u_i f_i + \nu u_i \nabla^2 u_i, \quad (2.4)$$

which in vectorial form becomes, for the incompressibility condition (equation 2.2):

$$\frac{d}{dt} \left(\frac{\mathbf{u}^2}{2} \right) = -\nabla \cdot \left(\frac{p\mathbf{u}}{\rho} \right) + \mathbf{u} \cdot \mathbf{f} + \nu \mathbf{u} \cdot \nabla^2 \mathbf{u}. \quad (2.5)$$

The third fundamental law is the equation of the evolution of the enstrophy (i.e. squared vorticity), which is obtained starting from the vorticity equation:

$$\frac{\partial \boldsymbol{\omega}}{\partial t} + \mathbf{u} \cdot \nabla \mathbf{u} = \boldsymbol{\omega} \cdot \nabla \mathbf{u} + \nu \nabla^2 \boldsymbol{\omega}, \quad (2.6)$$

where $\boldsymbol{\omega} = \nabla \times \mathbf{u}$. Equation (2.6) multiplied by $\boldsymbol{\omega}$, after some arrangement, gives the enstrophy equation:

$$\frac{d}{dt} \left(\frac{\boldsymbol{\omega}^2}{2} \right) = \boldsymbol{\omega} \cdot (\boldsymbol{\omega} \cdot \mathbf{D}) + \nu \nabla^2 \left(\frac{\boldsymbol{\omega}^2}{2} \right) - \nu (\nabla \boldsymbol{\omega})^2, \quad (2.7)$$

where \mathbf{D} is the strain-rate tensor which is defined as:

$$D_{ij} = \frac{1}{2} \left(\frac{\partial u_i}{\partial x_j} + \frac{\partial u_j}{\partial x_i} \right). \quad (2.8)$$

Equation (2.7) in 2D turbulence reduces to:

$$\frac{d}{dt} \left(\frac{\boldsymbol{\omega}^2}{2} \right) = \nu \nabla^2 \left(\frac{\boldsymbol{\omega}^2}{2} \right) - \nu (\nabla \boldsymbol{\omega})^2. \quad (2.9)$$

Namely, in the case of 2D turbulence the stretching term of the equation (2.7) is equal to zero because the velocity gradient is always perpendicular to the vorticity, which is necessarily perpendicular to the plane of motion. In fact, it is easy to demonstrate that the stretching term vanishes as $\boldsymbol{\omega} = (0, 0, \omega)$ and the components $D_{13}, D_{31}, D_{23}, D_{32}, D_{33}$ of the strain-rate tensor D_{ij} are identically zero, hence:

$$\boldsymbol{\omega} \cdot \mathbf{D} = 0. \quad (2.10)$$

2.1.2 Quadratic invariants

In the inviscid (i.e. $\nu = 0$), unforced case (i.e. $\mathbf{f} = 0$), equation 2.5 reads:

$$\frac{d}{dt} \frac{1}{2} \langle \mathbf{u}^2 \rangle = 0. \quad (2.11)$$

Therefore, in 2D turbulence equation (2.5) the mean kinetic energy $E(t) = \frac{1}{2} \langle \mathbf{u}^2 \rangle$ is a quadratic invariant, where $\langle \dots \rangle$ represents an ensemble average, i.e. a statistical average performed on an infinite number of realizations.

Moreover, from equation (2.9), using also in this case the hypothesis of inviscid fluid, we obtain:

$$\frac{d}{dt} \left(\frac{\omega^2}{2} \right) = 0 \Rightarrow \frac{d}{dt} \left\langle \frac{\omega^2}{2} \right\rangle = 0 \Rightarrow \frac{d}{dt} Z(t) = 0, \quad (2.12)$$

from which we can conclude that in 2D turbulence the enstrophy $Z(t)$ is conserved. This result forms the basis for all the theories of two dimensional turbulence, which is then characterized by another quadratic invariant along with the mean kinetic energy, i.e. the enstrophy.

2.1.3 Velocity spectra: the enstrophy cascade and the inverse energy cascade

As previously described the conservation of the vorticity of each fluid parcel in 2D turbulence implies the existence of two quadratic invariants: the energy and the enstrophy. Therefore, Kraichnan [1967] proposed the existence of two different inertial ranges for 2D turbulence: one with constant energy flux extending from injection scale toward larger scales and one with constant enstrophy flux extending from injection scale toward the viscous scale. This is the double cascade process proposed by Kraichnan [1967]: the inverse energy cascade and the enstrophy cascade, respectively.

The understanding of the direction of the double cascade in the inertial ranges is based on the Fjortoft's theorem, which serves as the basis for 2D turbulence phenomenology. The Fjortoft's theorem, starting from the study of the 2D Euler equations in the Fourier space and the conservation laws of

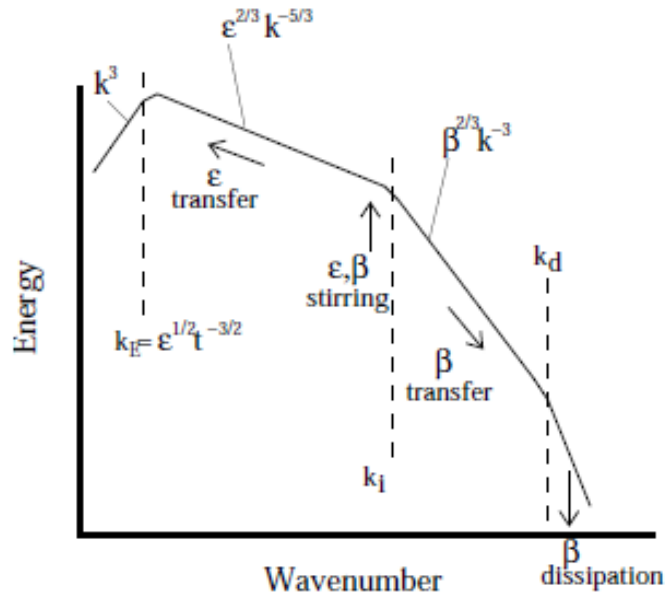


FIGURE 2.1: The energy spectrum in 2D turbulence. β indicates the injected flux, k_d is wavenumber and the wavenumber k_E is characteristic of the spectrum maximum.

kinetic energy and enstrophy, shows that the energy flows towards large scale while enstrophy flows towards small scales. A detailed reasoning is treated in Lesieur [1990] and Kraichnan [1967].

For the inverse energy cascade Kraichnan [1967] predicted the existence of a self-similar range of scales in which the energy spectrum $E(k)$ scales as $k^{-5/3}$, where k is the wavenumber. Its form, given in the Fourier space, reads:

$$E(k) = C' \varepsilon^{2/3} k^{-5/3}, \quad (2.13)$$

where C' is the Kolmogorov-Kraichnan constant, found experimentally of order 1.5, and ε is the energy flux. The dimensional analysis reported in Kraichnan [1967] is similar to the one used for 3D Kolmogorov kinetic energy cascade, except for the sign of the kinetic energy flux which is negative in 2D turbulence. In the range ($k < k_i$), in which k_i represents the forcing wavenumber, the kinetic energy spectrum is then proportional to $\varepsilon^{2/3} k^{-5/3}$ as shown in figure 2.1.

Physically, the mechanism involved in the inverse energy cascade is essen-

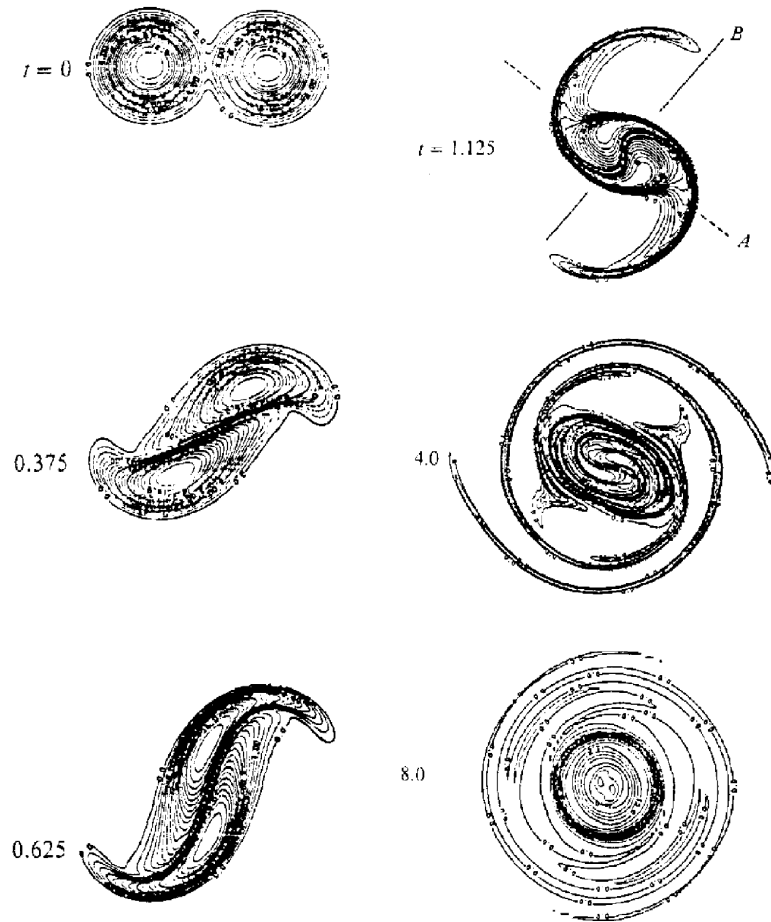


FIGURE 2.2: Steps of the vortex merging process shown by Melander et al. [1988].

tially an aggregation process, driving the formation of large clusters of like sign vortices, known as “vortex merging” [Tabeling, 2002]. The phenomenon of vortex merging plays a fundamental role in the free-decay of 2D turbulence as it involves an interplay between small and large eddies. Vortex merging has been studied along different approach: e.g. Melander et al. [1988] proposed an instability mechanism, showing as whenever two like-sign vortices are separated by less than a crucial distance, they merge.

As suggested by Fjortoft’s theorem, Kraichnan [1967] and Leith [1968] proposed the existence of the enstrophy cascade in the context of a turbulence

forced at a fixed wavenumber k_i by a stationary forcing injecting kinetic energy at a rate ε and enstrophy at a rate $\beta = k_i^2 \varepsilon$. Then a dimensional analysis similar to the one used for the Kolmogorov energy cascade in 3D turbulence assumes that:

$$E(k) \sim \beta^{\frac{2}{3}} k^{-3}, \quad (2.14)$$

where β is the enstrophy transfer rate. Batchelor [1969] proposed the same k^{-3} enstrophy cascade towards small scales for a freely-decay turbulence.

Physically, the process prevailing in the enstrophy cascade is essentially the elongation of the vorticity patches, which leads the fluid blob laying in a straining fields to a decrease of its transverse direction. Since the vorticity of each fluid parcel is conserved, the result is an increase of the gradient of the vorticity in the direction orthogonal to the straining field and an increase of the small scale vorticity. Therefore, the mechanism involved in the direct enstrophy cascade leads to a loss of energy of the small-scale flow at the advantage of the straining field [Kraichnan, 1976].

2.2 Absolute and relative dispersion

Mixing processes in straight compound channels can be analysed from a Lagrangian point of view, i.e. studying material particle (passive tracers) trajectories during the flow motion [Boffetta et al., 2001, Provenzale, 1999]. Lagrangian statistics involve averages of particle positions, in terms of single or pairs or groups of particles (absolute and relative statistics respectively). In the following a brief description of these statistics will be provided.

Particle trajectories form the basis for the Lagrangian analysis of the mixing process and for the computation of absolute dispersion and diffusivity. Given an Eulerian velocity field it is possible to compute trajectories of material particles by integrating the equation:

$$\frac{d\mathbf{x}^*(t^*)}{dt^*} = \mathbf{u}^*(\mathbf{x}^*, t^*), \quad (2.15)$$

where $\mathbf{x}^*(t^*)$ is the position at time t^* of the given particle and $\mathbf{u}^*(\mathbf{x}^*, t^*)$ is the Eulerian velocity at point \mathbf{x}^* and time t^* . Hereinafter stars denote

dimensional quantities.

The mean Lagrangian kinetic energy is computed to test if particle trajectories reach quasi-stationary conditions and it is defined as

$$E_L^*(t^*) = \left(\frac{1}{2}\right) \left\langle u_L'^*(x^*, y^*, t^*)^2 + v_L'^*(x^*, y^*, t^*)^2 \right\rangle, \quad (2.16)$$

where $u_L'^*$ and $v_L'^*$ are the Lagrangian velocity fluctuations and the brackets indicate average over the total number of particles. The Lagrangian kinetic energy should be constant over the entire duration of the experiments and it should be $E_L^* \sim E_E^*$, which is its Eulerian counterpart, to confirm that the computed particle trajectories provide a good sampling.

2.2.1 Single-particle statistics

Once the particle trajectories are known, the absolute dispersion tensor, $\mathbf{A}^{*(2)}$, can be found [see Provenzale, 1999, among others]:

$$A_{ij}^{*(2)}(t^*, t_0^*) = \frac{1}{M} \sum_{m=1}^M \{ [x_i^{*m}(t^*) - x_i^{*m}(t_0^*)][x_j^{*m}(t^*) - x_j^{*m}(t_0^*)] \}, \quad (2.17)$$

where M is the total number of particles, $\mathbf{x}^{*m}(t^*)$ is the position of the m -th particle at time t^* and $\mathbf{x}^{*m}(t_0^*)$ is its initial position (at time t_0^*). If the flow is isotropic $\mathbf{A}^{*(2)}$ is a multiple of the identity matrix. The mean square displacement is given by the trace of $\mathbf{A}^{*(2)}$, defined as total absolute dispersion, which reads:

$$a^{*2} = \text{Trace} \left(\overline{\mathbf{A}^{*(2)}} \right) = A_{xx}^{*(2)} + A_{yy}^{*(2)}. \quad (2.18)$$

However, in the most general non-isotropic case, the average square displacements along the x^* , y^* directions may be different owing to flow anisotropy. The time derivatives of absolute dispersion is defined as absolute diffusivity $K^{*(1)}$

$$K^{*(1)} = \frac{1}{2} \frac{d}{dt^*} \left[\text{Tr}(\mathbf{A}^{*(2)}) \right], \quad (2.19)$$

which can be written as

$$K^{*(1)} = K_x^{*(1)} + K_y^{*(1)}. \quad (2.20)$$

The absolute diffusivity coefficient measures the average rate of spreading of the particles in the domain.

The time dependence of the diffusivity coefficients enables clear identification of different dispersion regimes [Boffetta et al., 2001, Provenzale, 1999]: in a wide variety of applications, the absolute dispersion obeys power laws of the type $a^{*2}(t^*, t_0^*) \sim t^{*\gamma}$ and, therefore, the absolute diffusivity can be described as $K^{*(1)} \sim t^{*\gamma-1}$. The fundamental results obtained by Taylor [1921] in the case of homogeneous turbulence show that, for short times after particles' deployment, an exponent $\gamma = 2$ can be expected, describing the so-called “ballistic regime”. For times longer than an integral time scale T_L^* , defined as the decorrelation time, the exponent should be $\gamma = 1$, the so-called diffusive or Brownian regime. The Lagrangian time scale T_L^* is evaluated as the integral of the normalized velocity autocorrelation $\mathcal{R}(\tau)$:

$$T_L^* = \int_0^\infty \mathcal{R}(\tau^*) d\tau^*, \quad (2.21)$$

where the Lagrangian normalized autocorrelation of the i -th velocity component is computed using the following estimator:

$$\mathcal{R}_{ii}(\tau^*) = \frac{\frac{1}{M} \sum_M \rho_{Lii}^*(\tau^*)}{[\text{Var}(u_{Li}^{*'}) \text{Var}(u_{Li}^{*'})]^{1/2}}, \quad (2.22)$$

where $\rho_{Lii}^*(\tau^*)$ is the covariance of the velocity component along the i -th direction defined as:

$$\rho_{Lii}^*(\tau^*) = \left\langle u_{Li}^{*'}(t^*) u_{Li}^{*'}(t^* + \tau^*) \right\rangle. \quad (2.23)$$

Here the brackets indicate an average over the time, whereas the covariance is averaged over a set of N trajectories.

The Lagrangian decorrelation time T_L^* can be interpreted as the “time necessary for each particle to loose memory of its initial velocity”.

Relations of time dependence of the diffusivity coefficient can be schematically summarized as follows:

$$a^{*2} \propto t^{*2} \text{ for } t^* \ll T_L^*, \quad (2.24)$$

$$a^{*2} \propto t^* \text{ for } t^* \gg T_L^*. \quad (2.25)$$

For intermediate times, a variety of scalings has been found, depending on the specific flow under investigation.

The Taylor asymptotic regimes have been extended by Babiano et al. [1987], who showed that the exponent of the time power laws of the absolute dispersion depends on the slope of the Lagrangian energy spectrum in the frequency domain ($L^*(\sigma^*)$). Besides, they have proved that the Brownian regime is independent of the restrictive hypothesis of flow homogeneity. This result is supported by Lagrangian data derived from inhomogeneous oceanic and atmospheric velocity fields, see Elhmaïdi et al. [1993] and references cited therein. It is easy to show that the absolute diffusivity $K^{*(1)}$ can be expressed in terms of the normalized velocity autocorrelation $\mathcal{R}(\tau^*)$ [see LaCasce, 2008, among others]:

$$K^{*(1)} = \nu^{*2} \int_0^\infty \mathcal{R}(\tau^*) d\tau^* = \nu^{*2} T_L^*. \quad (2.26)$$

The diffusivity is, thus, the product of the velocity variance (ν^{*2}) and of the Lagrangian time scale. If we now write the Lagrangian frequency spectrum $L^*(\sigma^*)$ by using the Fourier transform of the velocity autocorrelation as:

$$L^*(\sigma^*) = 2\nu^{*2} \int_0^\infty \mathcal{R}(\tau^*) \cos(2\pi\sigma^*\tau^*) d\tau^* \quad (2.27)$$

we find that for $\sigma^* = 0$ the spectrum is proportional to the absolute diffusivity:

$$L^*(0) = 2\nu^{*2} \int_0^\infty \mathcal{R}(\tau^*) d\tau^* = 2\nu^{*2} T_L^* = 2K^{*(1)}. \quad (2.28)$$

The latter result implies that the absolute diffusivity is determined by the lowest-frequency motion, e.g. by the mean flow [Davis, 1982]. Indeed, a constant mean causes the absolute dispersion to increase quadratically in time, and, thus, the diffusivity to increase linearly in time.

2.2.2 Multiple-particle statistics

The relative dispersion can be defined as the mean square distance at time t^* between a pair of particles that at time t_0^* have a distance equal to d_0^* , and is formulated as:

$$R_{ij}^{*(2)}(t^*, t_0^*, d_0^*) = \frac{1}{M-1} \sum_{m=1}^{M-1} \left\{ [x_i^{*m}(t^*) - x_i^{*(m+1)}(t^*)][x_j^{*m}(t^*) - x_j^{*(m+1)}(t^*)] \right\}, \quad (2.29)$$

where $(M-1)$ is the number of particle pairs. In analogy with the absolute statistics a total relative dispersion, mean square relative displacement between pairs, can be defined as the trace of the matrix given by equation (2.29):

$$r^{*2} = \text{Trace}(\mathbf{R}^{*(2)}). \quad (2.30)$$

The time derivative of relative dispersion, defined as the relative diffusivity $K^{*(2)}$ can be written as:

$$K^{*(2)} = \frac{1}{2} \frac{d}{dt^*} \left[\text{Tr}(\mathbf{R}^{*(2)}) \right]. \quad (2.31)$$

Classical studies on 2D turbulence [Babiano et al., 1990, Bennett, 1984, Kraichnan, 1966, Lin, 1972] demonstrate that the two distinct cascading regimes (inverse energy cascade and direct enstrophy cascade) can be characterized in terms of relative diffusivity: $K^{(2)} \propto r^{4/3}$ in the energy cascade and $K^{(2)} \propto r^2$ in the enstrophy cascade. The former relationship (“Richardson-Obukhov law”) descends from a cubic growth with time of the mean-squared relative displacement r^2 , while the latter Kraichnan-Lin law corresponds to an exponential growth in time of r^2 . Relations of time dependence of relative coefficients in analogy with the absolute diffusivity can be schematically summarized as follows [Bennett, 1987]:

$$r^{*2} \propto t^{*2} \text{ and } K^{*(2)} \propto t^* \text{ for } t^* < T_P^*; \quad (2.32)$$

$$r^{*2} \propto t^{*3} \text{ and } K^{*(2)} \propto r^{*\frac{4}{3}} \text{ for } T_P^* < t^* < T_L^* \quad (2.33)$$

$$K^{*(2)} \approx 2K^{*(1)} \text{ for } t^* > T_L^* \quad (2.34)$$

where T_P^* represents the time for which “pairs of particles have lost memory of their initial separation d_0^* ”. The relationship between the absolute and relative diffusivity for large times, i.e. $t^* > T_L^*$, is easily demonstrated from equation (2.19) and (2.31).

Bennett [1984] showed that the dependence of the diffusivity on separation directly reflects the slope of the energy spectrum in the wavenumber space $E(k) \propto k^{-\alpha}$, linking the inverse energy cascade ($\alpha = 5/3$) to a growth of relative diffusivity proportional to $r^{4/3}$ and the enstrophy cascade ($\alpha = 3$) to a growth proportional to r^2 . As pointed out by Er-El and Peskin [1981] the two-particle diffusion in 2D turbulence can be controlled by two distinct dynamical mechanisms leading to two different regimes known as “local dispersion” and “non-local dispersion”. In local dynamics the relative dispersion is controlled by a local straining mechanism which is not really effective in causing further separation of the particles, while in the case of non-local dynamics particles are subjected to very strong shear produced by the large-scale structures. The two dispersion regimes can be identified on the basis of the value of the energy spectrum slope α [Bennett, 1984]. The local dynamics are characterized by $1 < \alpha < 3$ and the dispersion of pairs is dominated by eddies of the same scale of their separation. Hence, the corresponding diffusivity scales as

$$K^{(2)} \equiv \frac{1}{2} \frac{d}{dt} r^2 \propto r^{\frac{(\alpha+1)}{2}}. \quad (2.35)$$

Non-local dynamics, otherwise, are characterized by values of α larger than 3 (steeper spectra). Valuable additional information on the dispersion regimes can be extracted from the analysis of the PDFs of the separations of pairs of particles. The PDF, a normalized histogram of displacements, is crucial for the estimate of the flow and mixing regimes because all moments are derived from it: the spread about the center of mass can be measured by the variance of the displacements, i.e. using the second-order moment [LaCasce, 2008]. Usually, the dispersion measures the width of the PDF but it does not give any information on the shape of the distribution. To get a more detailed description from the PDFs it is necessary to evaluate higher-order moments, in particular the fourth-order moment, the kurtosis ku , provides important insight on the shape of the distribution. Particles undergoing a random walk

lead to a Gaussian PDF, characterized by a kurtosis ku of 3. More often, a coherent advection produces PDFs which are not Gaussian and characterized by larger values of the kurtosis. As suggested by Er-El and Peskin [1981], Bennett [1984] and LaCasce [2008], under local dispersion the separation kurtosis is constant in time, while for non-local dynamics it grows exponentially. Finally, a potential difficulty with the use of the relative dispersion as a suitable measure concerns the methods of averaging distances at fixed times. If the dispersion is dominated by flow structures with size comparable with the particles' separation, averaging pairs with different separations may blur the dependencies. The Finite Scale Lyapunov Exponents (FSLE), consisting in averages of times at fixed distances, provide an useful alternate approach. In comparison with the relative diffusivity, the FSLE has the additional advantage of being an integral quantity rather than a derivative, and generally, it tends to be smoother than the diffusivity and less sensitive to random errors, which always affect experimental measurements. To calculate the FSLE it is necessary to first choose a set of distances that increase recursively:

$$r_n^* = \alpha r_{n-1}^* = \alpha^n r_0^*, \quad (2.36)$$

where α is an arbitrary constant larger than unity and then calculate the times required (known as “exit time” T_n^*) for each pair displacement to grow to the successive r_n^* . The estimate for the maximum Lyapunov exponent varies with distance and reads

$$\lambda_s^*(n) = \frac{1}{\log(\alpha)} \left\langle \frac{1}{T_n^*} \right\rangle. \quad (2.37)$$

If the dispersion has a power law dependence with time, like for local dispersion, the FSLEs exhibit a power law dependence on the separation. In particular, being the dispersion proportional to a power of time as ($r^2 \propto t^\gamma$), then the FSLEs, being mean inverse times, scale like $\lambda_s \propto r^{-2/\gamma}$. Generally, results obtained by means of the FSLE should recall those obtained by means of the relative diffusivity.

2.3 Conclusions

In the present study the basic concepts and tools briefly described above will be used to analyze mixing processes from a Lagrangian point of view. In particular, starting from the Eulerian velocity fields obtained by means of the PIV technique, we will perform a numerical integration of sets of particles trajectories, which form the basis for the Lagrangian analysis of the mixing processes. Hence, we will proceed in analyzing averages of particles positions, in terms of single and pairs of particles, in order to compute absolute and relative dispersion. Starting from the Lagrangian autocorrelation of velocity components (see equation (2.22)) we will evaluate the Lagrangian Integral scales, which are used together with the Lagrangian Kinetic energy to make dimensionless the resulting dispersion and diffusivity coefficients and to identify different dispersion regimes. The analysis of the behaviour of relative diffusivity (equation (2.31)) and the computation of the Eulerian Power Spectra Density function enable identification of different energy transfer processes. Valuable additional information on the dispersion regimes will be extracted from the analysis of the PDFs of the separation of pairs of particles and by analysing the decay of the finite-scale Lyapunov exponents with the particle separations.

Chapter 3

The experiments

3.1 Experimental set-up

Physical experiments have been carried out at the laboratory Enrico Marchi of the Department of Civil, Chemical and Environmental Engineering (DICCA), of the University of Genova, Italy using a flume which is 20 m long, 0.6 m wide with a trapezoidal cross-section, showed in figure 3.1. The general view of the experimental set-up is shown in figure 3.2. The cross-section

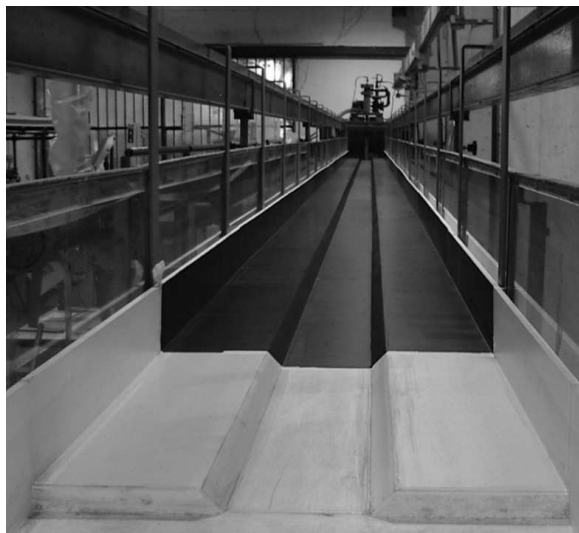


FIGURE 3.1: Cross-section of the compound channel.



FIGURE 3.2: General view of the DICCA compound channel flume.

is composed by a central main channel ($W_{mc}^* = 20$ cm), two lateral flat floodplains ($W_{fp}^* = 18$ cm) and a transition region ($W_{tr}^* = 2.5$ cm). A sketch of the cross-section of the experimental flume is shown in figure 3.3. Stars identify dimensional quantities. The compound channel, including the lateral

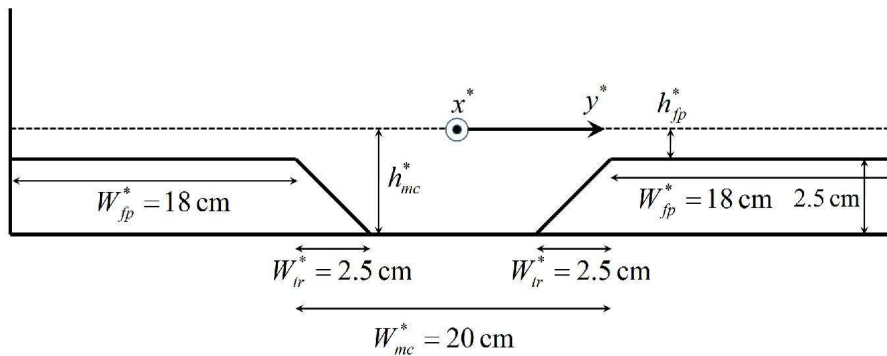


FIGURE 3.3: Sketch of the cross section of the flume.

vertical walls, is made by sheets of polyvinyl chloride (PVC) 1cm thick with a Manning roughness n equal to $0.009 \text{ s}^{-1}\text{m}^{1/3}$. The apparatus allows changes in the bed longitudinal slope (S). The change of the bed longitudinal slope was performed through the use of the cathetometer, (see figure 3.4). This instrument is used to measure the difference in level between two sections

through the reading of a graduated rod fixed to the axis of the telescope with an accuracy of one millimetre.



FIGURE 3.4: Cathetometer used to measure bed longitudinal slope and channel inlet.

The hydraulic circuit which has fueled the channel during the experiments consists of an inlet section and two collecting tanks at the outlet, recirculation piping, two pumps and an electronic/manual water discharge control system. Between the inlet and the beginning of the measuring channel a system of flow straighteners has been provided (which are a series of metal sheets positioned at 2 cm apart each other, figure 3.4), and grids containing glass wool in order to dissipate the turbulence of the inlet and obtain the most possible uniform flow in the measuring section.

Cartesian coordinate system is used in which the x^* and y^* axes are aligned with the streamwise and spanwise direction of the flow, respectively, as is illustrated in figure 3.3. About seventy experiments have been performed by changing the main dimensionless experimental parameters r_h and Fr , defined as

$$r_h = \frac{h_{mc}^*}{h_{fp}^*} \qquad Fr = \frac{U_m^*}{\sqrt{gR^*}} \qquad (3.1)$$

where h_{mc}^* is the main channel depth and h_{fp}^* is the floodplain depth, g is the gravity acceleration, U_m^* is the surface peak velocity in the main channel and R^* is the hydraulic radius. The main characteristics of the experiments are

grouped in table 3.1 providing the values of r_h , the Froude number, the liquid discharge (Q^*) and the Reynolds number $Re = 4U_m^*R^*/\nu$, where ν is the kinematic viscosity. The measuring area is at a distance of 10 m downstream of the flume inlet and it is characterized by fully-established flow conditions both in terms of bottom boundary layer and transition shear layer evolution [Stocchino et al., 2011, Stocchino and Brocchini, 2010]. According to Bousmar et al. [2005] compound channel flows are fully established for a length L downstream of the inception with $L/W_{fp} > 35$; in the present case it is $L > 6.6\text{m}$.

Results are analysed with reference to the classification introduced by Nezu et al. [1999]. “Shallow flows” ($r_h > 3$) are characterized by monotonic velocity profiles and a strong velocity gradients at the transition between the main channel and the floodplains, leading to a strong shearing in the transition, associated with intense macro-vortices. At the wall boundary layers only a weak shear occurs and almost no macro-vortices are generated.

“Intermediate flows” ($2 < r_h < 3$) are characterized by non-monotonic velocity profiles with a dip over the transition. According to Nezu et al. [1999] such an effect is the signature of counter-rotating macro-vortices at the transition. The depth increase leads to a growth of the wall boundary layer thickness and macro-vortices are generated, by wall-adherence-induced shearing, also over the floodplain close to the walls.

“Deep flows” ($r_h < 2$) are characterized by a very weak shear in the transition region. The wall boundary layer increases in size and more and stronger macro-vortices are generated over the floodplains, while the influence of the topography is much weaker.

For high values of the Froude number, surface waves may be generated that can possibly interfere with the surface velocity measurements, object of the present study. In particular, roll waves are known to form for Froude numbers larger than 2. In order to avoid the generation of surface waves, we have placed at the the flume inlet a polystyrene sheet, free to float on the water surface, that significantly damps water surface oscillations of any kind.

TABLE 3.1: Main experimental parameters

Flow	Exp. Series	r_h (-)	Fr (-)	S (-)	Q^* (l/s)	U_m^* (m/s)	$Re \cdot 10^3$ (-)
Shallow	Series 00	3.05-3.69	0.63-0.73	0.0016	2.39-3.49	0.25-0.31	16.0-13.1
	Series 00	3.40-4.42	1.12-1.26	0.0048	3.55-5.25	0.42-0.52	23.9-34.9
	Series 0	3.10	1.31	0.0064	4.88-6.14	0.51-0.56	32.6-40.6
	Series 200	3.08-4.16	0.89-0.93	0.0032	2.99-4.37	0.34-0.39	20.1-28.9
	Series 400	3.15	1.64	0.0100	7.47-7.92	0.69-0.70	49.5-52.3
	Series 500	3.10-3.94	1.89-1.94	0.0140	6.68-9.07	0.73-0.82	40.5-60.0
	Series 800	3.50-4.08	1.52-1.59	0.0100	5.42-6.14	0.61-0.62	36.3-40.9
	Series 900	3.01	1.14	0.0048	5.55	0.49	36.7
Intermediate	Series 00	2.20-2.61	0.72-0.73	0.0016	4.32-5.89	0.33-0.37	28.3-37.9
	Series 00	2.36	0.92	0.0048	6.54-10.75	0.45-0.63	42.4-68.7
	Series 0	2.02-2.92	1.32-1.42	0.0064	6.68-13.54	0.57-0.75	44.0-86.1
	Series 200	2.04-2.57	0.96-1.00	0.0032	5.85-9.44	0.44-0.53	38.2-60.1
	Series 800	2.20-2.89	1.66-1.72	0.0100	8.51-13.94	0.72-0.87	56.1-89.6
	Series 900	2.23-2.65	1.17-1.20	0.0480	6.79-9.44	0.53-0.60	44.4-60.8
Deep	Series 00	1.77-1.97	0.73-0.75	0.0016	7.47-9.87	0.40-0.44	47.3-61.2
	Series 00	1.82-1.85	1.21-1.36	0.0048	14.29-16.66	0.69-0.78	89.4-103.9
	Series 0	1.85-1.96	1.43-1.45	0.0064	14.67-16.99	0.77-0.83	92.8-111.8
	Series 200	1.68-1.89	1.01-1.05	0.0032	11.31-16.07	0.56-0.64	71.1-98.2
	Series 500	1.77-1.99	2.10-2.16	0.0140	20.73-28.51	1.13-1.26	131.5-176.6
	Series 800	1.77-1.91	1.79-1.82	0.0100	19.53-24.12	0.99-1.07	122.9-149.4

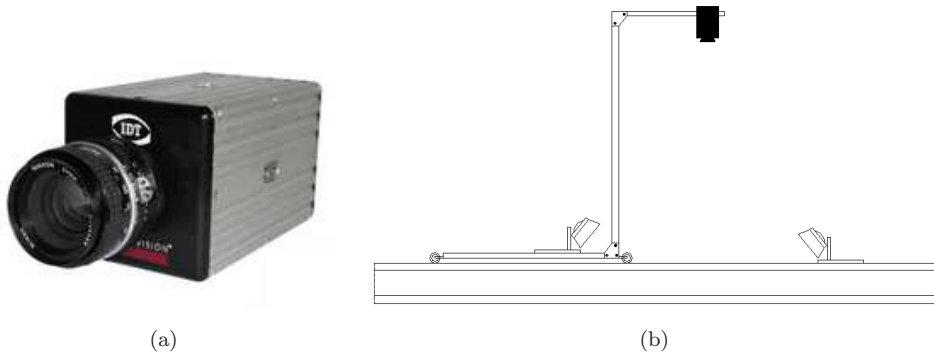


FIGURE 3.5: (a) High-speed digital camera and (b) sketch of digital camera and lighting system.

3.1.1 PIV system

The PIV system consists of a high-speed digital camera (IDT model Xs3) shown in figure 3.5b, and an illumination system composed by four white light incandescent lamps of 500 Watts (figure 3.5b).

The seeding tracers are white plastic particles with a mean diameter of $150 \mu\text{m}$ and a specific gravity of about 1.05. Anti-clustering treatments have been preventively applied to the particles. The approximate area density of the particle tracers was estimated in about $10 \text{ particles/cm}^2$. Therefore, the area of interest was a rectangle with dimensions up to $(1.2 \times 0.6) \text{m}^2$. The image-repetition rate was chosen between 100 Hz and 250 Hz, depending on the flow velocity and a single acquisition was made of a number of frames between 2000 and 4000, resulting in different temporal intervals from 10 to 45 seconds. A simple example of recorded image is shown in 3.6.

To test the repeatability of the measurements, we have performed several acquisitions for a fixed set of experimental parameters (r_h, Fr). Finally, Probability Density Functions (PDFs) of the measured displacements have been calculated to test whether the PIV set up in use was adequate to avoid peak-locking effects, which may deteriorate the quality of the measurements. The resulting PDFs, not being multimodal, suggest that the measured velocity are not affected by such a systematic error.

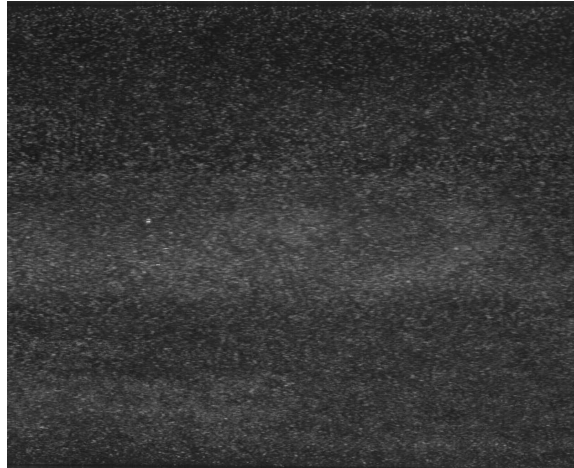


FIGURE 3.6: Example of recorded image.

3.2 Experimental approach: the Particle Image Velocimetry system

Measurements of two-dimensional velocity fields on the free surface have been obtained by means of a 2D PIV analysis. Particle Image Velocimetry (PIV) is an optical method of flow visualization and it is used to obtain instantaneous velocity measurements and related properties in fluids. The fluid is seeded with tracer particles which are illuminated in a plane of the flow. The displacement of the particles images is used to calculate two-dimensional velocity fields. The PIV technique has been used to analyse the main features of the flow under investigation and the Eulerian velocity fields are used as the basis for the computation of the tracers' trajectories and the subsequent analysis of mixing processes. The present experimental approach, based on the free-surface velocity measurement, is often used in many experimental works with primary focus on quasi-2D vortical structures [see Jirka, 2001, Nikora et al., 2007, Socolofksy and Jirka, 2004, among others]. This approach is valid as long as secondary flows, which develop over vertical cross-sections of the flow, can be considered negligible in the formation of the quasi-2D macro-vortices at hand. In the following we briefly describe the basic features of the PIV measurement technique. Most of the material presented in this section is treated in great detail in the book of Raffel et al. [1998].

Since for the analysis of the images we use the commercial software IDTproVisionTM PIV software, the description provided in this section has to be intended only as a brief presentation of the general features of the experimental apparatus and of the mathematical concepts that are used in a generic PIV analysis.

3.2.1 Fundamental principles of PIV

A typical PIV system consists of several components, as shown in figure 3.7. The flow is seeded with tracers particles and it is investigated by a plane of light produced by the passage of a laser beam through a system of lenses and mirrors. It is assumed that the tracer particles move with local flow velocity. One or more digital cameras record pictures of the light reflected by the particles through a CCD sensor (Charge Coupled Device).

PIV records images of the particles at different instants of time and analyses them on the basis of a statistical method to evaluate the particles average displacement in small areas named interrogation windows. The result is a map of local displacement vectors from which, known the time interval between two shots, the velocity fields are derived.

In order that a measurement session is successful, the operator must adjust optimally the parameters under its control:

- *Image-repetition rate*: must be sufficiently long to enable the estimation of the displacement of the particles between two images with adequate resolution. Meanwhile, the value must be such that the particles with an out-of-plane velocity do not have time to leave the analysed domain.
- *Density of tracer particles*: a key parameter to obtain suitable images is the amount of particles to use. Three different types of particle image density can be distinguished (see figure 3.8). Low density of tracer particles allow one to detect the trajectory of each particle through the measurement methods of tracking, denominated Particle Tracking Velocimetry (PTV). A medium density of tracer particles is required in the standard techniques of statistical evaluation PIV. As in the previous case the particles are clearly visible but the displacement is calculated

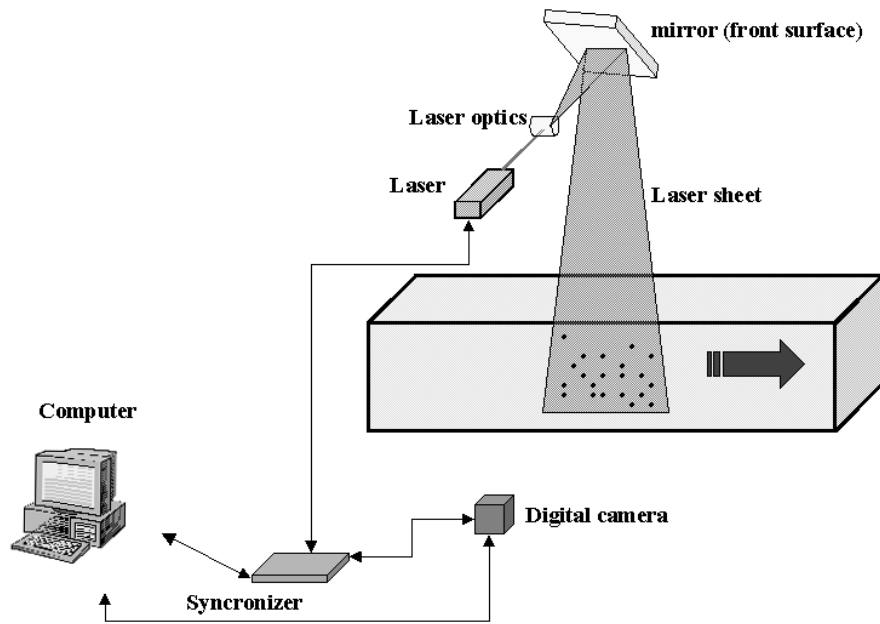


FIGURE 3.7: Pictorial sketch of a generic PIV system.

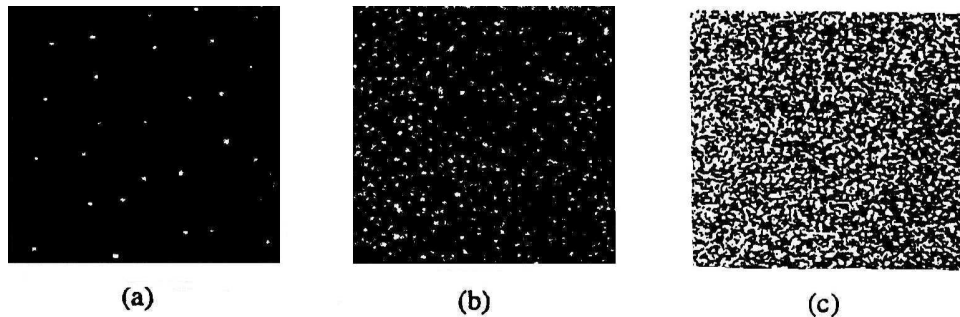


FIGURE 3.8: Modes of particles image density:(a)Low density, (b)Mean density, (c)High density, from Raffel et al. [1998].

on a statistical basis whereas a group of points. If particle density is too high, it is not possible to identify single particles as they overlap and appear as speckles. It is the case of Laser Speckle Velocimetry (LSV).

- *Laser illumination:* it is necessary to find a good balance between the particle size and the power of the light source: in fact, the use of larger particles which allow to obtain a greater amplification of the reflected light, is opposed to the need to have a tracer that follows the current

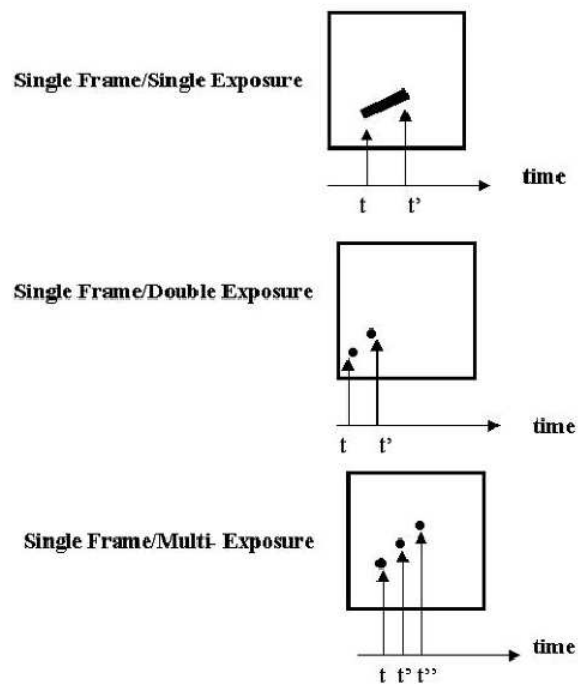


FIGURE 3.9: Single frame recording technique, from Raffel et al. [1998].

without disturbing the flow. In liquid flow particles of large diameter are used for which in general can use less powerful sources.

- *Laser pulse duration*: the duration of the light pulse emitted by the laser during the shot of the picture must be very quick so that the particles prove "frozen" and do not show streaks.
- *Size of interrogation window*: the size of the interrogation area must be small enough so that the velocity gradients inside are negligible.

3.2.2 Image recording techniques

The different approach to PIV image recording can be separated into : (a) single-frame/multiple exposure PIV and multi-frame/single exposure PIV. A schematic description of the two techniques is shown in figure 3.9 and figure 3.10. The first approach consists in capturing the illuminated flow on a single frame, so that there is no information on the temporal order of the

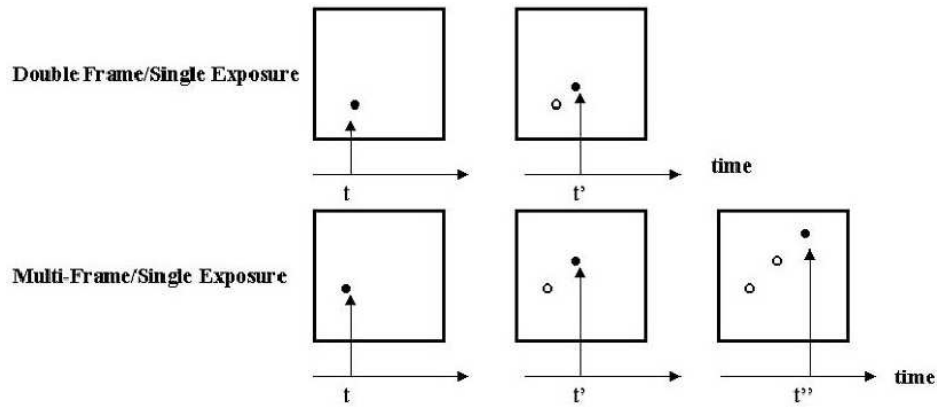


FIGURE 3.10: Multi frame recording technique, from Raffel et al. [1998].

illumination pulses. This may give rise to some ambiguity in identifying the direction of displacement vectors.

The second approach (multi-frame/single exposure) involves the acquisition of multiple frames, each corresponding to a laser pulse, so that the temporal order of the particle position is preserved.

Depending on the techniques chosen for subsequent analysis an appropriate image recording approach can be selected. In the present experimental campaign, we chose to use the second method since for further analysis was necessary to preserve the temporal order of the images.

3.2.3 Post-processing of PIV data

For the analysis of the images of our experiments we used the commercial software IDTproVisionTM PIV software. Hereinafter mathematical concepts that are used in a generic PIV analysis are briefly described.

A recording session consists of a random distribution of particle images, with

describe the pattern of N tracer particles inside the flow. The random distribution of particles at a given time t may be represented by:

$$\Gamma = \begin{pmatrix} \mathbf{X}_1 \\ \mathbf{X}_2 \\ \cdot \\ \cdot \\ \cdot \\ \mathbf{X}_N \end{pmatrix}, \quad (3.2)$$

where \mathbf{X}_i represent the position vector of a particle at time t . The image position vectors, which represent the coordinates of the particle i at time t on the image plane may be described as :

$$\mathbf{x}_i = \begin{pmatrix} x_i \\ y_i \end{pmatrix}. \quad (3.3)$$

The particles position coordinates and image position coordinate are assumed to be related by a constant magnification factor M :

$$X_i = \frac{x_i}{M}, Y_i = \frac{y_i}{M}. \quad (3.4)$$

The PIV image can be described as a convolution of the geometric image and the impulse response of the imaging system, the so-called point spread function. Particles are assumed infinitely small and the lenses are assumed perfectly aberration-free well focused, so the point spread function can be described by the square of the first order Bessel function, also called Airy function. A good approximation for the Airy function of a real lens system is a Gaussian function $\tau(\mathbf{x})$. The most complete and careful mathematical description of physical background has been given by Raffel et al. [1998]. The convolution product of $\tau(\mathbf{x})$ with the geometric the geometric image of the particle at the position \mathbf{x}_i represents the image of a single particle located at position \mathbf{X}_i . The geometric image of infinitely small geometric particle can be described by a Dirac delta-function shifted to the position \mathbf{X}_i . The image

intensity field of the PIV image may be written as:

$$I(\mathbf{x}, \mathbf{\Gamma}) = \tau(\mathbf{x}) * \sum_{i=1}^N V_0(\mathbf{X}_i) \delta(\mathbf{x} - \mathbf{x}_i), \quad (3.5)$$

where $V_0(\mathbf{X}_i)$ is the transfer function which gives the conversion into an electronic signal of the light energy of the image of an individual particle. With:

$$\tau(\mathbf{x} - \mathbf{x}_i) = \tau(\mathbf{x}) * \delta(\mathbf{x} - \mathbf{x}_i), \quad (3.6)$$

the image intensity field can be written as :

$$I(\mathbf{x}, \mathbf{\Gamma}) = \sum_{i=1}^N V_0(\mathbf{X}_i) \tau(\mathbf{x} - \mathbf{x}_i). \quad (3.7)$$

PIV recordings are most often evaluated by means of a method based on the cross-correlation of two different frames. Two frames are acquired at two different times t and $t' = t + \Delta t$. A constant displacement \mathbf{D} of the particles inside the real space is assumed, so that the particles locations at time t' are given by:

$$\mathbf{X}'_i = \mathbf{X}_i + \mathbf{D}_i = \begin{pmatrix} X_i + D_{xi} \\ Y_i + D_{yi} \\ Z_i + D_{zi} \end{pmatrix}. \quad (3.8)$$

Considering identical light sheet during the recording of the two frames, the cross-correlation function of the intensity fields of two different frames can be written as:

$$R_{II}(\mathbf{s}, \mathbf{\Gamma}, \mathbf{D}) = \langle I(\mathbf{x}, \mathbf{\Gamma}) I'(\mathbf{x} + \mathbf{s} - \mathbf{d}, \mathbf{\Gamma}) \rangle, \quad (3.9)$$

where \mathbf{d} are the particles image displacement, \mathbf{s} is the displacement vector on the cross-correlation plane and I' is the intensity field of the second frame, defined as :

$$I'(\mathbf{x}, \mathbf{\Gamma}) = \sum_{j=1}^N V'_0(\mathbf{X}_j + \mathbf{D}) \tau(\mathbf{x} - \mathbf{x}_j - \mathbf{d}). \quad (3.10)$$

It is possible to decompose the correlation into three parts:

$$R_{II}(\mathbf{s}, \mathbf{\Gamma}, \mathbf{D}) = R_C(\mathbf{s}, \mathbf{\Gamma}, \mathbf{D}) + R_F(\mathbf{s}, \mathbf{\Gamma}, \mathbf{D}) + R_D(\mathbf{s}, \mathbf{\Gamma}, \mathbf{D}), \quad (3.11)$$

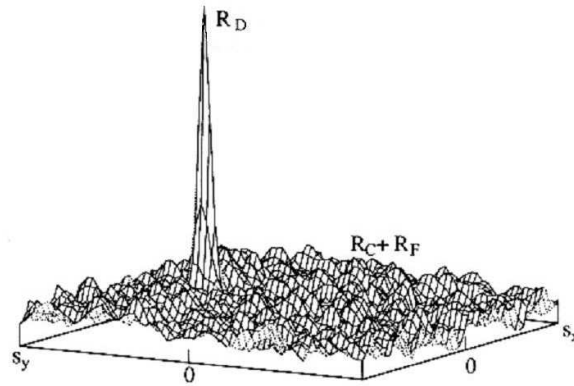


FIGURE 3.11: Cross-correlation function on the cross correlation plane, from Raffel et al. [1998].

where $R_D(\mathbf{s}, \mathbf{\Gamma}, \mathbf{D})$ represents the terms of the cross-correlation corresponding to $i = j$, i.e. terms representing the correlation of particles images of the first frame with images of the same particles belonging to the second frame; while $R_C(\mathbf{s}, \mathbf{\Gamma}, \mathbf{D}) + R_F(\mathbf{s}, \mathbf{\Gamma}, \mathbf{D})$ represents terms with $i \neq j$, i.e. referred to the correlation of randomly distributed particles. An example of a cross-correlation function on the cross correlation plane is shown in figure 3.11.

The data resulting from the analysis phase, before reaching the final presentation, follow a path characterized by the following key moments:

Validation of the raw data: after the analysis of the images, incorrect velocity vectors are often display (denominated "outliers"). Different validation methods have been proposed to highlight such data. These methods are generally based on moving average processes of knowledge of general patterns of flow field;

Replacement of incorrect data: after the previous operation, removed incorrect vectors need to be replaced since the for most post-processing algorithms it is required to have complete data fields. To do this, PIV uses for instance bilinear interpolation using vectors in the vicinity of that witch has to be replaced;

Data reduction: the PIV is a highly productive technique, from each measurement session thousands of data are obtained. For this reason the data is synthesized using average, conditional sampling and vector field operators.

Chapter 4

PIV results : experimental observation of Eulerian Flow fields

4.1 Mean Flow velocity profiles

4.1.1 2D velocity fields

Time-averaged velocity profiles obtained by the PIV measurements are shown in figure 4.1. Each figure refers to a velocity field for different values of the parameter r_h , i.e. to shallow, intermediate and deep flow conditions.

In the top panel of figure 4.1 is represented an example of velocity field obtained in case of shallow flow conditions. These conditions are characterized by a strong velocity gradient localized in the transition region between the main channel and floodplain where, consequently, macro-vortices are generated.

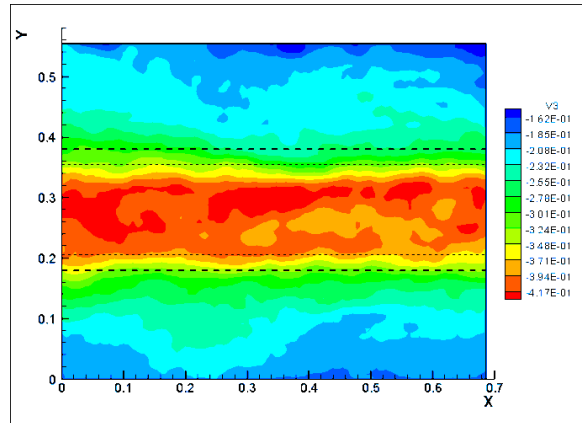
An example of velocity field in case of deep conditions are shown in panel c of figure 4.1. This measure highlights as in these conditions the streamwise velocity resembles that occurring in a rectangular channel: a weak shear occurs in the transition region and the macro-vortices are also generated in the wall boundary layer of the floodplain.

The streamwise velocity induced in intermediate flows are shown in figure 4.1 panel b, and it is characterized by a dip in the transition region, weaker than the shallow flow conditions. The non-monotonic behaviour of the velocity suggests that the topographic forcing has an important role in the generation of two-dimensional macro-vortices in straight compound channels.

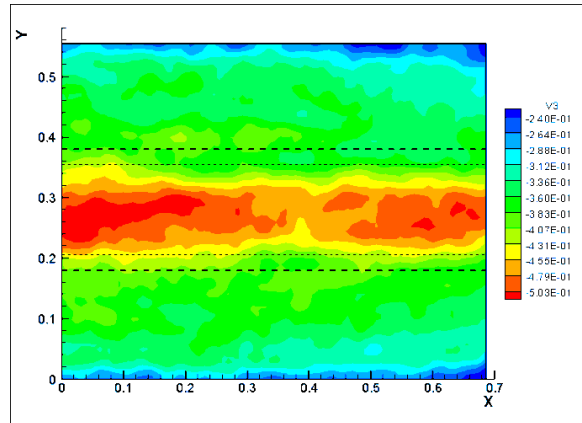
4.1.2 Mean streamwise velocity profiles

The two-dimensional velocity fields obtained by means of the PIV analysis have been elaborated to extract the main flow features of the flow under investigation. In particular, we performed an ensemble average on the velocity fields and, then, spatial averages along the streamwise direction to extract mean streamwise velocity profiles and profiles of dimensionless averaged Reynolds stress $\overline{u'v'}$ (see figure 4.2). In the following results are analysed with the reference to the classification introduced by Nezu et al. [1999].

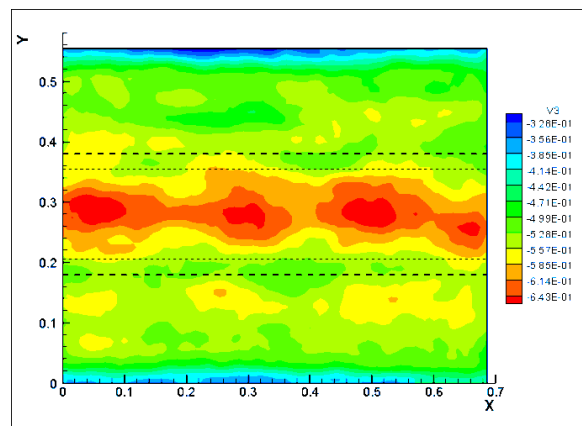
- (a) The “Shallow Flows” ($r_h > 3$) are characterized by monotonic velocity profiles and a strong velocity gradient at the transition between the main channel and the floodplain (see figure 4.2(a)). The ratio between the peak main channel velocity and the floodplain velocity is 1.3 – 1.5. This leads to a strong shearing in the transition and is associated with intense macro-vortices. At the wall boundary layers only a weak shear occurs and almost no macro-vortices are generated. The spanwise profile of $\overline{u'v'}$, figure 4.2(b), presents a local maximum at $y = 1$ where the flow jump intensifies the generation of turbulence. This feature is found also for the next class of flows, see panel (c) of the same figure.
- (b) The “Intermediate Flows” ($2 < r_h < 3$) are characterized by a dip in the mean velocity profile over the transition, see figure 4.2(a). According to Nezu et al. [1999] this effect is the signature of counter-rotating macro-vortices at the transition. The ratio between the peak main channel velocity and the floodplain velocity is 1.05 – 1.15 and, thus, weaker than for the “Shallow Flows”. The depth increase leads to a growth of the wall boundary layer thickness and macro-vortices are generated also in the floodplain close to the walls.



(a)



(b)



(c)

FIGURE 4.1: 2D free-surface velocity field for (from top to bottom) :
 (a) “Shallow Flows” ($r_h = 3.43$, $Fr = 0.46$),
 (b) “Intermediate Flows” ($r_h = 2.39$, $Fr = 0.54$), (c) “Deep Flows” ($r_h = 1.76$, $Fr = 0.58$). V_3 indicates the time-averaged velocity.

(c) The “Deep Flows” ($r_h < 2$) are characterized by a very weak shear in the transition region, but there is still influence of the compound channel geometry on the surface velocity profiles (see figure 4.2(a)). The ratio between the peak main channel velocity and the floodplain velocity is 1.00 – 1.05. The wall boundary layers increase in size and more and stronger macro-vortices are generated over the floodplains. However, the influence of the topography is much weaker and this can also be seen in the distribution of $\overline{u'v'}$ that is flatter except close to the lateral wall, panel (d) of figure 4.2.

4.2 Main properties of the macro-vortices

4.2.1 Vortex identification

A specific analysis to identify and to track vortical structures has been carried out. Among the many Eulerian techniques of vortex identification reported in the literature, we employed two methods: the first approach was based on the evaluation of the swirling strength $\lambda_{ci} > 0$, the second approach was the Okubo-Weiss criterion [Okubo, 1970, Weiss, 1991]. The former is commonly used in turbulence measurements to study coherent structures of turbulent flows [e.g. Adrian et al., 2000]. The swirling strength, defined as the positive imaginary eigenvalue of the local velocity gradients tensor, is large where there is a strong rotation of the flow, i.e. a vortex, Adrian et al. [2000], and automatically exclude regions of strong shearing. Generation of two dimensional macro-vortices has been observed for all values of the Froude number investigated. The classification of the flow regimes used to characterize the mean velocity profile can be applied also when the free surface vortical structures are considered. In fact, in the case of “Shallow Flows”, inspection of figure 4.3(a,b) reveals that the transition regions are dominated by large-scale macro-vortices and the sense of rotation is positive (anti-clockwise) for the left shear layer and negative (clockwise) for the right shear layer. The macro-vortices are aligned in the region with a spanwise distance between 0.5 and 1

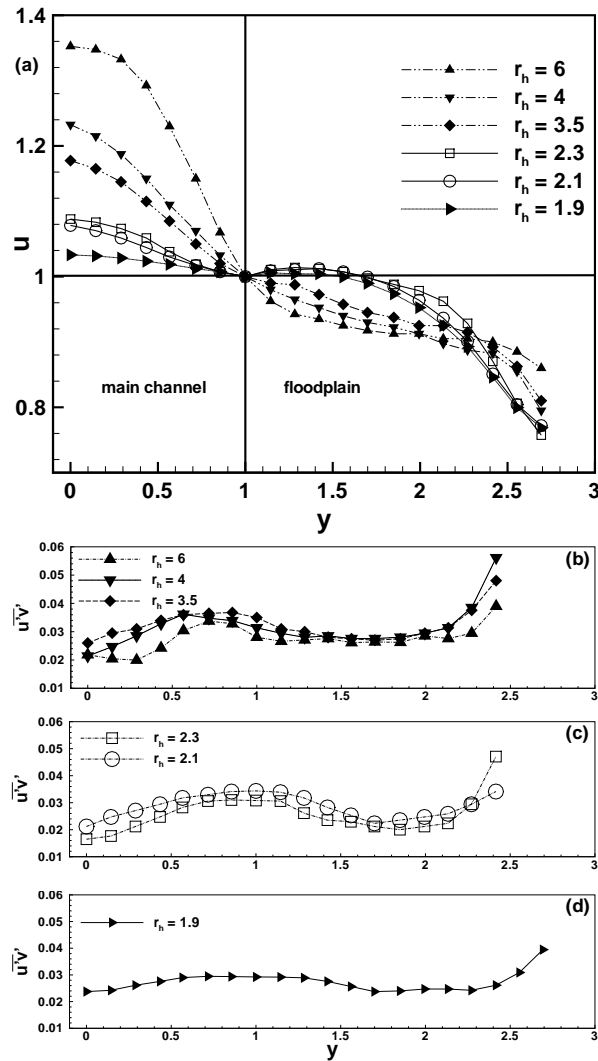


FIGURE 4.2: Mean streamwise surface velocity (a) and turbulence intensity (b,c,d) for different value of r_h .

channel half-widths from the main-channel axis, which corresponds to the region of high turbulence intensity. The macro-vortices remain confined in the transition region and almost no macro-vortices are present above the floodplains. Their formation can be explained in terms of the vorticity generation mechanism at the depth jumps described in Soldini et al. [2004]. Increasing the discharge leads to the “Intermediate Flows” for which the surface velocity is characterized by slightly weaker double shear layers in the transition regions and strong wall shear layers above the floodplains; this can be seen in

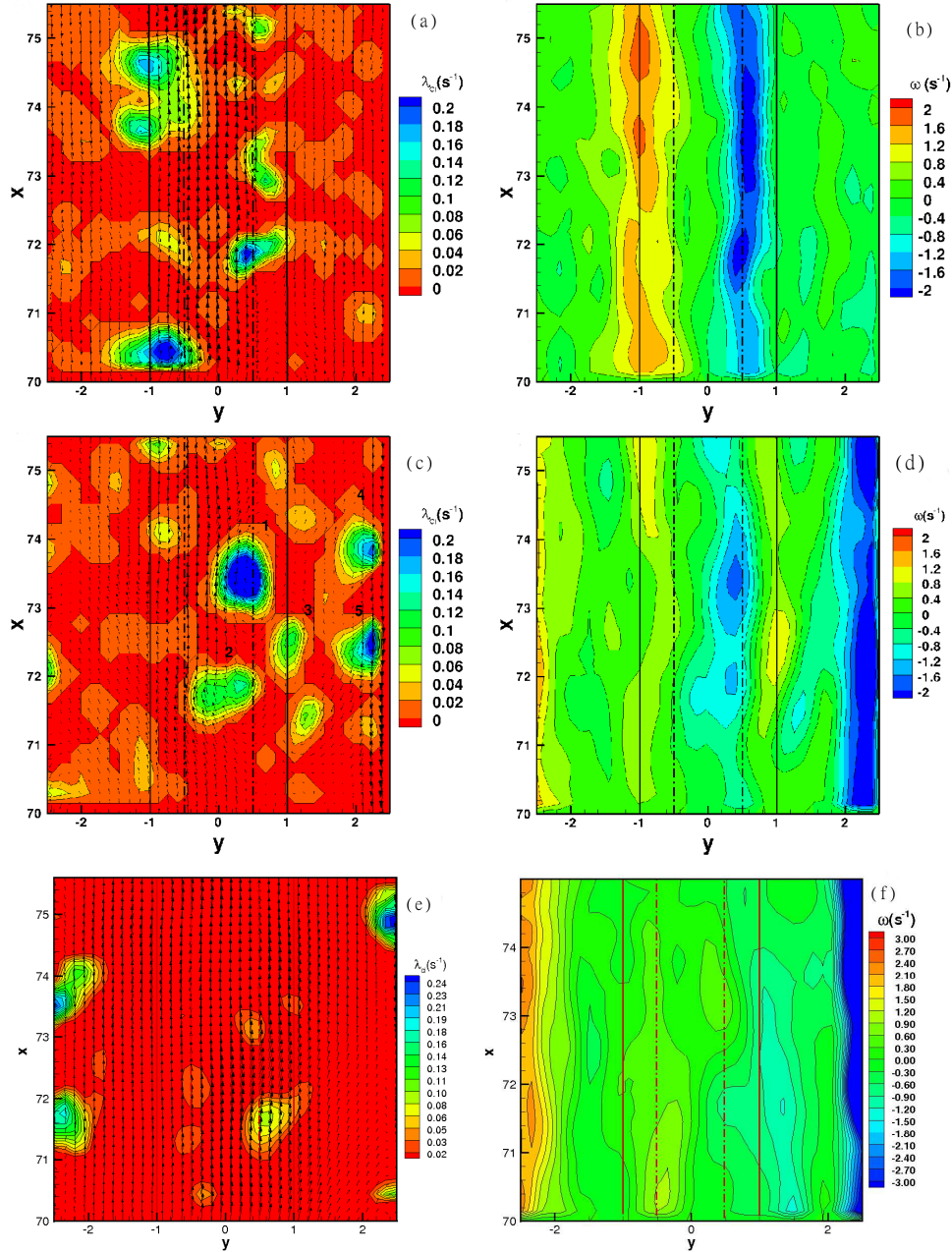


FIGURE 4.3: Left: velocity fluctuation by galilean decomposition $u'(x, y, t) = u(x, y, t) - \bar{u}(t)$ and swirling strength for "Shallow Flows" (panel (a)), "Intermediate Flows" (panel (c)) and "Deep Flows" (panel (e)). Right: the corresponding vorticity field (panels (b,d,f)).

the vorticity distribution as well as in the vortex positions in figure 4.3(c,d). For example, vortices 1, 2 and 3 are located in the transition region, vortices 1 and 2 rotate clockwise while vortex 3 rotates anti-clockwise. Vortices 4 and 5, both located in the wall shear layers, have negative vorticity and, therefore, rotate clockwise. Finally, for the “Deep Flows” (figure 4.3(e,f)) , macro-vortices are observed only close to the side walls and none is present at the transition region. In this case, the difference in the flow depth between the floodplains and the main channel is no longer an active mechanism to generate vorticity.

The second approach that we adopted was the Okubo-Weiss criterion [Okubo, 1970, Weiss, 1991] and its generalization to time-dependent flows [Hua and Kline, 1998]. These criteria enable both to partition the flow into regions with different dynamical properties and to characterize flows with a complex topology. By quantifying the local rate of separation of initially close trajectories, an attempt is also made to relate the nature of the stirring processes to the local topology of the flow. For steady flows, characterized by velocity gradients which are also slowly-varying in space, the Okubo-Weiss criterion makes use of the eigenvalue of the local velocity gradient tensor \mathbf{D}^* . The tensor \mathbf{D}^* is such that, for incompressible fluid, $\mathbf{D}^{*2} = \lambda_0^* \mathbf{I}$, where $\lambda_0^* = -\det(\mathbf{D}^*)$ is the product of the eigenvalue of the velocity gradient tensor. The Okubo-Weiss criterion consists in the evaluation of λ_0^* , which can also be written as [Weiss, 1991]:

$$\lambda_0^* = \frac{1}{4}(S^{*2} - \omega^{*2}), \quad (4.1)$$

where $S^{*2} = S_n^{*2} + S_s^{*2}$ is the total square strain, sum of the normal (S_n^*) and shear (S_s^*) components, and ω^{*2} is the square vorticity, which in a (x^*, y^*) , 2D flow has only the out-of-plane component ω_z^{*2} . Depending on the sign of λ_0^* , the flow has different local properties. The largest dispersion occurs in flow regions where $\lambda_0^* > 0$, here the flow can be taken as locally hyperbolic (strain overcomes rotation); on the other hand, where $\lambda_0^* < 0$ the flow is dominated by rotation, and it is assumed as locally elliptical. Hyperbolic regions, which act as fluid jets, are characterized by a local exponential divergence of nearby particles, on the contrary, elliptical regions are characterized by an approximate constant distance between adjacent particles.

For time-dependent flows Hua and Kline [1998] proposed an extension of the Okubo-Weiss criterion that requires the computation of the eigenvalues of the local acceleration tensor, which can be written as: $\mathbf{N}^* = \lambda_0^* \mathbf{I} + d\mathbf{D}^*/dt^*$. The Hua and Kline [1998] criterion is, then, based on the sign of the largest eigenvalue of \mathbf{N}^* , namely $\lambda_+^* = \lambda_0^* + \lambda_1^*$, where:

$$\lambda_1^* = \sqrt{\left(\frac{\partial S^*}{\partial t^*}\right)^2 - \left(\frac{\partial \omega^*}{\partial t^*}\right)^2}. \quad (4.2)$$

Both the above criteria provide a description of the flow in terms of stable elliptical regions and unstable hyperbolic regions, but the latter is closer to a pure Lagrangian point of view [Boffetta et al., 2001].

We first analyse the measured two-dimensional Eulerian velocity fields with the aim to distinguish regions with different dynamical properties, using the value and, more importantly, the sign of the eigenvalue λ_+^* , as suggested by Hua and Kline [1998]. An example of the computed values of λ_+^* is shown in figure 4.4 in the case of Shallow flow (a), Intermediate flow (b) and Deep flow (c) conditions. Similar results have been obtained using the Okubo-Weiss criterion based on the evaluation of the eigenvalue λ_0^* : the unsteady eigenvalue λ_1^* has been found to be always at least one order of magnitude smaller than λ_0^* . This suggests, as expected, that the flow under investigation is slowly varying in time. In the case of shallow conditions, the flow fields are dominated by large scale two-dimensional coherent structures, identified by large patches of negative λ_+^* , with a surrounding turbulent field characterized mainly by a low-intensity, positive eigenvalue. Among nearby vortical structures intense hyperbolic regions are clearly visible. The macro-vortices are observed at the transition region (indicated by the dash-dotted white lines in figure 4.4) where the flow depth jump is localized.

The vortex generation mechanism was discussed in detail by Soldini et al. [2004]. Fundamental results of this study are that the size of the macro-vortices scales with the downstream distance over which velocity fronts cross the depth jump and that the intensity of the macro-vortices depends on the depth jump itself.

In this experimental work, as described in Stocchino and Brocchini [2010], we

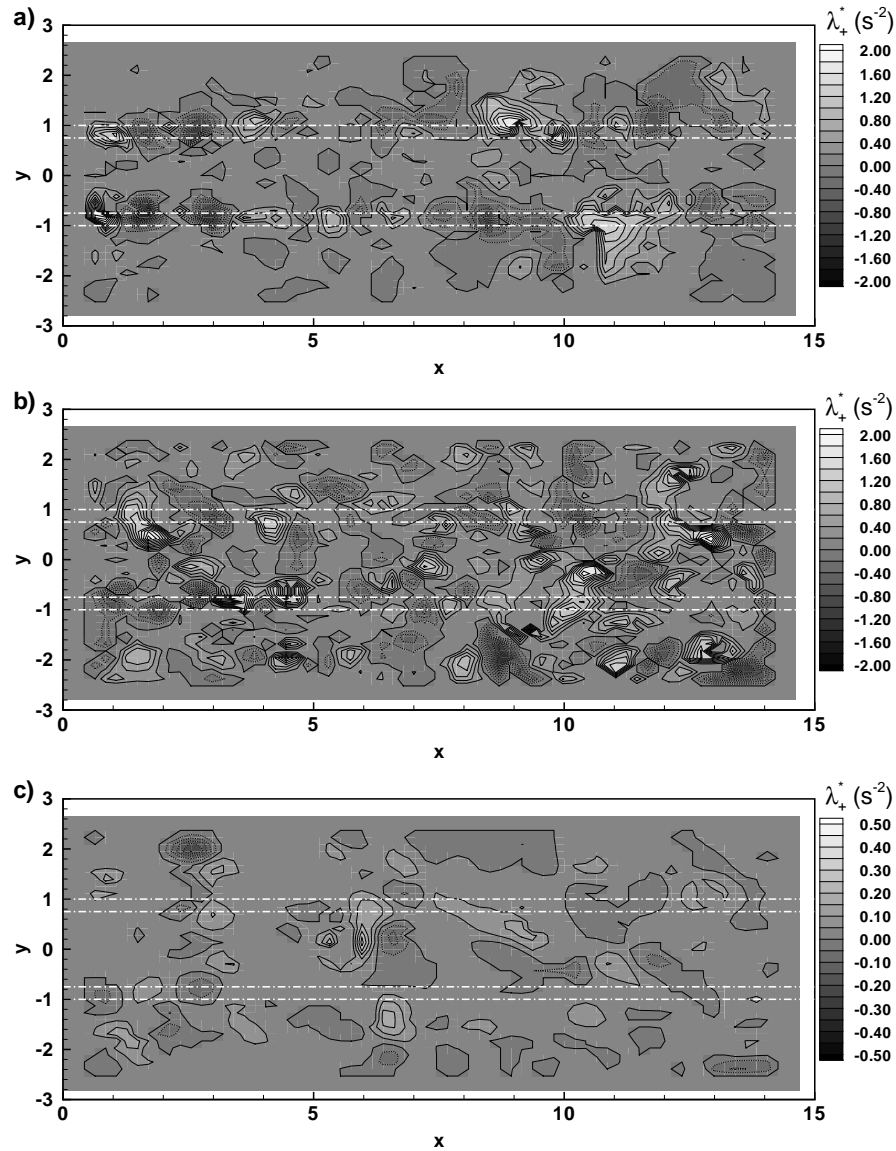


FIGURE 4.4: Examples of 2D maps of the positive Hua and Kline eigenvalue λ_+^* : (a) Shallow flow conditions (EXP201, $r_h = 4.16$, $Fr = 0.60$), (b) Intermediate flow conditions (EXP205, $r_h = 2.04$, $Fr = 0.76$) and (c) Deep flow conditions (EXP112, $r_h = 1.28$, $Fr = 0.142$). The dotted-white lines indicate the transition regions of the compound channel. For the Deep flow the contour range has been reduced.

observed that the size of the macro-vortices scales well with that of the transition region and that these coherent structures remain confined within the transition regions while they are convected downstream by the mean flow. The quasi-2D macro-vortices behave as organized domains with a distinct dynamical role. On the contrary, for lower values of the flow depth ratio r_h , corresponding to Intermediate flow conditions, the Hua and Kline [1998] eigenvalue is more randomly distributed in the domain and fewer macro-vortices can be recognized, located either in the transition regions or in the floodplains. The background turbulent field is, in this case, characterized by a distribution of λ_+^* oscillating between moderate positive and negative values. Decreasing further r_h , i.e. moving to deeper flow conditions, the distribution of the Hua and Kline [1998] eigenvalue is even more uniform and less intense than in the previous case (the range of the contour levels has been reduced to improve the plot quality). The non-organized background turbulence occupies most of the flow domain and dominates the dynamics.

4.2.2 Main features of the macro-vortices

The resulting maps of distribution of both the Hua and Kline [1998] eigenvalue and the swirling strength have been used to study the main geometrical features and their evolution of the vortical structures by a statistical analysis. In particular, we could infer the position of the core of the vortex, the area occupied by the vortex Ω , the radius of the area-equivalent circle R_{eq} , and other geometrical characteristics of interest, e.g. the eccentricity ϵ of the vortices, the maximum radius R_{max} and the inclination angle θ with respect to the mean flow direction x (see figure 4.5). Normalized probability Density Functions (PDFs) of the above features have been obtained. The total number of vortices revealed during a single experiment ranges between 200 and 400.

It was first fundamental to evaluate the characteristics of their generation which, as above described, seems to be mainly concentrated in the transition region for “Shallow Flows” and at the lateral walls for “Intermediate” and “Deep Flows”. Macro-vortices of different sizes are generated depending on

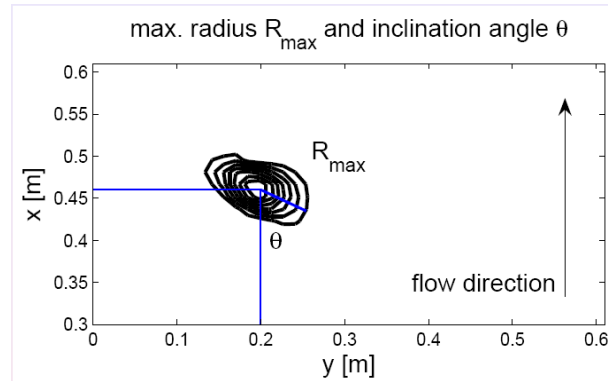


FIGURE 4.5: Swirling strength of a single vortex core with maximum Radius R_{max} and inclination angle θ

the Froude number. To detail such dependencies we have analyzed both the PDFs of the vortex area-equivalent radius (figure 4.6(a-d)) of both transition region vortices (represented by lines with triangles) and wall vortices (represented by lines with squares). For Shallow Flows ($r_h > 3$), vortices are found to reside mainly in the transition region and with typical size in the range (0.025–0.035)m. For “Intermediate” and “Deep Flows” macro-vortices both increase in size and frequency over the floodplains, the transition region exhibiting a decreasing vortex content. It is also interesting to note that, generally, floodplain vortices are smaller than those generated at the transition region. The fundamental result is that the mean vortex radius is always in the range $0.025\text{m} \leq R_{eq} \leq 0.035\text{m}$, which compares well with the transversal size of the transition region (0.05m).

Besides the distribution of the equivalent radius, we have analyzed also the shape of the vortical structures observed either on the transitional regions or on the floodplains. In particular, we have computed the eccentricity ϵ , defined as the ratio between the major and minor axes of the vortex, which is a measure of the vortex symmetry ($\epsilon = 1$ represents a perfectly circular vortex). PDFs of ϵ are reported on figure 4.6(e-h), with the same graphical arrangement used for R_{eq} . In the “Shallow Flows” regime transitional macro-vortices are rather elongated with values of $\epsilon \approx 0.55 - 0.60$. On the contrary, for smaller ratios r_h , the vortices, which are more concentrated over the floodplains, are characterized by a similar distribution of eccentricity peaked

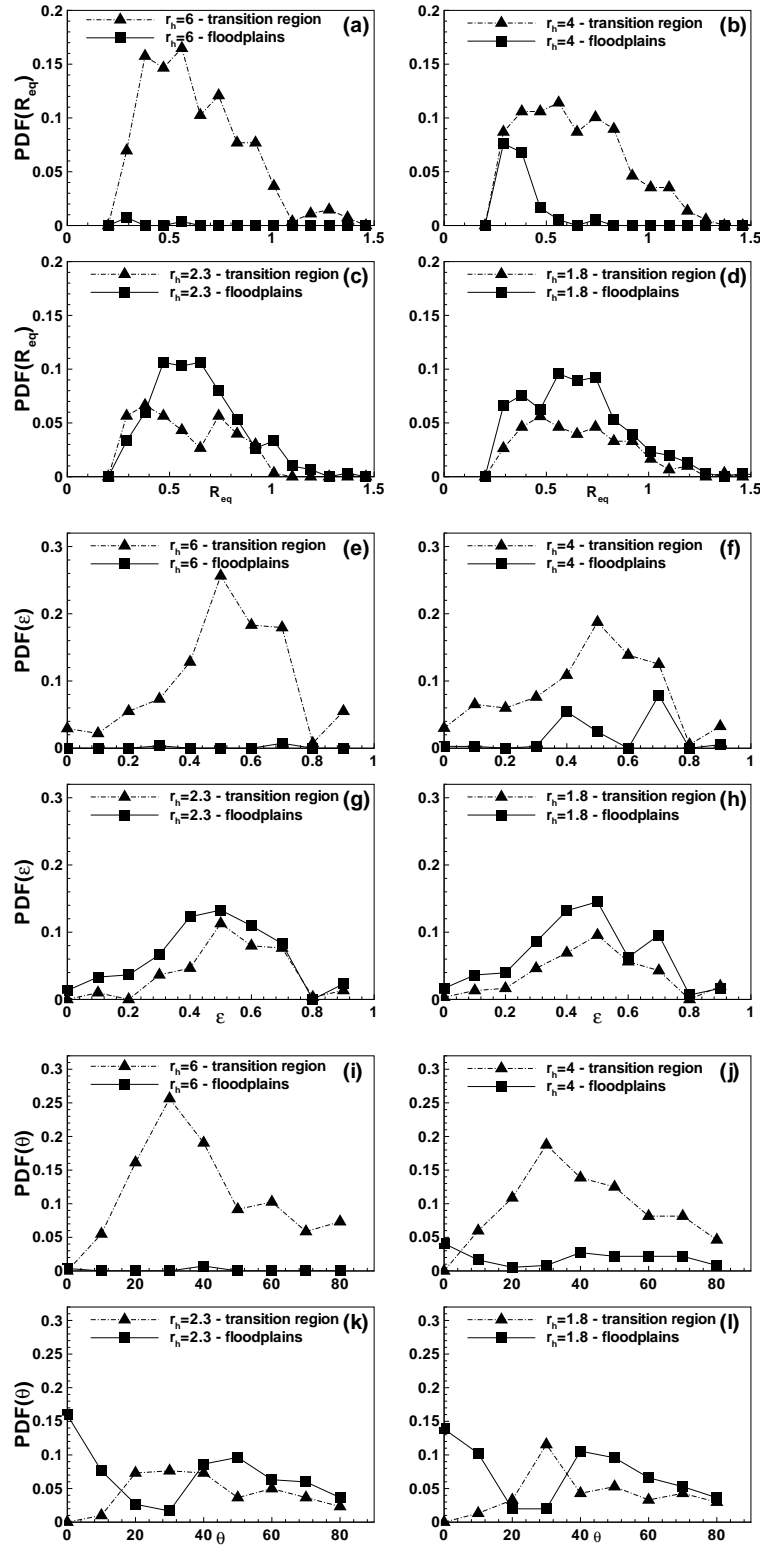


FIGURE 4.6: PDFs of macro-vortex size and shape. PDF of the equivalent radius R_{eq} , vortex eccentricity ϵ and the alignment angle θ for different depth ratios.

at $\epsilon \approx 0.5$ and $\epsilon \approx 0.7$, suggesting that wall-vortices are slightly rounder than those generated at the transition region. In the case of 2D free turbulence, it has been found that elliptical vorticity patches are, in general, unstable. Due to the difference in rotation between the vortex core and the edges, elliptical vortices are subjected to filamentation and, ultimately, they tend to become circular. This process is known as “axisymmetrization” [see Tabeling, 2002, and cited references]. In the present case, the latter process is likely to be inhibited by the topographic forcing and the resulting background shearing, causing the vortical structure to remain more elongated.

Finally, we have calculated the PDFs and mean values of the angle θ that expresses the orientation of the main axis of the vortex with respect to the mean flow (perfect vortex-mean flow alignment is achieved for $\theta = 0$). The PDFs are, again, reported in figure 4.6(i-l). For “Shallow Flows” macro-vortices are observed to be oriented to the mean flow with an angle $\theta \approx 40^\circ - 50^\circ$. Increasing the Froude number, the vortices, mainly concentrated along the lateral walls, are characterized by a bimodal distribution of orientation peaked at $\theta \approx 0^\circ$ and $\theta \approx 50^\circ$, whereas macro-vortices generated at the transition regions are characterized by a broader orientation distribution. This suggests that wall-vortices are, on average, more aligned with the mean flow than those generated at the transition region. Moreover θ , independent of dU/dy over the transition region and weakly decreasing over the floodplain, ranges, in average, between 20° and 50° . Thus, in general, macro-vortices are not parallel to the main flow and those covering the transition region are not sensitive to the mean shear (a decrease of θ with dU/dy is expected for alignment due to shearing) and those over the floodplains are weakly aligned by the mean shear. In other words, the transition region macro-vortices are believed to weakly engulf the floodplain fluid more similarly to what happens for wakes than for jets/shear layers. In fact, the shear at the transition region of a jet is strong enough to align the interface vortices parallel to the mean interface; this does not happen for wakes [Mobbs, 1968].

As a result of the characterization of the fundamental features of the compound channel flow, it was possible to discuss similarities and clear differences with a free shear layer flows induced by the meeting of shallow streams of different speed. In this respect, a first difference is made evident by the mean

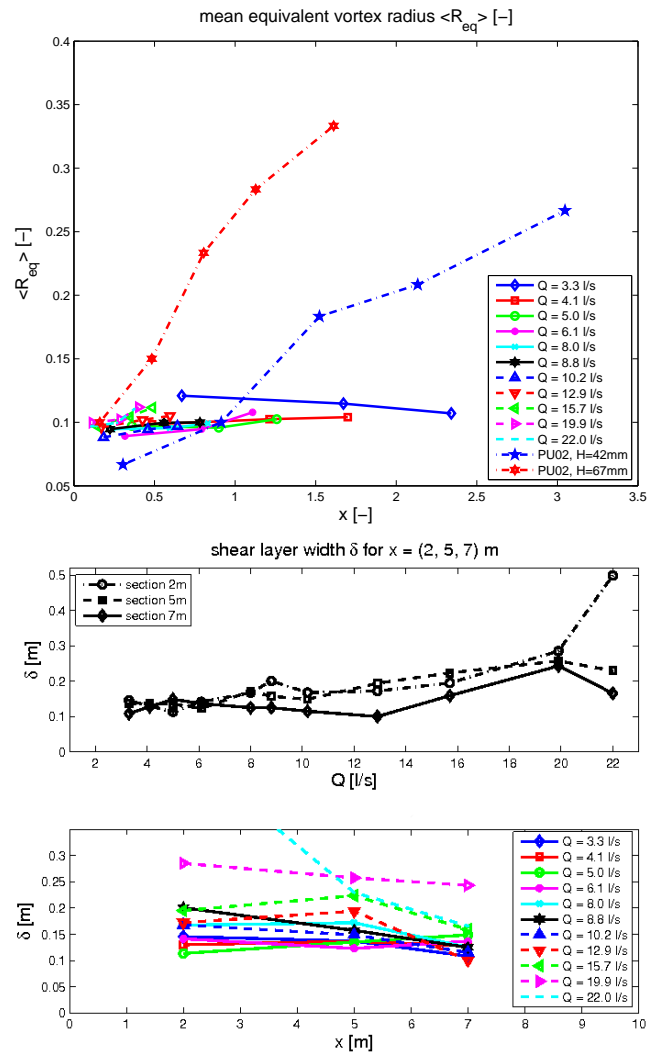


FIGURE 4.7: Top panel: normalized mean vortex radius R_{eq} over normalized downstream distance $x[-]$ for all discharges and experiments of van Prooijen and Uijttewaal [2002] Bottom panel: Shear layer thickness δ as a function of discharge Q and downstream distance x .

flow profile shown in figure 4.2. For most of the values of the depth ratio r_h , a non-monotonic profile characterizes the fully-developed flow. Hence, bell-type function, typically used as self-similar solutions for free shear layers Chu et al. [1991], van Prooijen and Uijttewaal [2002], is inadequate to represent the mean flow in a compound channel. Moreover, although horizontal mixing is governed by the quasi-2D macro-vortices in both flows, differences are expected, because the vortical structures of the two flows seem to have rather different properties. Such a difference is easily appreciated by inspecting figure 4.7 (top panel), which illustrates, in suitable dimensionless form, the downstream growth of R_{eq} for the macro-vortices observed in the present experiments (solid and dashed lines) and those measured in free shear flows by van Prooijen and Uijttewaal [2002] (dashed-dotted lines). While the former have a size almost constant with x , the latter ones grow in size at a considerable rate. This is consistent with the fact that the thickness δ of a free shear layer is expected to grow linearly in the streamwise direction, whereas in the case of compound channels δ remains constant, as soon as the flow is fully developed, see figure 4.7 bottom panels. The dependence of δ on the flow discharge is also shown in the same figure. This is a reflection of the fundamental fact that the size of compound-channel macro-vortices scales with the crossflow size of the transition region, which remains constant along x , [Piattella et al., 2006, Soldini et al., 2004] whereas shear-layer macro-vortices scale with the shear layer width that increases downstream of the inception [see figure 5 of van Prooijen and Uijttewaal, 2002]. Moreover, macro-vortices are also found to reside in different spatial regions in the two flows. In the case of a free shear layer the vortex position, coinciding with that of the shear layer, is seen to bend towards the low-velocity region of the shear layer [van Prooijen and Uijttewaal, 2002]. On the contrary, in a compound channel, not only the lateral walls provide an extra agent for vortex generation (mainly confined over the flood plains), but also transition-region macro-vortices are found to reside over the transition region only.

Chapter 5

Lagrangian statistics

5.1 Absolute properties

We start the study of the Lagrangian mixing with the analysis of single particle statistics evaluated from the numerical trajectories, see equations (2.17) and (2.19).

Once the two-dimensional Eulerian velocity fields have been obtained, an ensemble of particle trajectories has been computed. This approach, namely to calculate numerically the particle trajectories starting from measured Eulerian fields, is commonly adopted in mixing studies [Lekien et al., 2005]. We calculated particle trajectories using a fourth-order Runge-Kutta algorithm with adaptive step size, which has a local accuracy of order $(\Delta t^*)^4$, where Δt^* is the integration time step. In more detail, for each flow field we inseeded the experimental flow with approximately $\mathcal{O}(10^4)$ “numerical particles” (massless) on a regular grid (of constant size Δx^* and Δy^*) and, subsequently, evaluated the tracers’ trajectories by integrating (2.15) in time with the mentioned Runge-Kutta algorithm employing a bi-cubic spatial interpolation and a polynomial time interpolation of the experimental Eulerian fields. From the ensemble of particle trajectories the single or absolute particle statistics, dispersion and diffusivity, have been evaluated.

The evaluation of the single-particle statistics has been performed after removal of a mean velocity profile from the Eulerian fields. In particular, the

ensemble-averaged velocity along the y -direction vanishes ($\overline{V}^*(x^*, y^*) = 0$), while along the x -direction the ensemble-averaged velocity $\overline{U}^*(x^*, y^*)$ assumes a bell-like profile, with the maximum located in the main channel and a velocity gradient at the transition between the main channel and the floodplains [Stocchino and Brocchini, 2010] which is stronger for shallower flows. It is, therefore, necessary to remove the mean flow prior to evaluating the absolute statistics. This issue has been rigorously studied by Davis also in connection with ocean dynamics [Davis, 1982, 1983]. For each Eulerian velocity field the mean velocity $\overline{U}^*(x^*, y^*)$, varying along the longitudinal and the transversal direction, has been subtracted from the instantaneous longitudinal velocity $u^*(x^*, y^*, t^*)$. For a 2D flow evolving in the (x^*, y^*) - plane the residual velocity field then reads:

$$\mathbf{u}^{*'}(x^*, y^*, t^*) = \mathbf{u}^*(x^*, y^*, t^*) - \overline{\mathbf{U}}^*(x^*, y^*) \quad (5.1)$$

where $\overline{\mathbf{U}}^*(x^*, y^*)$ indicates the velocity averaged over the duration of the single realization. This method is adequate to handle flows that are inhomogeneous, like in the present case or in oceanographic applications, while the classical results of Taylor were obtained assuming $\mathbf{U}^*(x^*, y^*) = 0$, i.e. for homogeneous flows. The absolute statistics are, then, derived from the residual velocities.

To test if the particle trajectories reach quasi-stationary conditions, we have computed the mean Lagrangian kinetic energy, defined in the equation (2.16). The Lagrangian kinetic energy together with its Eulerian (E_E^*) counterpart is illustrated for sample Shallow and Deep flow conditions in figure 5.1. By inspecting figure 5.1 it is clear that E_L^* and E_E^* attain very close values which are also almost constant over the entire duration of the experiments, residual fluctuations are due to low-frequency turbulent events.

5.1.1 Time scales and growth law

We have first evaluated the Lagrangian integral time scales T_{uL}^* and T_{vL}^* , using the procedures described in Guala et al. [2007] and Luo et al. [2007], for each experiment and for both the Lagrangian residual components $u_L^{*'}$

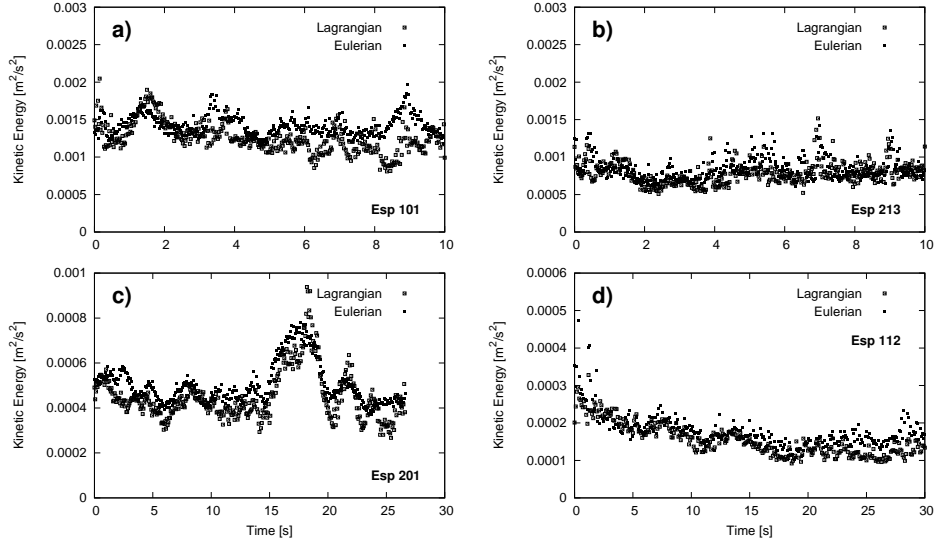


FIGURE 5.1: Eulerian and Lagrangian kinetic energy (respectively E_E^* and E_L^*) for Shallow flows (panel a: EXP101 ($r_h = 3.69$, $Fr = 0.88$); panel c: EXP201 ($r_h = 4.16$, $Fr = 0.60$)) and Deep flows (panels b: EXP213 ($r_h = 1.68$, $Fr = 0.82$); panel d: EXP112 ($r_h = 1.28$, $Fr = 0.14$)).

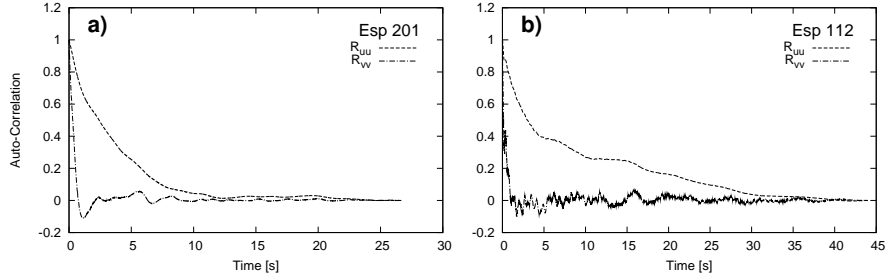


FIGURE 5.2: Autocorrelation for: (a) Shallow flows (EXP201, $r_h = 4.16$, $Fr = 0.60$) and (b) Deep flows (EXP112, $r_h = 1.28$, $Fr = 0.14$).

and v_L^* . Therefore, the Lagrangian normalized autocorrelation of the i -th velocity component has been computed using equation (2.22). Typical examples of the Lagrangian normalized autocorrelation function for the streamwise $\mathcal{R}_{uu}(\tau^*)$ and spanwise $\mathcal{R}_{vv}(\tau^*)$ direction are shown in figure 5.2 for one sample Shallow flow (panel a) and one sample Deep flow (panel b). Clearly the spanwise autocorrelation decays more rapidly than the streamwise autocorrelation, leading to a much smaller Lagrangian integral scale, thus highlighting the fact that quasi-uniform flows in compound channels are fundamentally

unidirectional. Moreover, the results of the cross-stream correlation for the Shallow flow show a clear initial dip, indicating the presence of trapping vortices, while the results for the Deep flow condition display a correlation with a lower energy and a noisy shape. Such a result suggests, as pointed out by Guala et al. [2007], that Shallow flows are dominated by macro-vortices, while Deep flows are, mainly, shear-dominated flows. Starting from the Lagrangian time integral scales the corresponding spatial integral scales (L_{uL}^* , L_{vL}^*) can be easily computed. The computed values of the Lagrangian time scales for all the experiments are listed in table A.1, together with values of the Eulerian integral scales (T_{uE}^* , T_{vE}^*), which have been calculated as the time integrals of the normalized Eulerian autocorrelation functions (the Eulerian integral scales are always greater than the Lagrangian scales). In the following, the results are given in dimensionless form (unstarred variables) using the quantities defined above (T_{uL}^* , L_{uL}^*) together with the time-averaged Lagrangian kinetic energy E_L^* to make dimensionless the absolute dispersion and diffusivity.

5.1.2 Absolute dispersion and diffusivity

The dimensionless absolute dispersion a^2 is a function of time as shown by the sample cases (Shallow flow of EXP201, Intermediate flow of EXP205 and Deep flow of EXP112) illustrated in figure 5.3. One first, significant, difference between the flow regimes is that a^2 shows a non-monotonic behaviour in the Shallow flow conditions (see range $0.2 \leq t^*/T_{uL}^* \leq 2$), whereas it monotonically increases with time in the Deep flow experiment. A similar behaviour has been described in Elhmaïdi et al. [1993], where the single-particle dispersion has been studied by purely-2D numerical simulations characterized by few long-lived, large-scale vortices immersed in an almost homogeneous turbulent background. In that case, the Authors justified the non-monotonic trend of a^2 by the influence of the macro-vortices on the flow mixing. In particular, they analysed two different initial conditions: 1) a uniform seeding over the entire domain, 2) a seeding localized in the vicinity of an isolated vortex. The latter initial condition led to the non-monotonic behaviour, whereas the dispersion observed in the case of uniform seeding was mainly forced by

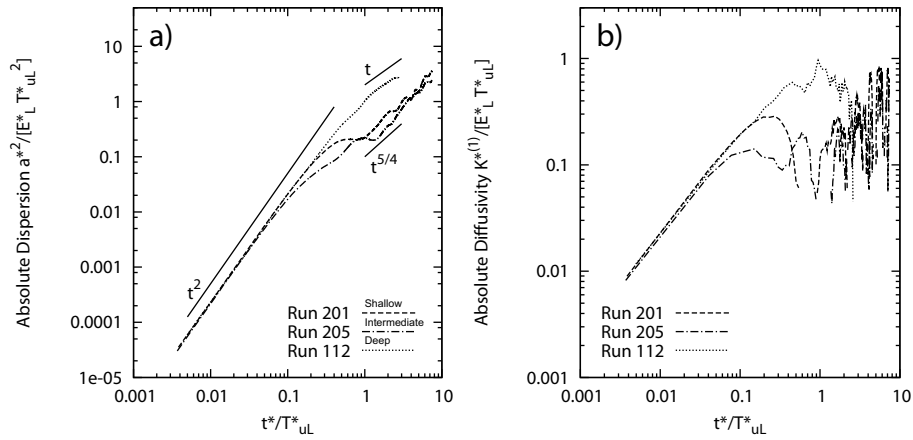


FIGURE 5.3: a) Absolute dispersion; b) Absolute diffusivity. EXP201: $Fr = 0.6$, $r_h = 4.16$; EXP205: $Fr = 0.69$, $r_h = 5.57$; EXP112: $Fr = 0.14$, $r_h = 1.28$.

the background turbulence rather than by the macro-vortices, which occupied a small portion of the entire domain. It is interesting to note that for the Shallow flows the absolute dispersion is a non-monotonic function of time even if we seeded the domain with an initial homogeneous distribution of particles. This suggests that for the present class of flows the dominant dynamical features are the transitional macro-vortices, which control the overall dispersive process. On the contrary, such vortical structures are almost absent in the case of Deep flows with a consequent smoother dispersive process. If we now analyze in detail the results shown in figure 5.3, the single-particle dispersion of EXP201 is seen to be characterized by different regimes. An initial ballistic regime is observed until a^2 reaches a local maximum at a value that is related to the typical size of the macro-vortices: for the specific case shown, $a^2 \simeq 0.2$ corresponds to a length of about $\sqrt{a^2} = 0.45$. This compares well with the dimensionless transition region ($L_i = W_{tr}^*/L_{uL}^* = 0.36$) which, recalling the studies of Soldini et al. [2004] and of Stocchino and Brocchini [2010], provides a suitable scale for the macro-vortices. In view of this and of some results which follow, we regard this scale as the “injection scale” $L_i = W_{tr}$ for the turbulence energy. Moreover, the time for which the local maximum of the absolute dispersion occurs is of the same order of magnitude as the vortex turnover time ($\sim 3T_T$), defined as $T_T = 1/\sqrt{2Z^2}$, where Z^2 is the total enstrophy (calculated as the ensemble averaged square vorticity).

In table A.1 the values of the dimensionless turnover time are reported for all the experiments, where the turnover time has been made dimensionless with the Lagrangian integral time scale. It is possible to evaluate a dimensionless turnover length scale (L_T) associated with T_T . A simple inspection of the available data shows that $1.5 \leq L_i/L_T \leq 3.5$. The absolute dispersion attains such a local maximum as soon as the particles trapped in coherent vortical structures undergo almost regular oscillation on a length scale comparable with the vortex diameter.

For longer times, particles are influenced by the straining regions that surround the large-scale structures and the absolute dispersion increases with time following a power law with an exponent closer to $5/4$, as also described in Elhmaïdi et al. [1993]. Finally, after such an intermediate regime, a^2 grows with t following a dependence which resembles that of a Brownian regime ($a^2 \propto t$). At this stage, the influence of the macro-vortices is less vigorous and the background turbulence dominates the mixing.

Decreasing the flow depth ratio r_h the Intermediate flows are characterized by the simultaneous generation of macro-vortices both at the transition region and at the sidewalls. In this case, transitional macro-vortices still strongly influence the growth of the absolute dispersion a^2 leading to a close similarity with the Shallow flows as shown in figure 5.3, EXP205.

Decreasing further r_h , we reach the Deep flows. In this case, the behaviour of the single-particle dispersion is mainly monotonic with no evidence of oscillations in the intermediate regime, as observed for the Shallow and Intermediate flows. Especially in the case of EXP112, characterized by very deep conditions ($r_h = 1.2$), the Brownian regime is clearly attained after a time of about $(1.3 - 1.5)T_{uL}^*$. The absence of transitional coherent vortices in Deep flows leads to a more regular transition from the initial ballistic regime towards a fully-developed Brownian regime.

Given the behaviour of the absolute dispersion shown in figure 5.3a, the corresponding absolute diffusivity $K^{(1)}$, i.e. the time derivative of a^2 is, not surprisingly, rather irregular except for the initial ballistic regimes. This is a direct consequence of the non-monotonic behaviour of a^2 . However, for large times the absolute diffusivity seems to oscillate with an almost-constant upper bound, resembling what would occur in the case of an equilibrium regime.

The large time asymptotic behaviour of mixing characteristic will be better discussed in the next chapter in order to characterize typical values diffusivity coefficient.

We have evaluated the anisotropy of the absolute statistics by computing separately $A_x^{(2)}$, $A_y^{(2)}$, $K_x^{(1)}$ and $K_y^{(1)}$, these being, respectively, the contributions to the total absolute dispersion and diffusivity in the x and y directions (see figure 5.4). In the case of Shallow flows (EXP201, figure 5.4 panels a and b) the dispersions in the streamwise and spanwise direction are fairly close, indicating a weak anisotropy. In this class of flows, dominated by large-scale vortices, the contribution of the coherent structures produces an intense dispersion in both directions, especially for long times. On the contrary, the few macro-vortices which characterize the Deep flows (EXP112, figure 5.4 panels c and d) are unable to trigger significant mixing processes in the transverse direction (y), leading to a stronger anisotropy with a difference of approximately one order of magnitude.

5.2 Relative properties

5.2.1 Shallow flows

The behaviour of the relative diffusivity $K^{(2)}$ versus the initial separation $r = r^*/L_{uL}^*$ is shown in figure 5.5; as postulated by Bennett [1984], relative diffusivity follows a power law of the type $K^{(2)} \propto r^\beta$. The computation of the relative diffusivity is performed by time differentiating the squared separation $r^2(t)$, which has small amplitude high frequency oscillations. Therefore, the time derivatives becomes a rather noisy signal. However, the trend of the envelope of the relative diffusivities for different initial separations allows for an identification of power law in $r(t)$.

In the case of Shallow flow conditions the results suggest that the growth of the relative diffusivity follows two distinct power laws depending on the scale of the separation, namely for small separation $K^{(2)} \propto r^{1.8-2.0}$ and for large separations $K^{(2)} \propto r^{1.5}$. The change of the growth regime seems to occur for

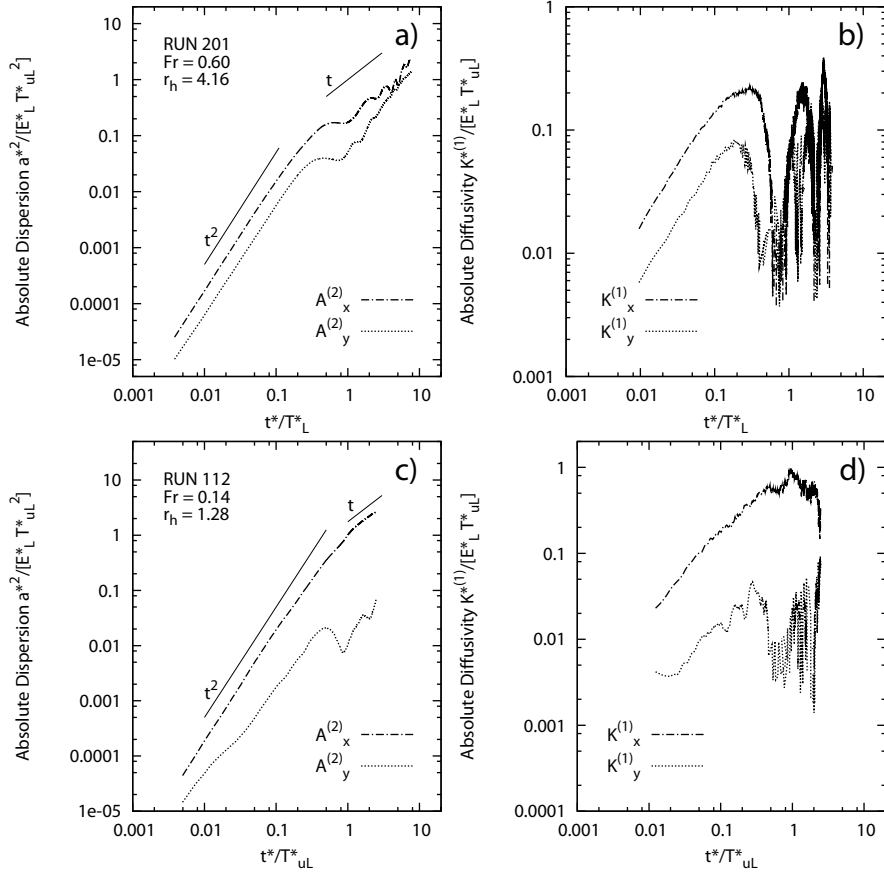


FIGURE 5.4: Plots of $A_x^{(2)}$, $A_y^{(2)}$, $K_x^{(1)}$ and $K_y^{(1)}$ for the Shallow flow of EXP201, panels a) and b), and for the Deep flow EXP112, panels c) and d).

distances smaller than the spatial integral scale (L_{uL}^* , i.e. $r = 1$), suggesting the existence of another length scale that plays a significant role in the mixing dynamics. More precisely, the regime with exponent $1.8 - 2.0$, which we regard as a first indication of a direct enstrophy cascade, persists as long as the particle separations remain below the values of 0.2 for EXP101 and of 0.4 for EXP201 (see figure 5.5). These approximately correspond to the turbulence “injection length scale” L_i that has already been highlighted to be the typical scale of generation of vorticity (hence turbulence) in a compound channel flow. Note that, typically, it is $0.2L_{uL}^* \leq L_i \leq L_{uL}^*$. We postulate that for $r < L_i$, $K^{(2)}$ increases as it would occur for a direct enstrophy cascade regime while for $L_i < r < 1$, $K^{(2)}$ increases at a lower rate (1.5) which we postulate to be compatible with an inverse energy cascade process (classical

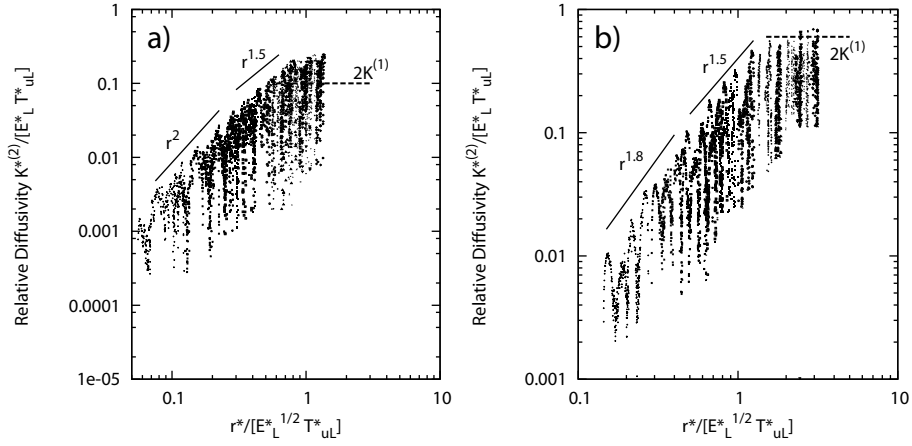


FIGURE 5.5: Relative diffusivity as function of the dimensionless separation r for Shallow flow conditions ($r_h > 3$): a) EXP101; b) EXP201.

rate of $4/3$). In more detail, particle pairs initially separated by a distance smaller than L_i will experience both growth regimes, i.e. exponential in time ($K^{(2)} \propto r^2$) for $r < L_i$ and cubic in time ($K^{(2)} \propto r^{1.5}$) for $r > L_i$, whereas particle pairs with initial separation greater than L_i , will grow cubically in time up to the largest scales of the flow.

As already described in chapter 2, an inverse energy cascade is the result of a specific dynamics of coherent vortical structures that undergo vortex merging, transferring in this way energy from the smaller to the larger scale. Indeed, vortex merging has been observed during the experiments run with Shallow flow conditions, as shown in figure 5.6, where contours of the Okubo-Weiss eigenvalue of consecutive flow fields are displayed. Being aware that the detailed merging mechanism is still an open issue, λ_0 has been used only for the purpose of helping the identification of the merging of the vortices. For convenience, we have plotted only the negative contours of λ_0 that corresponds to elliptical regions (vortices). It can be seen that vortices residing in the transition regions merge together leading to larger flow structures.

Further evidence of the presence of an inverse energy cascade occurring in Shallow flow conditions can be found by means of the dimensionless Eulerian Power Spectral Density (PSD) function $S_u(k^* L_i^*)$ of the streamwise (u) velocity component, where the wavenumber k^* has been made dimensionless using $W_{tr}^* = L_i^*$. The PSD functions have been normalized with the friction

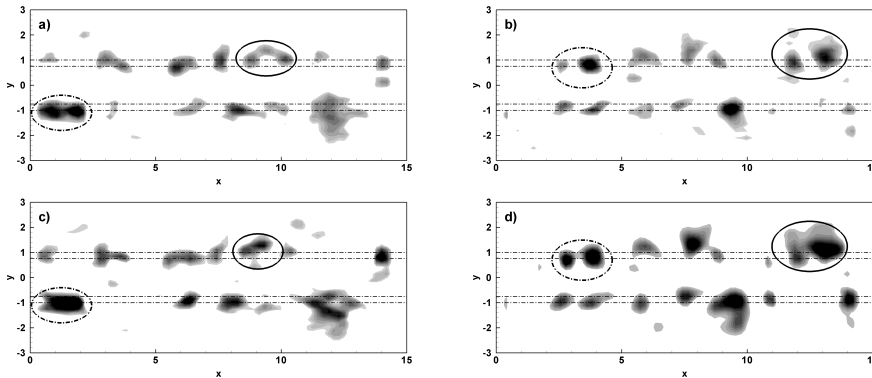


FIGURE 5.6: Contours of the Okubo-Weiss eigenvalue λ_0 showing vortex merging in the case of a Shallow flow (EXP201, $r_h = 4.16$, $Fr = 0.60$). Merging events are highlighted by solid ellipses and occur around $(x, y) = (1, -1)$ and $(x, y) = (9, 1)$ at two subsequent times, panels a) and c), and around $(x, y) = (3, 1)$ and $(x, y) = (13, 1)$ at two subsequent times, panels b) and d). The dotted-black lines indicate the transition regions of the compound channel. Note that only negative values of λ_0 have been displayed.

velocity u_* defined as $u_* = \sqrt{gh_{mc}^*S}$. Owing to the limited size of the velocity series in space, the computation of the PSD has been carried out in terms of frequency $S_u(f^*)$ and, subsequently, evaluated in terms of wavenumbers by dividing each frequency by the time and space-averaged surface velocity U_s^* , $k^* = f^*/U_s^*$, under the assumption of “frozen turbulence”, as suggested by Nikora et al. [2007] in a similar context of free surface flows. Examples of dimensionless PSDs are reported in figure 5.7 for the Shallow flow cases (EXP101 and EXP201). The figure illustrates the coexistence of two different regimes, separated at around $k^*L_i^* = k^*W_{tr}^* = 1$ i.e. at an injection scale comparable with the transition region width W_{tr}^* .

Additional information on dispersion dynamics can be achieved from the analysis of the PDFs of the particles’ displacements. The main advantage in using the time dependence of the PDFs is the possibility of distinguishing different dispersion regimes characterized by the same dependence of $K^{(2)} \propto r^\gamma$ on the basis of the Gaussianity/non-Gaussianity of the PDFs. Generally, the analysis of time dependence of the *kurtosis* should agree with the results obtained in terms of relative diffusivities, beyond providing extra information on the characteristics of the dispersion regimes [LaCasce, 2008]. For Shallow

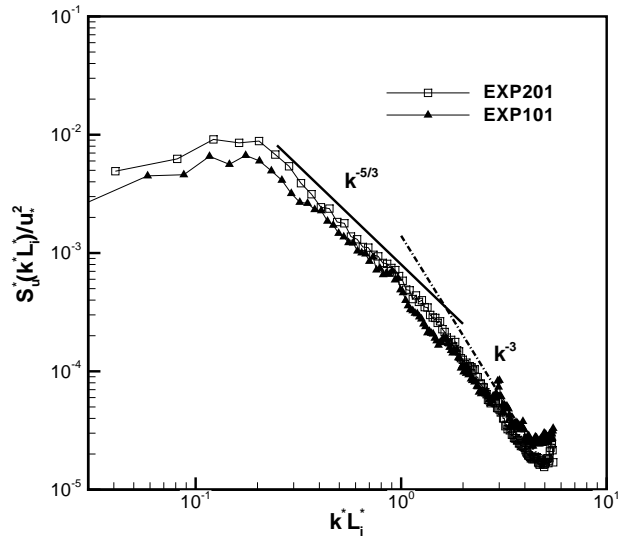


FIGURE 5.7: Normalized Eulerian Power Spectral Density function S_u corresponding to the Shallow flows experiments of figure 5.5.

flows the kurtosis as a function of time, and the PDFs at a dimensionless time equal to $t = t^*/T_{uL}^* = 2$ are shown in figures 5.8.

The two regimes found on the basis of the results of relative diffusivity are characterized by two different behaviours of the kurtosis. Separations smaller than the injection scale ($L_i = 0.36$), namely $r_0 = 0.14$ and $r_0 = 0.21$, are characterized by a large values of ku , which is almost constant for times longer than the integral time scale ($t = 1$) and far from the Gaussian conditions, see the PDFs distributions (bottom panels of figure 5.8). On the contrary, larger separations ($r_0 = 0.72$ and $r_0 = 1.44$), after an initial rapid decrease of ku , become quasi-Gaussian with a value of ku slightly larger than 3. The corresponding PDF distributions possess, in this case, rounder peaks and shorter, thinner tails.

The analysis of the relative statistics suggests that an equilibrium (Brownian) regime, where $K^{(2)} \propto 2K^{(1)}$, is attained for any value of r_h and Froude number once dimensionless separations are larger than 2. However, the results in terms of relative statistics are affected by strong oscillations. This may be due to the accuracy in computing relative quantities at large scales.

An alternate approach is to use the distance as the independent variable and average the times of mixing. In other words, the Finite Scale Lyapunov Exponents (FSLEs) are obtained by recording the times required for individual

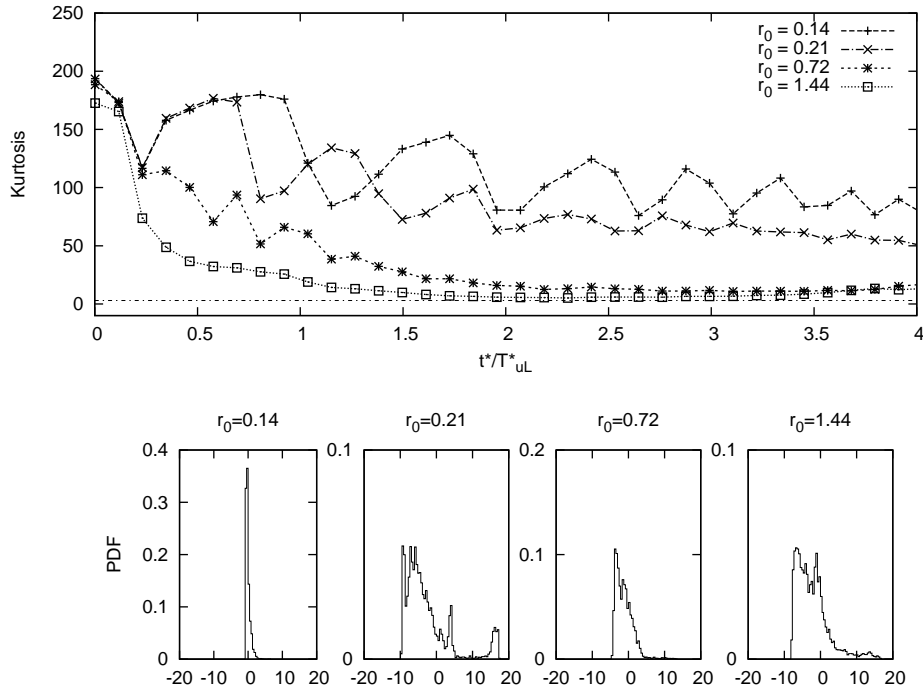


FIGURE 5.8: Top: kurtosis of different initial relative separations (r_0) as function of time. The dash-dotted line indicates the value of the kurtosis for a Gaussian distribution, i.e. $ku = 3$. Bottom: PDF of relative displacements for dimensionless time ($t = 2$). Shallow flow (EXP201).

pair separations to increase from one distance to the next, as explained in Section 2.2.2. Also the results obtained by means of the FSLE should agree with those obtained by means of the relative diffusivity. In the specific they also highlight the presence of two distinct stages of growth: at the smaller scales the value of λ_s^* typically attains an almost constant value, while, once larger scales are reached, it decreases following an approximate power law dependence with the distance. In figure 5.9 the values of the FSLEs have been reported for Shallow flow conditions. If the FSLEs attain a constant value over different separation scales, an exponential growth is implied. Indeed, the regime for separation smaller than the injection scale results in an exponential time growth of r^2 , leading to an almost constant value of the FSLEs. For scales larger than $r = r^*/L_{uL}^* > 1$ the FSLEs suggest another phase of growth, and their values decrease with an approximate power law close to $r^{-2/3}$ as for the Richardson regime. Finally, for larger separations, the decay

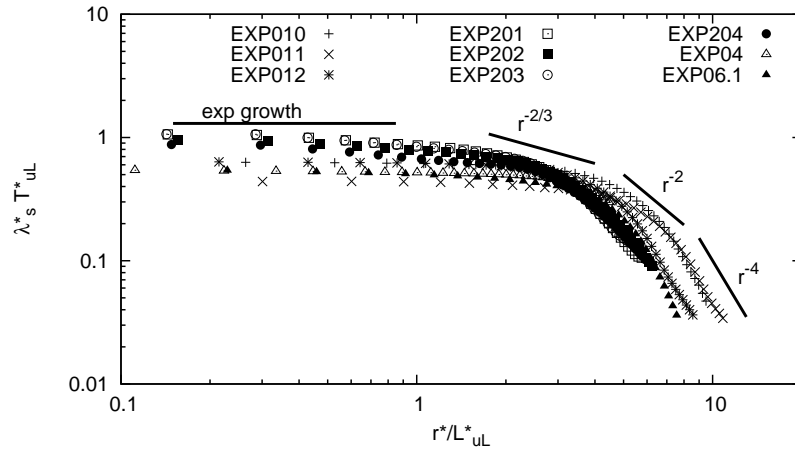


FIGURE 5.9: Finite Scale Lyapunov Exponents (FSLEs) for Shallow flow conditions

of λ_s follows a power law proportional to r^{-2} , suggesting the presence of an equilibrium regime (linear growth in the relative dispersion, i.e. the asymptotic regime characterized by standard diffusion, see LaCasce [2008] for more details). Moreover, for separations larger than the equilibrium regime, the decay of the FSLEs becomes steeper, corresponding to a growth in time of the separations with an exponent less than unity ($\gamma < 1$). The latter result indicating the existence of a subdiffusive regime, which implies that particles remain trapped by the large-scale flow structures and, as a consequence, the dispersive process is inhibited by them. In the present case, however, this happens at scales comparable with the width of the channel, which represent a constraint on the particle separations. Therefore, the observed diffusive regime is only controlled by the geometrical characteristics of the experimental flume.

5.2.2 Intermediate flows

Decreasing r_h and entering the Intermediate flow conditions, the dynamics of particle pairs is further complicated by the role of the Froude number. Intermediate flows behave quite differently with respect to Shallow flows although the influence of the macro-vortices is still evident because of the simultaneous presence of transitional vortices and floodplains vortices, as already discussed

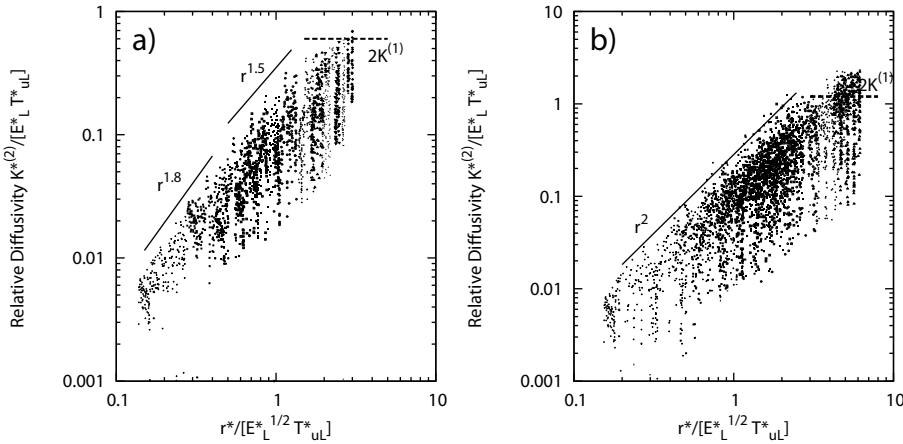


FIGURE 5.10: Relative diffusivity as a function of the dimensionless separation r for Intermediate conditions ($2 < r_h < 3$) in different regimes: a) subcritical flows, $Fr < 1$ (EXP205) and b) supercritical flows, $Fr > 1$ (EXP12).

in chapter 4.

To highlight the role of the Froude number, the behaviour of $K^{(2)}$ as function of the particle pair separation r is shown in figure 5.10, both for the subcritical regime ($Fr < 1$) and for the supercritical regime ($Fr > 1$). In the former case a strong similarity exists with the Shallow flows, characterized by two distinct growth regimes (direct enstrophy cascade for $r < L_i$ and inverse energy cascade for $L_i < r < 1$, with $L_i \sim 0.36$). However, as the Froude number exceeds the unity, our results indicate a change in the dynamics of the relative diffusivity with a single intermediate regime such that $K^{(2)} \propto r^2$, which is, usually, related to a non-local dynamics of particle pairs in the enstrophy inertial range associate with an energy spectrum of the kind $E(k) \propto k^{-3}$. Therefore, it seems that only for subcritical conditions an inverse-energy cascade survives (the injection scale always related to the flow depth jump as in the Shallow flows conditions), whereas only an enstrophy cascading process occurs for $Fr > 1$.

These behaviours are clearly evident by inspecting figure 5.11 where the results for the PSD functions are reported for the mentioned Intermediate flow conditions. In particular the subcritical case (panel a) is similar to that characterizing the Shallow flows (see figure 5.7), whereas the supercritical case (panel b) shows an enstrophy cascade. In the latter case it is reasonable to state that the flow is mainly dominated by the large-scale shear structure,

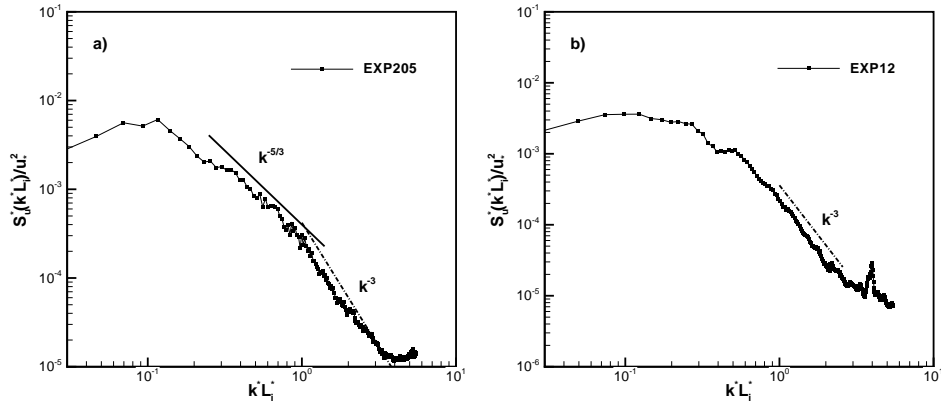


FIGURE 5.11: Normalized Eulerian Power Spectral Density function S_u corresponding to the Intermediate flow experiments of figure 5.10.

rather than by the transitional macro-vortices so that the dispersion is controlled by non-local processes.

A similar behaviour is observed in the PDFs for subcritical Intermediate flows, as shown in figure 5.12, where the inverse energy cascade is still the dominant process that controls the relative separation. Again, the smaller separations are well distinguished from the larger ones because the former are characterized by larger kurtosis, although in both cases ku attains almost constant values. However, if the flow regime is supercritical, the growth of the relative diffusivity $K^{(2)}$ follows one single power law (r^2) for any given initial value of the separations. The corresponding ku , after an initial decay stage lasting for $0 < t < 1.5$, rapidly tends to a constant value, approximately equal to 10, similar to that observed for the large separations in the subcritical flows.

Similarly to what done for the Shallow flow, we have analyzed the behaviour of the values of the FSLEs for different separations. In figure 5.13 the results obtained for the Intermediate flows for subcritical (panel a) and supercritical conditions (panel b) are reported. In the case of subcritical conditions, results similar to those shown for Shallow flows are recovered: for small separations it is possible to identify a first regime corresponding to an almost constant slope, while for larger separations a Richardson-like regime ($r^{-2/3}$) and an equilibrium regime (r^{-2}) are found. For supercritical flow conditions, when an enstrophy cascade sets in and $K^{(2)}$ follows a single trend proportional to r^2 (which implies an exponential growth in time of r^2) the plateau of λ_s extends

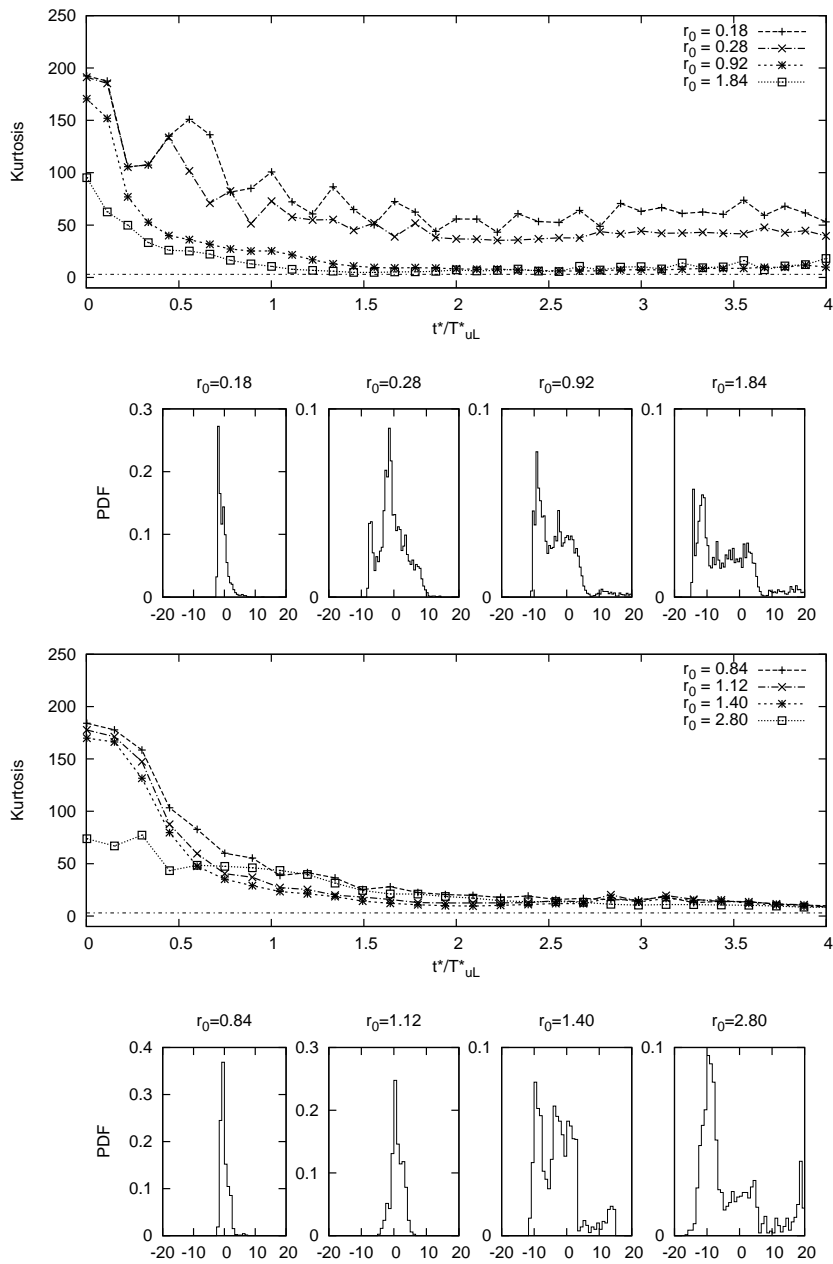


FIGURE 5.12: Subcritical (case EXP205) and supercritical (case EXP12) Intermediate flows. First (subcritical flow) and third (supercritical flow) panels: kurtosis of different initial relative separations (r_0) as function of time. The dash-dotted line indicates the value of the kurtosis for a Gaussian distribution, i.e. $ku = 3$. Second (subcritical flow) and fourth (supercritical flow) panels: PDFs of relative displacements for dimensionless time ($t = 2$).

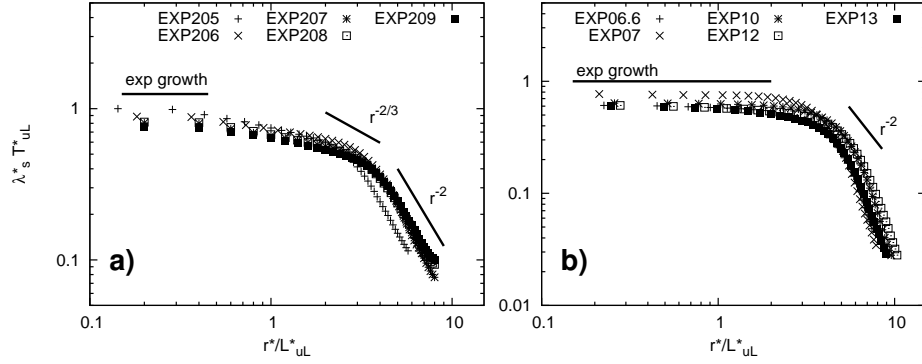


FIGURE 5.13: Finite Scale Lyapunov Exponents (FSLEs) for Intermediate flow conditions. a) Subcritical flow ($Fr < 1$); b) Supercritical flow $Fr > 1$.

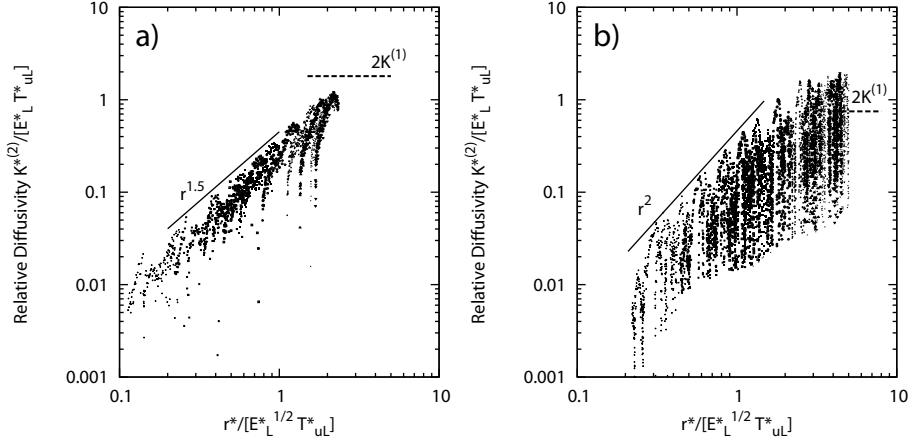


FIGURE 5.14: Relative diffusivity as a function of the dimensionless separation r for Deep conditions ($r_h < 2$) in different regimes. Panel a) subcritical flows ($Fr < 1$) EXP112; panel b) supercritical flows ($Fr > 1$) EXP17.

up to $r \simeq 2$. For larger separations an equilibrium is, again, reached. Also in this case a subdiffusive regime is visible for separations larger than $r > 5$.

5.2.3 Deep flows

The relative diffusivity always follows one single growth power law which, however, depends on the flow regime, i.e. $K^{(2)} \propto r^{1.5}$ in the subcritical regime and $K^{(2)} \propto r^2$ in the supercritical one, see figure 5.14. Even in this case, the equilibrium phase is not easily detectable from $K^{(2)}$. A single growth regime is also evident from the FSLEs, see figure 5.15. Indeed, the exponen-

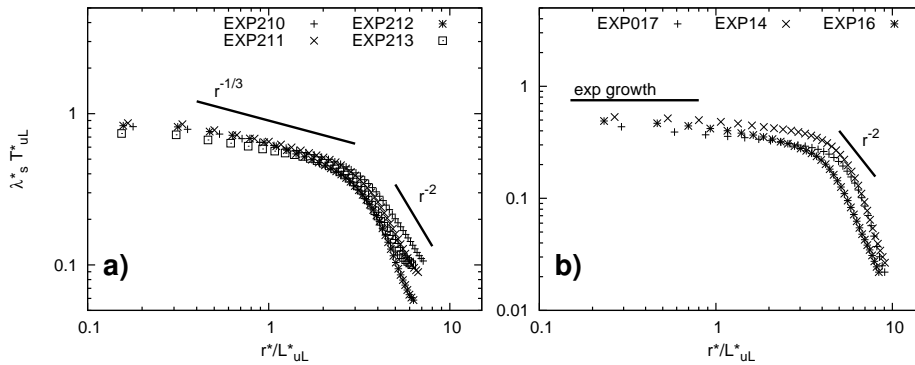


FIGURE 5.15: Finite Scale Lyapunov Exponents (FSLEs) for Deep flow conditions. a) Subcritical flow ($Fr < 1$); b) Supercritical flow $Fr > 1$.

tial growth is almost absent in case of subcritical flows, where a single trend proportional to $r^{-1/3}$ covers separations up to about 3, before changing to a clear equilibrium slope (r^{-2}). On the contrary, supercritical flows are characterized by a long exponential growth, related to $K^{(2)} \propto r^2$, again followed by a diffusive regime.

An explanation for the behaviour of the Deep flows is based on the observation that the topographic forcing only weakly affects such a flow, since $r_h \rightarrow 1$ and, as a consequence, no transitional vortices are observed. The results suggest that for subcritical flows the energy transfer occurs through a direct energy cascading (see figure 5.16a) where for the PSD an exponent -2 is recovered (close to the value of $-5/3$ typical of a Richardson regime), whereas in the supercritical regime a direct enstrophy cascade dominates the dynamics (see figure 5.16b).

The present results are in good agreement with the findings of Nikora et al. [2007], who investigated the influence of large-scale flow structures on the energy processes characterizing free-surface uniform flows, in a case of rectangular cross-section. The analysis of the surface velocity measurements presented in Nikora et al. [2007] suggests that for $Fr > 1$ the energy spectrum follows a power law with an exponent -3 (enstrophy cascade) while, for subcritical conditions ($Fr < 1$), a direct energy cascade was observed. Note that the same exponent of the Richardson regime can be recovered also in the case of shear dispersion.

For the present case, shear dispersion is likely to occur in the case of Deep

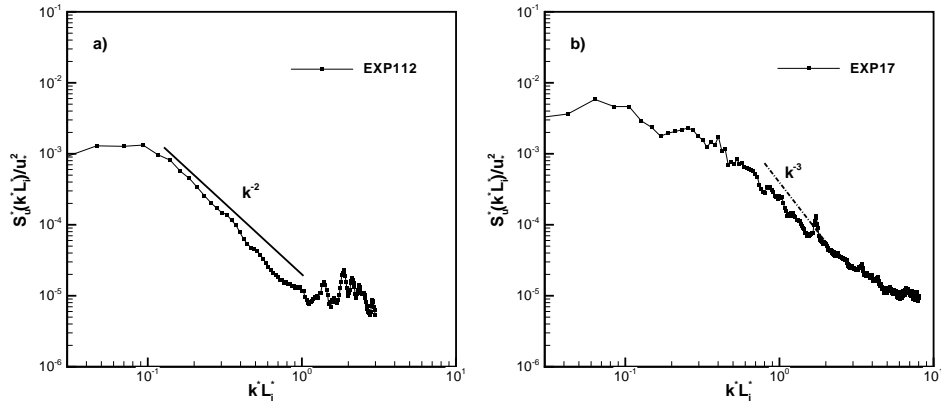


FIGURE 5.16: Normalized Eulerian Power Spectral Density function S_u corresponding to Deep flows experiments of figure 5.14.

flows. A way to distinguish the Richardson dispersion from shear dispersion is to investigate the PDFs of the separations, since in the case of shear dispersion PDFs of separation should be Gaussian [LaCasce, 2008]. Subcritical Deep flows are characterized by a Richardson-like exponent, however, the time dependence of the kurtosis, after an initial decay stage for $0 < t < 1.5$, attains an almost constant value close to pure Gaussian distributions ($ku = 3$), suggesting that in these conditions a shear dispersion takes place [Bennett, 1987] (see the top two panels of figure 5.17).

Finally, in supercritical flows the results are in agreement with those found for the supercritical Intermediate flows, i.e. ku decays from its initial value to a constant value approximately equal to 10 (see the bottom two panels of figure 5.17).

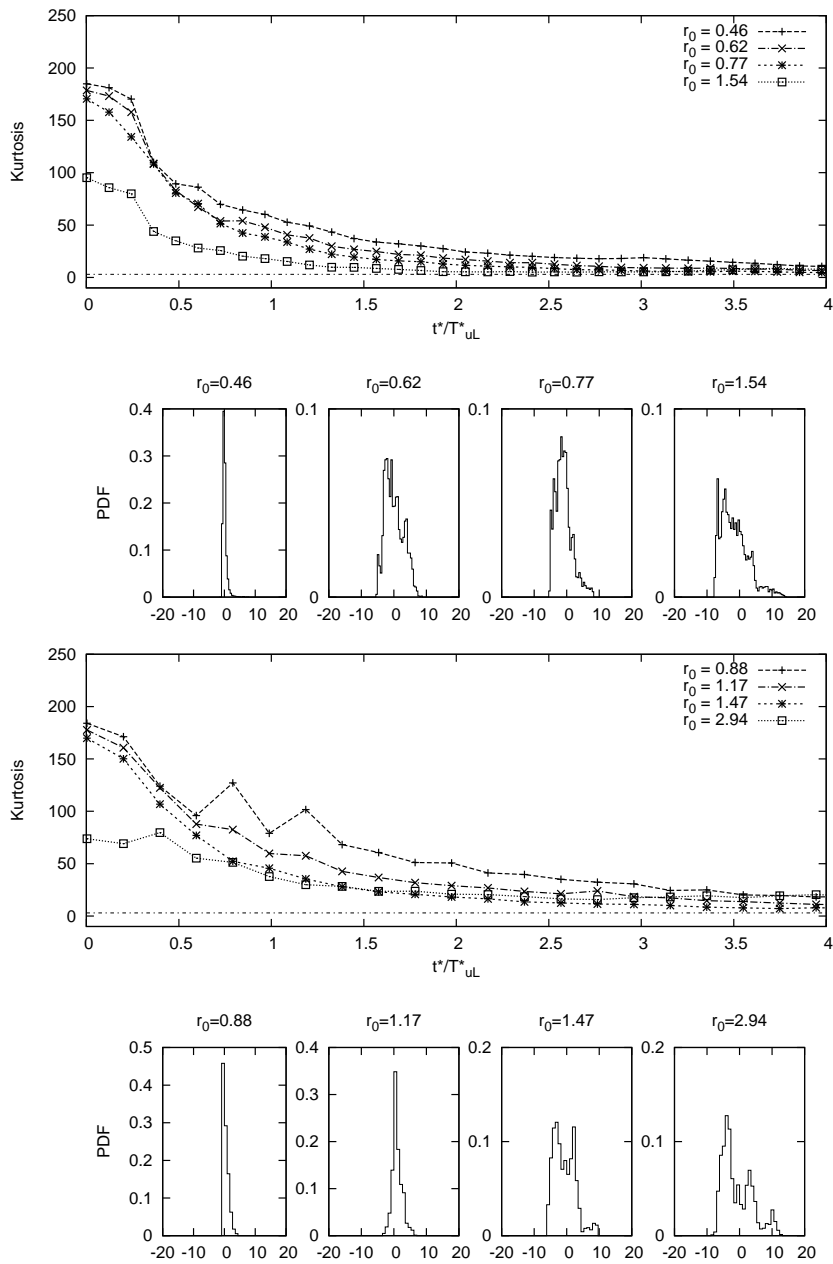


FIGURE 5.17: Subcritical (case EXP213) and supercritical (case EXP17) Deep flows. First (subcritical flow) and third (supercritical flow) panels: kurtosis of different initial relative separations (r_0) as function of time. The dash-dotted line indicates the value of the kurtosis for a Gaussian distribution, i.e. $ku = 3$. Second (subcritical flow) and fourth (supercritical flow) panels: PDFs of relative displacements for dimensionless time ($t = 2$).

Chapter 6

Mixing characteristics

The main objective of this section is the computation of the diffusivity coefficients for compound channel flows and the comparison of the present data with previous contributions.

To this end, a different scaling is preferable because it is the most commonly used in this field of research. In particular, the diffusivity coefficients can be made dimensionless choosing a typical length scale and a typical velocity scale, representative of the intensity of the turbulent flow. The hydraulic radius R^* has been chosen as the relevant length scale and the bottom shear velocity u_S^* as the velocity scale: unless the channel can be assumed as infinitely wide, the hydraulic radius is a more correct length scale than the flow depth hence u_S^* reads

$$u_S^* = \sqrt{g i_f R^*}, \quad (6.1)$$

where i_f is the bottom slope.

6.1 Previous laboratory experiments and state of the art

Calculations of pollutant concentration in water bodies (e.g. rivers, reservoirs, estuaries and oceans) are based on the solution of the advection-diffusion

equation which in its three-dimensional form reads:

$$\begin{aligned} \frac{\partial C^*}{\partial t^*} + u^* \frac{\partial C^*}{\partial x^*} + v^* \frac{\partial C^*}{\partial y^*} + w^* \frac{\partial C^*}{\partial z^*} = \frac{\partial}{\partial x^*} \left(D_x^{*T} \frac{\partial C^*}{\partial x^*} \right) + \\ + \frac{\partial}{\partial y^*} \left(D_y^{*T} \frac{\partial C^*}{\partial y^*} \right) + \frac{\partial}{\partial z^*} \left(D_z^{*T} \frac{\partial C^*}{\partial z^*} \right), \end{aligned} \quad (6.2)$$

where $\mathbf{u}^* = (u^*, v^*, w^*)$ is the Eulerian three-dimensional vector field, D_x^{*T} , D_y^{*T} and D_z^{*T} are the turbulent diffusion coefficients [see Taylor, 1921].

However, in most applications a simplified version of equation (6.2) is employed. In particular, whenever the shallow-water approximation holds, 2D or 1D advection-diffusion equations can be derived by integrating (6.2) along the vertical and the transversal direction, respectively.

For depth-integrated computations, streamwise and spanwise mass fluxes can be written, on the basis of a Fickian approach, in terms of the product of the gradients of the mean concentration times the following coefficients:

$$K_x^* + \overline{D_x^{*T}} \quad \text{and} \quad K_y^* + \overline{D_y^{*T}}, \quad (6.3)$$

where K_x^* and K_y^* respectively account for the dispersion effects due to the non-uniformity of the vertical profile of the longitudinal and transversal velocity, whereas $\overline{D_x^{*T}}$ and $\overline{D_y^{*T}}$ are the vertically-averaged turbulent diffusion coefficients.

By further integrating along the transversal direction a 1D advection-diffusion equation is obtained, in which the longitudinal mass flux is the product between the streamwise gradient of the area-averaged concentration and the following coefficient:

$$K_L^* + \overline{K_x^*} + \overline{\overline{D_x^{*T}}}, \quad (6.4)$$

where $\overline{K_x^*}$ is the dispersion coefficient due to the vertical flow/concentration disuniformity, $\overline{\overline{D_x^{*T}}}$ is the area-averaged turbulent diffusion coefficient and K_L^* accounts for the longitudinal dispersive effects.

The accuracy of the solution of equation (6.2) and of its simplified versions strongly depends on the chosen diffusivity and dispersive coefficients. For this reason major efforts have been devoted to the estimation of such coefficients; in the following we briefly recall the most relevant results, some of which are

compared with our findings.

6.1.1 Transverse mixing coefficient

The value of the transverse dispersion coefficient is often assumed to be a function of the bottom shear velocity and of the mean water depth as:

$$K_y^* + \overline{D_y^{*T}} = Au_s^* h^*, \quad (6.5)$$

where A is a factor depending on the width-to-depth ratio and on the bottom friction factor.

If, on the one hand, it is possible to directly measure the turbulent diffusivity $\overline{D_y^{*T}}$ separately from the dispersive term K_y^* , by limiting the effects of secondary flows, on the other hand, whenever secondary flows play a relevant role, it is impossible to separate the two contributions.

In order to evaluate $\overline{D_y^{*T}}$, Elder [1959] performed an experimental investigation on a uniform open-channel flow in a flume characterized by a rectangular section. In particular he measured the depth-integrated concentration distribution of a tracer and by comparison with an analytical solution he was able to estimate a constant A of about 0.17. With a similar experimental set-up Okoye [1970] found $0.1 \leq A \leq 0.2$.

However, natural river flows very often differ from those evolving in rectangular channels. Because of this, several experiments have been performed to investigate the effects of: 1) cross-section variation, 2) sidewall irregularities and 3) channel curvature. In the present context, we restricted our attention to the results obtained for straight channels, that represent the closest configuration to the one employed in the present study, disregarding any curvature effects.

Holley and Abraham [1973] studied how transverse mixing in a straight rectangular flume of constant depth was influenced by the presence of lateral groins. The authors found that $0.16 \leq A \leq 0.4$, thus concluding that secondary flows induced by groins strongly enhance lateral mixing. In a similar set of experiments, Lau and Krishnappan [1977] investigated the variation of the transverse dispersion coefficient depending on different values

of the friction factor and width-to-depth ratio, obtaining values of about $0.15 \leq A \leq 0.25$.

Moreover, Webel and Schatzmann [1984] described an experimental study, performed in a 20m-long rectangular flume, and the dependence of the mixing coefficient on different properties of the channel flow (Reynolds number, Froude number, width-to-depth ratio and roughness), finding $0.13 \leq A \leq 0.24$. Moreover, a residual dependence on the friction coefficient remains when the flow evolves in smooth conditions.

Rutherford [1994] in his book collected results from many studies resulting in an extended range for the transversal mixing coefficient equal to $0.1 - 0.15 < A < 0.3 - 0.4$.

More recently, Chau [2000] proposed data on transverse mixing in an open, rectangular channel under different flow and bottom roughness conditions and, in agreement with previous works, found $0.13 \leq A \leq 0.14$.

The first attempt to analyze dispersion and diffusion processes due to composite sections, such as those of compound channels, has been made by Arnold et al. [1989] who evaluated mixing coefficients using either a modified version of the generalized change of moment analysis or a variational method in conjunction with a finite element dispersion model. The results suggest a mean value $A = 0.45$. Wood and Liang [1989] employed the measures performed for a rectangular channel by Nokes and Wood [1988] to compare an eigenvalue-eigenfunction solution for the dispersion of effluent in a compound-like channel with some experimental data of solute dispersion performed by Wood and Liang [1989] themselves. The results of the analytical model revealed that values of the lateral diffusivity for rectangular channels were not in agreement with the experimental data. The same kind of approach has been followed by Spence et al. [1997] and Spence et al. [1998] who found $A \sim 0.32$. A similar value has been obtained by an experimental campaign by Fraselle et al. [2008], who suggested a mean value (for the main channel and the floodplains) $A = 0.21$. Zeng et al. [2008], using the generalized method of moments, and on the basis of data collected in a symmetric trapezoidal compound channel found $A \sim 0.26$. Guymer and Spence [2009] proposed a distribution of local transverse mixing coefficient with peak mixing occurring at the start of the floodplain.

All the above mentioned works do not analyze the influence on the transverse mixing coefficient due to flow characteristics such as the flow depth ratio and the Froude number.

6.1.2 Longitudinal mixing coefficient

The longitudinal dispersion coefficient K_x^* was first introduced by Taylor [1921] as a measure of the dispersion process described by the advection-dispersion equation. Elder [1959] extended Taylor's theory for the dispersion in pipe flows to an open channel of infinite width and he derived an analytical solution for the longitudinal dispersion coefficient. Elder's theory assumes: 1) a logarithmic vertical profile for the longitudinal velocity and 2) that the turbulent transport coefficient of momentum and mass are identical. Eventually, Elder [1959] derived the following relationships:

$$K_x^* = 5.93u_S^*h^* \quad (6.6)$$

$$\overline{D_x^{*T}} \sim (2 \div 3)D_z^{*T} = (2 \div 3)0.067u_S^*h^*, \quad (6.7)$$

in which h^* is the water depth averaged in the transversal direction.

Once the 1D advection-diffusion equation is derived for the longitudinal direction (i.e. averaging over the depth and width), the mixing coefficient to be determined becomes the sum of three different contributions, see eq. (6.4), where K_L^* is the longitudinal dispersion coefficient, which arises from the average along the transversal direction of the convective terms.

It is, usually, assumed that $K_L^* \gg \overline{K_x^*}, \overline{D_x^{*T}}$, since it is observed that longitudinal dispersion dominates longitudinal mixing due to non-uniformity of the vertical velocity profile and other geometrical non-uniformities (dead zones, curves, non-uniform depth, etc.).

Most of the estimates of K_L^* for natural streams have been of empirical nature. By qualitative means Fischer [1975] obtained an approximated formula for the dimensionless dispersion coefficient $K_L^*/h^*u_S^*$,

$$\frac{K_L^*}{h^*u_S^*} = 0.011 \left(\frac{U^*}{u_S^*} \right)^2 \left(\frac{B^*}{h^*} \right)^2, \quad (6.8)$$

where U^* is the cross-sectional mean velocity and B^* is the width of the channel. The general form of dimensionless longitudinal dispersion coefficients proposed in the literature is

$$\frac{K_L^*}{h^* u_S^*} = \alpha \left(\frac{U^*}{u_S^*} \right)^\beta \left(\frac{B^*}{h^*} \right)^\gamma, \quad (6.9)$$

where α , β and γ are non-integer constants.

In particular, Seo and Cheong [1998] analyzed previous empirical equations and derived the following values of the coefficients $\alpha = 5.915$, $\beta = 0.620$ and $\gamma = 1.428$. Finally Deng et al. [2001], taking into account the irregularity of natural rivers and directly integrating the Fischer's triple integral, developed the following relationship for the longitudinal dispersion coefficient:

$$\frac{K_L^*}{h^* u_S^*} = \frac{0.15}{8\epsilon_{t0}} \left(\frac{U^*}{u_S^*} \right)^2 \left(\frac{B^*}{h^*} \right)^{5/3}, \quad (6.10)$$

where $\epsilon_{t0} = 0.145 + (1/3520) (U^*/u_S^*) (B^*/h^*)^{1.38}$.

For natural open channels, the strong non-uniformity of the velocity profile between the two banks may lead to values of $K_L^*/h^* u_S^*$ that range from 5 to 7000 [Fischer et al., 1979].

6.2 Transverse and Longitudinal Diffusivity

In most of the experimental works discussed in the previous section the transverse mixing coefficient has been evaluated using the so-called method of moments. In particular, such a method assumes that the advection-diffusion equation for a uniform, straight-channel flow due to a continuous point-source release of contaminant has a gaussian-type solution for the concentration. The moments of the latter distribution, e.g. the variance, are then fitted against the concentration measurements. From the time of spatial evolution of the variance the transverse dispersive coefficient is, eventually, evaluated.

In the present analysis, we have used a more direct approach based on the theoretical background discussed in Chapter 2.

Based on the discussion of section 5.1 and operating the mentioned mean flow

removal, we are able to evaluate an equivalent transversal mixing coefficient which takes into account the effects of the turbulent diffusion and dispersion, as usually reported in the literature [see a.o. Rutherford, 1994, and references therein]

$$K_y^{*(1)} \equiv K_y^* + \overline{D_y^{*T}} = (\text{from eq. 6.5}) = Au_S^* h^* \quad . \quad (6.11)$$

Two major mechanisms generally influence the longitudinal dispersion: (i) turbulent velocity fluctuations; (ii) lateral and vertical variation of the velocity in the cross-section. Because of the experimental approach (PIV measures of surface velocity) and because of the mentioned mean flow removal from the Eulerian velocity fields, we are able to provide an estimate of the turbulent diffusion term $\overline{D_x^{*T}}$ only, which is, usually, much smaller than the dispersion coefficient K_L^* . Hence the longitudinal absolute diffusivity evaluated by means of equation (2.19) corresponds to the turbulent diffusion:

$$K_x^{*(1)} \equiv \overline{D_x^{*T}} \quad . \quad (6.12)$$

Moreover, as discussed in Stocchino et al. [2011] and in chapter 5, the approach used to numerically calculate the particle trajectories starting from measured Eulerian fields and, therefore, to evaluate absolute dispersion, suffers of small-amplitude, high-frequency oscillations that, ultimately, generate a noisy time distribution of the absolute diffusivities, which is the time derivative of a^{*2} . In the present context, where the aim is to quantify the values of the diffusivity coefficients and their dependence on the main physical parameter, it has become crucial to eliminate the spurious oscillations before computing $K_x^{*(1)}$ and $K_y^{*(1)}$.

In particular, we have tested two methods. With the first approach, we have filtered the absolute dispersion distribution and, then, we have computed the time derivative of the filtered signal and the diffusivity coefficient is eventually evaluated where its value is constant (i.e. for longer times). We have used two different filters in our procedure. In particular, the Savitzky-Golay filter, which is a generalized moving average with filter coefficients determined by an unweighted linear least-squares regression and a polynomial model of

specified degree. The other filter is a local regression based on weighted linear least squares and a 2^{nd} degree polynomial model, where lower weight is assigned to outliers in the regression. The method assigns zero weight to data outside six mean absolute deviations. Alternatively, we have sought for the best linear regression of the filtered data, using a least square method, of the absolute dispersion in a time range where this is meaningful, i.e. where a Brownian regime is expected.

The resulting linear coefficient is directly a measure of the diffusivity coefficients. The coefficients computed with both methods resulted to be very similar, however, after several tests, the second approach proved to be more robust and it was used to produce the results that we discuss in the following. As already described in chapter 2 and chapter 5, once the asymptotic trend of the absolute dispersion $a^2(t)$ is reached, the corresponding absolute diffusivity $K^{(1)}$ can be obtained by directly differentiating in time $a^2(t)$ and, not surprisingly, this shows a rather irregular time dependence, with large fluctuations, caused by the high-frequency oscillation discussed in the previous section.

Results obtained for single-particle statistics (absolute dispersion and absolute diffusivities) are reported as functions of time in figures 6.1, 6.2 and 6.3, for shallow and deep flow conditions. As described in the previous chapters, the dimensionless absolute dispersion a^2 displays, for both shallow and deep flow conditions, an initial ballistic regime with a quadratic growth in time (a^2 proportional to the dimensionless time t^2 where $t = t^*/T_L^*$). In figures 6.1, 6.2 and 6.3, the grey horizontal lines represent the linear regressions for filtered data obtained for times larger than T_L^* . Such a behaviour has been observed for the whole set of experiments.

A summary of the results obtained for the asymptotic values of the dimensionless absolute diffusivity coefficients for large times is reported in table 6.1. All quantities have been made dimensionless using the hydraulic radius R^* and the bottom shear velocity u_S^* of the uniform flow. Though these parameters may vary in a non-monotone way with the flow depth in compound channels, they represent the most suited pair of variables to produce dimensionless quantities comparable throughout all geometric and flow conditions.

As already stated the main physical parameters that control the dynamics

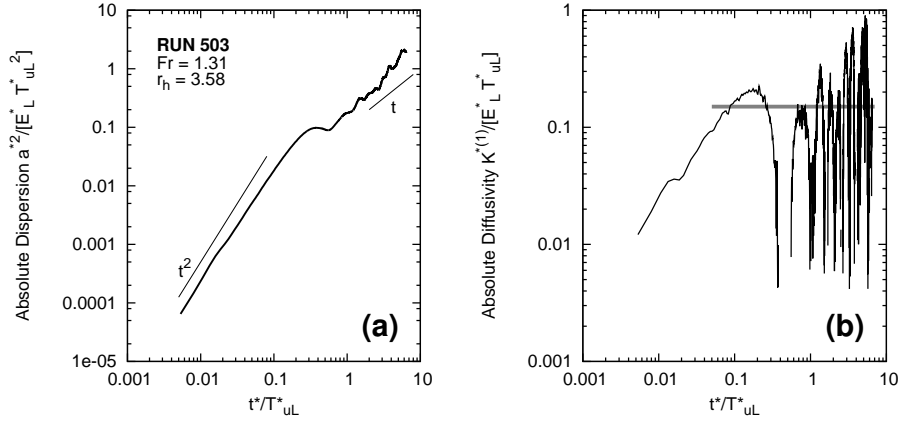


FIGURE 6.1: Single-particle statistics for experiment 503, shallow-flow conditions. Absolute dispersion and absolute diffusivity, panel (a) and panel (b) respectively.

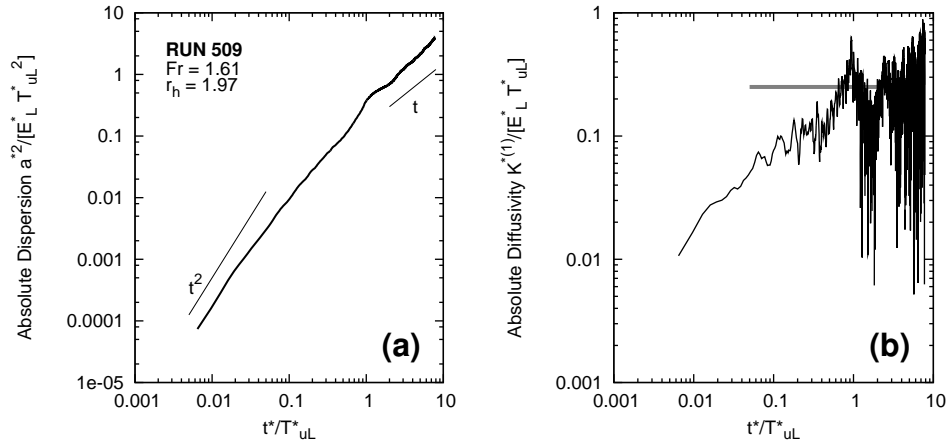


FIGURE 6.2: Single-particle statistics for experiment 509, deep-flow conditions. Absolute dispersion and absolute diffusivity, panel (a) and panel (b) respectively.

TABLE 6.1: Experimental measurements of absolute diffusivity coefficients

Flow	r_h (-)	Fr (-)	$K_x^{*(1)}/u_S^* R^*$	$K_y^{*(1)}/u_S^* R^*$
Shallow	3.01-4.42	0.63-1.94	0.035-0.441	0.060-0.481
Intermediate	2.02-2.92	0.72-1.72	0.013-0.473	0.021-0.341
Deep	1.68-1.97	0.73-2.16	0.014-0.094	0.020-0.230

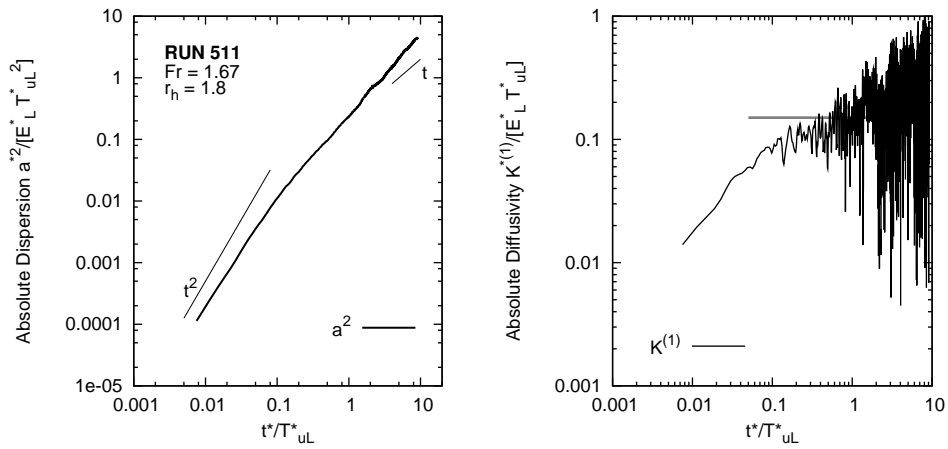


FIGURE 6.3: Single particle statistics for experiment 511, deep-flow conditions. Absolute dispersion, panel (a) and absolute diffusivity, panel (b).

of a uniform flow in a compound channel and, consequently, the Lagrangian mixing processes, are the flow-depth ratio r_h and the Froude number Fr , which discriminates the flow regimes between sub and supercritical. For this reason, the absolute diffusivity coefficients have been analyzed in terms of their dependence on r_h and Fr . In the following we show the results for the dimensionless absolute diffusivity components in the x - and y -directions, $K_x^{(1)} = K_x^{*(1)}/R^*u_S^*$ and $K_y^{(1)} = K_y^{*(1)}/R^*u_S^*$, respectively.

6.2.1 Zonal diffusivities for main channel and floodplains

Results are proposed for the dependence of longitudinal and transversal zonal diffusivities on both the relative flow depth (r_h) and flow intensity (Fr). Zonal diffusivities have been computed by a region-specific analysis that consists in seeding and tracking particles either in the main channel or on the floodplains. An attempt is also made to compare these results with available literature results for the dependence of $K_x^{(1)}$ with the flow intensity [Manson and Wallis, 2004].

Figures 6.4 and 6.5 show that the dependence of both $K_x^{(1)}$ and $K_y^{(1)}$ on r_h is robust, in the sense that both zonal diffusivities (top panels, those derived

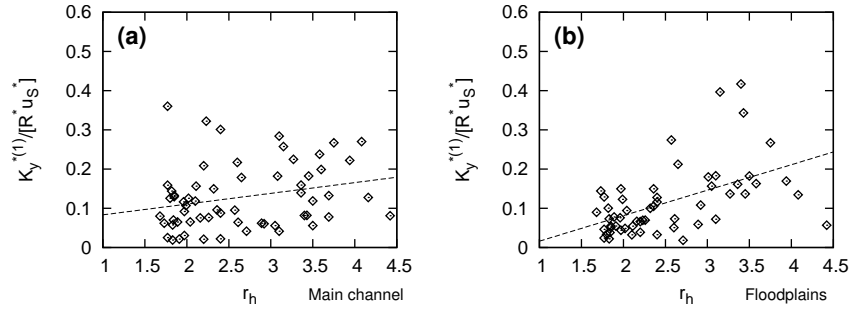


FIGURE 6.4: Dependence of the dimensionless absolute diffusivity $K_y^{*(1)}/u_S^* R^*$ on r_h for data collected in the main channel, (a) and floodplains (b). Lines indicate linear regression of the data.

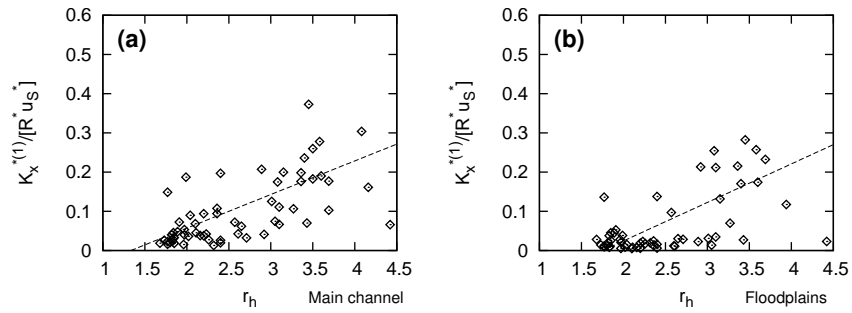


FIGURE 6.5: Dependence of the dimensionless absolute diffusivity $K_x^{*(1)}/u_S^* R^*$ on r_h for data collected in the main channel (a) and floodplains (b). Lines indicate linear regression of the data.

for the main channel flow and bottom panels those for the floodplain flows) monotonically increase with the shallowness parameter r_h and with comparable growth velocities in the main channel and floodplains for $K_x^{(1)}$ (figure 6.5) and a faster growth in the floodplains of $K_y^{(1)}$ (essentially due to the shallow flows, figure 6.4).

This is not true when considering the dependence on the flow intensity, here described by Fr (see figures 6.6 and 6.7). In fact, while the main-channel zonal $K_y^{(1)}$ is directly proportional to Fr (see top panel of figure 6.6), an inverse proportionality characterizes the dependence of the floodplain zonal $K_y^{(1)}$ on Fr (see bottom panel of figure 6.6). Similarly, the floodplain zonal longitudinal diffusivity, $K_x^{(1)}$, is almost independent from Fr (see the bottom panel of figure 6.7). Although these results may be interpreted in similarity with those of Manson and Wallis [2004], who find an inverse proportionality

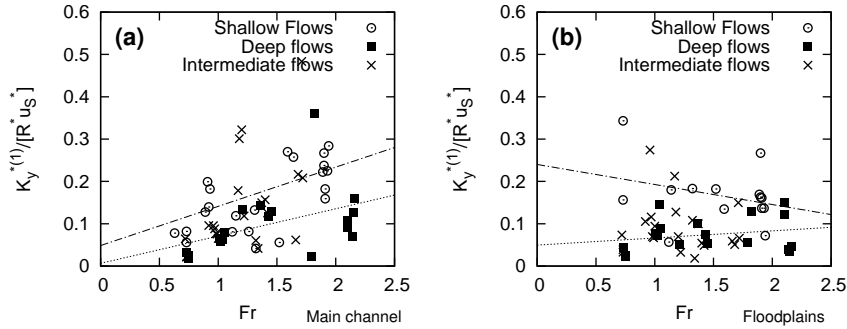


FIGURE 6.6: Dependence of the dimensionless absolute diffusivity $K_y^{*(1)}/u_S^* R^*$ on Fr for data collected in the main channel (a) and floodplains (b). Lines indicate linear regression of the data.

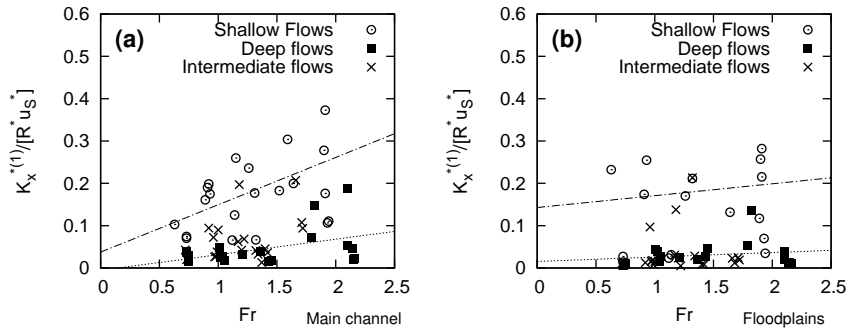


FIGURE 6.7: Dependence of the dimensionless absolute diffusivity $K_x^{*(1)}/u_S^* R^*$ on Fr for data collected in the main channel (a) and floodplains (b). Lines indicate linear regression of the data.

of the longitudinal diffusivity with the flow rate for floods that give rise to overbank flows, care must be used because all the present results pertain to overbank flows with diffusivities computed by the mentioned zonal analysis. Zonal sowing and tracking of tracers may also give rise to problems in characterizing the role of large-scale eddies that span over the transition region i.e. extend from the main channel to the floodplains. In this case it is virtually impossible to remove the influence of such coherent structures on the zonal diffusivities, hence leading to uncertainties in the values of the computed diffusivities.

Because of this type of problems and due to the wish of providing values of diffusivities to be used for practical modeling purposes, i.e. valid over the entire flow cross section, we have focused our attention of global values

of diffusivities, obtained seeding the flow over the whole compound channel cross-section (i.e. main channel and floodplains).

6.2.2 Global diffusivities for the whole channel

Figures 6.8 and 6.9 respectively illustrate the distributions of globally-computed (i.e. over the entire cross section) diffusivities $K_x^{(1)}$ and $K_y^{(1)}$ in the $(r_h; Fr)$ -parameter space. Despite a relatively large residual scatter in the estimated values, which derives from the fitting procedure described in section 6.2, the results suggest that in the $(r_h; Fr)$ -plane, $K_x^{(1)}$ and $K_y^{(1)}$ increase with both the flow depth ratio, i.e. for shallower flows, and the Froude number, i.e. for supercritical flows. The range of the experimental parameters covers a rather large interval: the Froude number spans from 0.6 to 2.2 and r_h from about 1.1 to 4.4.

In figure 6.10 the values of $K_y^{(1)}$ have been reported as function of the flow depth ratio r_h and of the Froude number Fr separately, in panels (a) and (b), respectively. The dimensionless transversal absolute diffusivity seems to monotonically increase with r_h from the deep flows towards the shallow flows, regardless of the values of the Froude number, see figure 6.10 panel (a). Despite a significant scatter of the measurements, due to the superposition of errors generated at each step (data collection, data analysis, etc.) of the complex procedure employed to estimate the mixing coefficients, an almost linear dependence on r_h can be observed. Comparably large scatter in the data is always found in similar studies [see Rutherford, 1994, and reference therein]. The highest values of $K_y^{(1)}$ are found for the shallow-flow conditions. However, if we analyze the results as function of the Froude number Fr , see figure 6.10 panel (b), the distinction between the two limiting cases (deep and shallow flows) appears more clearly. In fact, despite an increase of $K_y^{(1)}$ with Fr , two distinct trends can be easily recognized depending on the values of r_h , revealing that shallow flows (hollow markers) lead to greater values of $K_y^{(1)}$ than deep flows (solid markers). Results for the intermediate flows nicely accommodate between the deep and shallow flow cases (cross markers).

Analogous results for the streamwise coefficients $K_x^{(1)}$ are shown in figure 6.11, panels (a) and (b), respectively. A behavior similar to that observed for

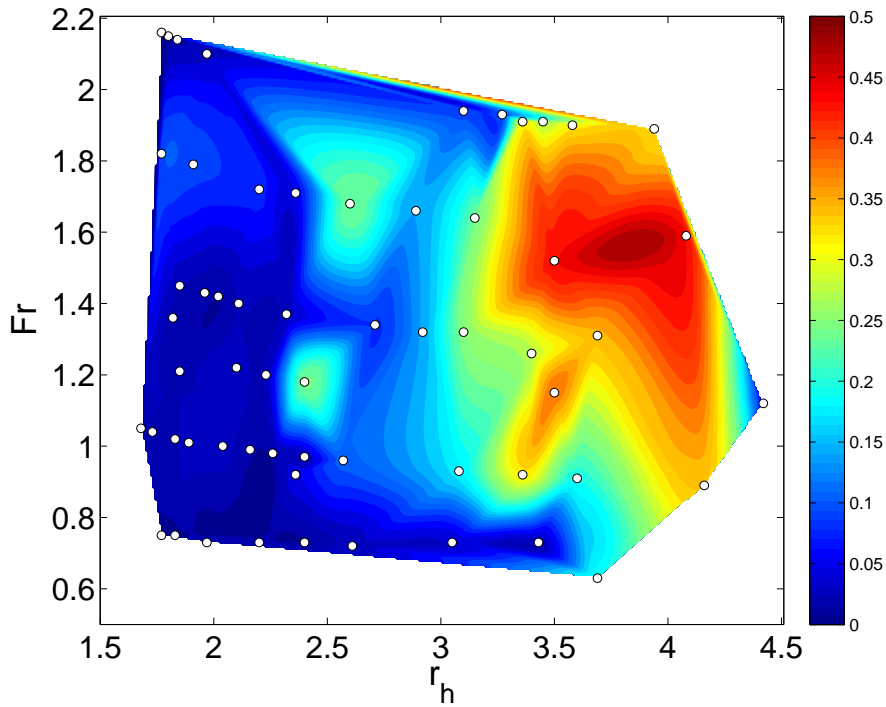


FIGURE 6.8: Distribution of the dimensionless absolute diffusivity $K_x^{*(1)}/u_S^* R^*$ in the $(r_h; Fr)$ -parameter space.

the transverse coefficient is recovered: the longitudinal turbulent diffusivity monotonically increases with the flow-depth ratio r_h , panel (a), and shallow and deep flows are remarkably different for the same flow conditions in terms of Froude number, panel (b).

Moreover, the longitudinal turbulent mixing is, not surprisingly, much less intense for the deep-flow conditions compared with the shallow cases. In fact, as described in section 6.1, $K_x^{(1)}$ only accounts for the turbulent fluctuations disregarding dispersive effects. For this reason the velocity fluctuations are less intense for the deep flows, where the two-dimensional free surface velocity fields are more uniform than for the shallow flow conditions, see chapter 4. In the present analysis, we have consistently observed that both the longitudinal and the transversal mixing coefficients increase with the flow-depth ratio. This can be explained, on the basis of the aforementioned flow characteristics, with the increase of the macro-vortices content as the flow becomes

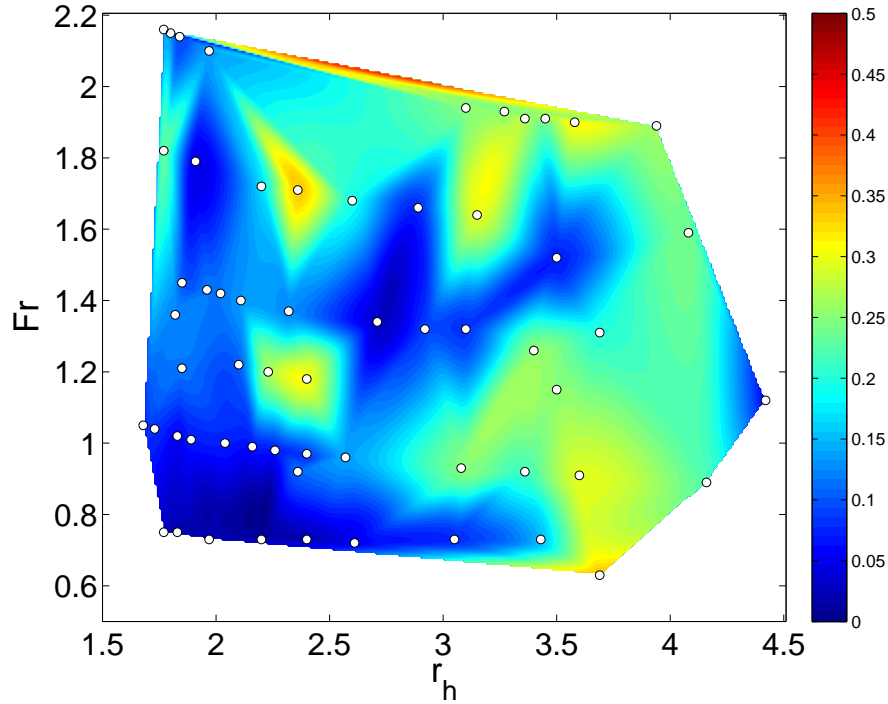


FIGURE 6.9: Distribution of the dimensionless absolute diffusivity $K_y^{*(1)}/u_S^* R^*$ in the $(r_h; Fr)$ -parameter space.

shallower, see figures 6.10 and 6.11. The action of the macro-vortices, that in some cases also are modified by merging processes, results in an increase of the mass transport coefficients in both directions. Moreover, the longitudinal coefficient $K_x^{(1)}$ displays a more pronounced difference from deep to shallow flows, see figure 6.11. In this case, the regularity of the free-surface velocity fields, which leads to flatter spanwise profiles of the mean streamwise velocity (see figure 4.2), results in a low intensity of the turbulent fluctuations and, thus, in a smaller $K_x^{(1)}$.

More information can be gained by plotting the ratio between the longitudinal and transversal coefficients ($K_x^{(1)}/K_y^{(1)}$) as function of r_h (see figure 6.12). The shaded area indicates the region of intermediate flows. The figure shows that deep flows, regardless the sub- super-critical regime, are characterized by a longitudinal turbulent diffusion always smaller than its transversal counterpart. On increasing r_h we find the range of intermediate flows ($2 < r_h < 2.5$)

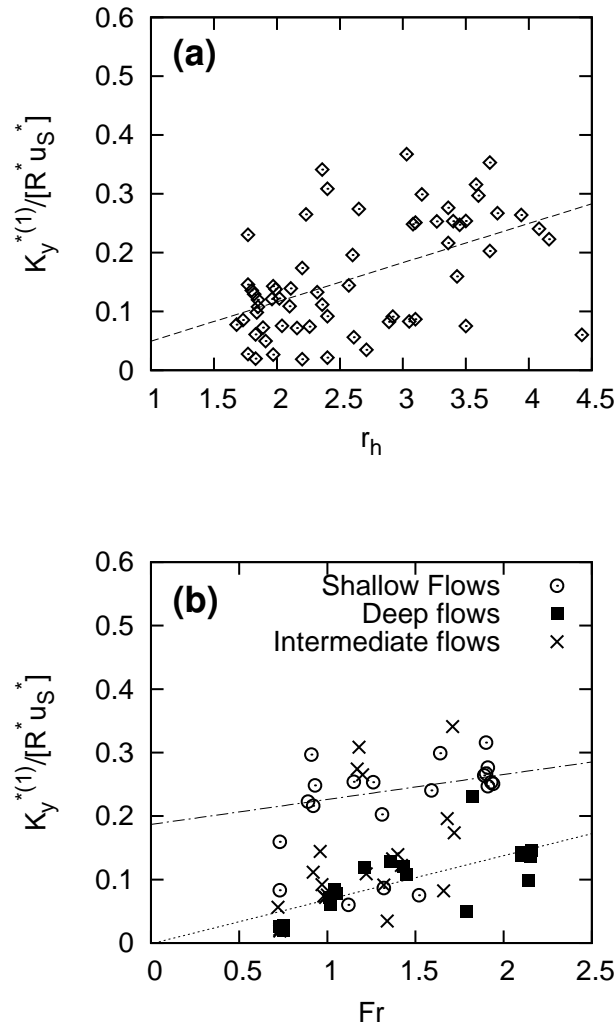


FIGURE 6.10: Dependence of the dimensionless absolute diffusivity $K_y^{*(1)}/u_S^* R^*$ on r_h (a) and Fr (b). Lines indicate linear regression of the data.

in which $K_x^{(1)}/K_y^{(1)}$ displays a behavior similar to that characterizing the deep flows. However, moving towards shallower conditions ($2.5 < r_h < 3$) a different behavior, depending on the Froude number is observed. In fact, subcritical flows statistically lead to higher transversal coefficients, whereas for $Fr > 1$ the opposite occurs, i.e. $K_x^{(1)}/K_y^{(1)} > 1$. The latter trend is also found for shallow flows ($r_h > 3$). The dominance of the longitudinal coefficient for the supercritical flows, can be ascribed to the shearing of the anisotropic mean flow that, having streamwise size/intensity larger than the

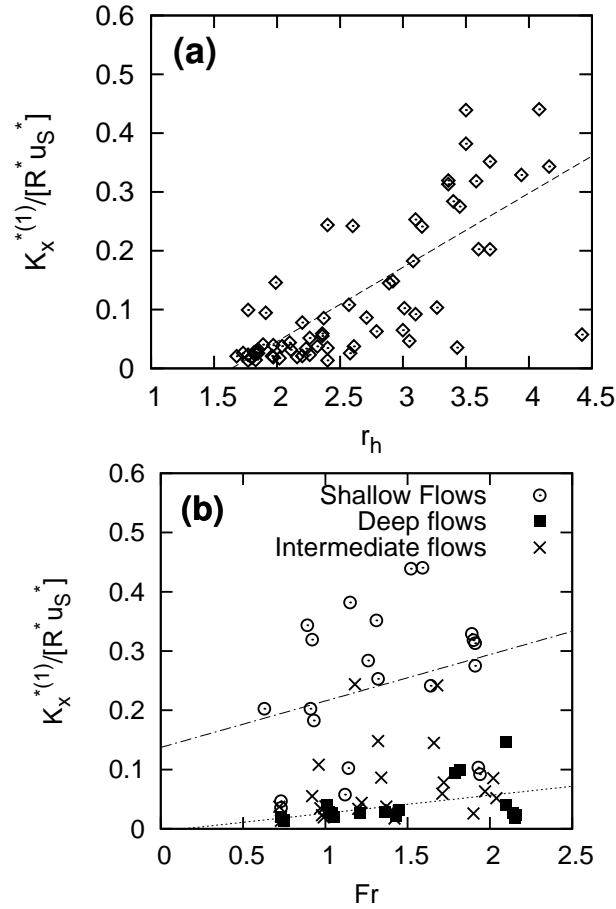


FIGURE 6.11: Dependence of the dimensionless absolute diffusivity $K_x^{*(1)}/u_S^* R^*$ on r_h (a) and Fr (b). Lines indicate linear regression of the data.

crossflow ones, dominates over the processes occurring at scales comparable to the macro-vortex size (i.e. crossflow size of the mean flow). In fact the turbulent energy balance of supercritical flows is characterized by a direct enstrophy cascade, rather than an inverse energy cascade typical of the subcritical flows [Stocchino et al., 2011].

The present measurements can also be compared with previous experimental campaigns. In figures 6.13 and 6.14 the present results for $K_x^{(1)}$ and $K_y^{(1)}$ are directly compared with several data from previous experimental campaigns.

Regarding $K_x^{(1)}$ in the streamwise direction we are able to measure only the contribution due to turbulent diffusion. In figure 6.13 only the data of Miller

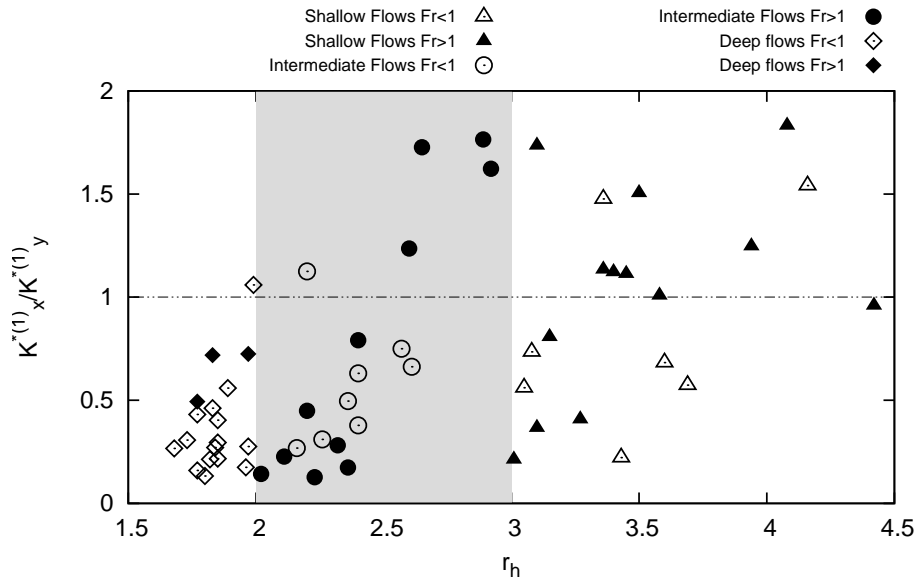


FIGURE 6.12: Dependence of the ratio $K_x^{*(1)}/K_y^{*(1)}$ on the flow depth ratio r_h . Gray shaded zone indicates intermediate flow conditions.

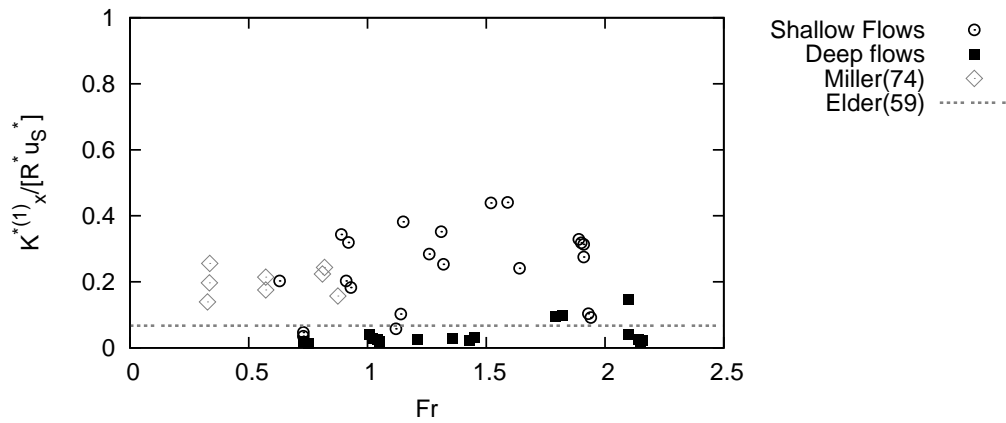


FIGURE 6.13: Dependence of $K_x^{*(1)}/u_s^* R^*$ on Fr , compared with available literature results.

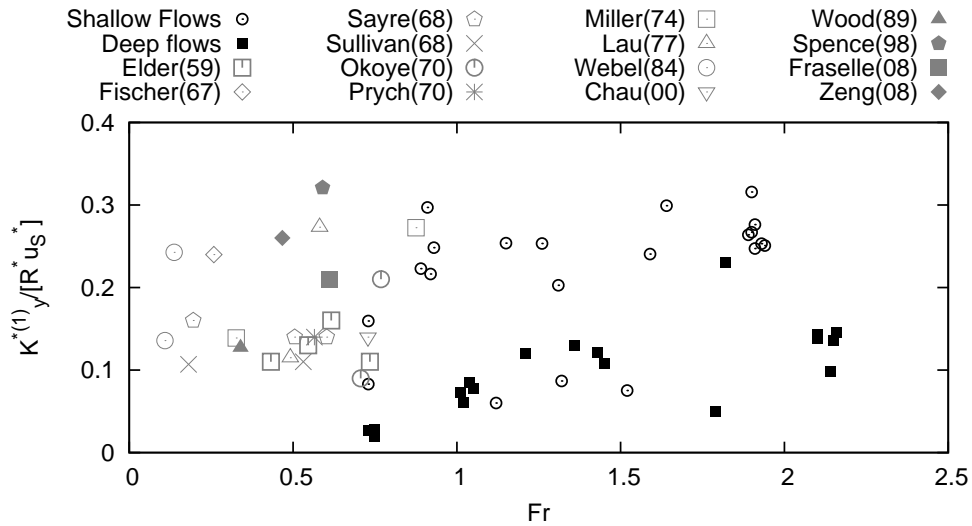


FIGURE 6.14: Dependence of $K_y^{*(1)}/u_s^*R^*$ on Fr , compared with available literature results. Gray markers: previous works, (empty for rectangular channel, fill for compound channels). Black markers: present campaign.

and Richardson [1974] are reported together with the theoretical prediction by Elder [1959]. Unfortunately, experimental data on the longitudinal turbulent diffusion are quite rare: the data of Miller and Richardson [1974] are the only available. Even if the present experiments have been performed with a different geometrical configuration (composite section rather than rectangular cross-section) and with a different roughness, much smoother than in Miller and Richardson [1974], the order of magnitude of the present measurements of $K_x^{(1)}$ well compares with that of the measurements by Miller and Richardson [1974], but, surprisingly, only for the shallow-flow cases. We expected the contrary to occur, since a rectangular flume cannot generate macro-vortices like in the case of shallow flows in a compound channel. A possible reason of the high values proposed by Miller and Richardson [1974] can be found in the roughness employed for the experiments, which may generate three-dimensional structures strongly affecting turbulent diffusion. The theoretical values predicted by Elder [1959] fall in between the values of shallow and deep

flows, being anyway closer to the latter flow conditions.

The results on the dependence of $K_y^{(1)}$ from Fr can be compared with various experimental results presented by several authors. Despite a noticeable scatter, all the literature values of $K_y^{(1)}$ coming from experiments made in rectangular flumes tend to be closer to the deep-flow cases of the present campaign. The higher values measured in rectangular-flume experiments might be due to the dependence on other flow conditions, in fact, even in previous experimental campaign it is possible to notice a quite large scatter in the outcomes for $K_y^{(1)}$ coefficient. The most evident influence on the results is due to the effect of the roughness present in the channel. For example, data obtained by Webel and Schatzmann [1984] and Lau and Krishnappan [1977] are pretty different from each other even if the value of the Froude number is almost the same. We should stress the fact that the present experimental campaign has been performed with a constant roughness, and the employment of different values of the latter could trigger different results as suggested by the range of the results obtained in previous laboratory experiments.

Other differences in the magnitude of the transversal mixing coefficient for previous campaign are due to different flow conditions in terms of velocities, hence of Froude number [a.o. Miller and Richardson, 1974], showing an increase in $K_y^{(1)}$ with Fr , as pointed out in the present analysis.

It is interesting to note that the few experiments concerning compound channel flows [Fraselle et al., 2008, Spence et al., 1998, Wood and Liang, 1989, Zeng et al., 2008] show a behaviour fairly similar to that observed in the present measurements. In fact, values of $K_y^{(1)}$ are smaller for deep flows [Fraselle et al., 2008, Wood and Liang, 1989] compared with shallow flows [Spence et al., 1998, Zeng et al., 2008], in qualitative agreement with our observations, though the values of $K_y^{(1)}$ that we find span over a wider range of the parameters than in the literature.

The results show that the values of the dispersion/diffusion coefficients, fundamental for many applications in water quality management, are mainly controlled by two physical parameters, namely the flow-depth ratio and the

Froude number. Based on the present measurements we have derived regressions for $K_x^{(1)}$ and $K_y^{(1)}$ in the $(r_h; Fr)$ -parameter space, that read:

$$\frac{K_x^{*(1)}}{R^*u_S^*} = -0.129 - 0.065Fr + 0.067r_h + 0.047Fr r_h, \quad (6.13)$$

$$R^2 = 0.648, \quad \text{err}_{var} = 0.0060$$

$$\frac{K_y^{*(1)}}{R^*u_S^*} = -0.188 + 0.131Fr + 0.094r_h - 0.023Fr r_h, \quad (6.14)$$

$$R^2 = 0.386, \quad \text{err}_{var} = 0.0057$$

where R^2 is the coefficient of determination of the regression and err_{var} is an estimate of the error variance. Notwithstanding the slightly low values of the R^2 , especially for $K_y^{*(1)}/R^*u_S^*$, which suggest a fairly variability in the data, relationships (6.13) and (6.14) can be easily implemented in 2D numerical models, taking into account the variations of flow depth ratio between the main channel and the floodplains and the overall flow regime.

Chapter 7

Conclusion

In the present research an extensive laboratory campaign has been dedicated to the analysis of the Lagrangian mixing in straight compound channels in quasi-uniform flow, for different conditions described by the values of the main physical parameters (i.e. the depth ratio r_h between water depth in main channel and floodplains and the Froude number Fr).

In a first stage, the experimental investigation based on PIV analysis of free-surface velocities has been made to reveal the fundamental features of the flow from the inception to the fully-developed flow conditions. Specific focus was on elucidating the properties of horizontal flow mixing governed by large-scale vortices with vertical axis generated in the transition region between main channel and floodplain. In this respect, the generation and evolution of macro-vortices in compound-channel flows are seen to strongly depend on the depth ratio r_h between water depth in main channel and floodplains.

For large values of the flow depth ratio ($r_h > 3$), i.e. in “Shallow Flows” conditions, the dominant flow features are the quasi-two dimensional vortical structures concentrated in the transition regions where the flow depth jump is localized. “Intermediate Flows” ($2 < r_h < 3$) are also characterized by a strong shearing at the transition region, with an intense peak of the time and x -averaged Reynolds stresses at that location, like the shallow flows and differently from the deep flows.

For low values of r_h (“Deep flows”), the free-surface velocity fields are characterized by a very weak cross-flow shearing at the transition regions; there almost no two-dimensional coherent macro-vortices observed, leaving only a low content of boundary vortices, caused by the shearing at the flume side-walls. In this case, the topographic forcing at the transition region is not effective in injecting a sufficient vorticity for the generation of the macro-vortices. Therefore, the mean shear at the transition region decreases with increasing Q and decreasing r_h and leads to the reduction of macro-vortices generation at the transition region and a simultaneous increase at the lateral walls. The macro-vortices radius clearly scaling with the crossflow extension of the transition region. Macro-vortices are not sensitive to the mean shear. The analysis has allowed us to point out similarities/difference between compound channel flow and true free shear flow. In this respect, a first difference is made evident by the mean flow profile in a compound channel. For most of the values of the depth ratio r_h , a non-monotonic profile characterizes the fully-developed flow. Hence, bell-type function, typically used as self-similar solutions for free shear layers Chu et al. [1991], van Prooijen and Uijttewaai [2002], is inadequate to represent the mean flow in a compound channel. Moreover, although horizontal mixing is governed by the quasi-2D macro-vortices in both flows, differences are expected, because the vortical structures of the two flows seem to have rather different properties. Such a difference is easily appreciated by inspecting the downstream growth of the dimension of the macro-vortices observed in the present experiments and those measured in free shear flows. While the former ones have a size almost constant, the latter ones grow in size at a considerable rate. Therefore, the global dynamics of a straight compound channel cannot be entirely explained by a shear layer approach i.e. the flow largely differs from that obtained by the meeting of three parallel streams of different velocity (fast stream in the main channel and two slow streams at the floodplains).

In the second part of the present work Lagrangian properties of the flow are analyzed, studying both the single- and multiple-particle statistics. The analysis has shown that, despite the apparent simplicity of the flow investigated, i.e. regular geometry and uniform flow conditions, the associated Lagrangian

mixing processes are rather complex and fundamentally controlled by two main parameters which are the flow depth ratio and Froude number.

For large values of the flow depth ratio ($r_h > 3$) macro-vortices strongly influence the total absolute dispersion (a^2) that is characterized by a non-monotonic growth with time in the regime intermediate between a small-time ballistic regime and an asymptotic Brownian regime. In particular, a local maximum is found, after the initial ballistic regime, for times comparable with the 2 to 3 times the mean turnover time. Decreasing r_h leads to a smoother growth of the total absolute dispersion with the classical asymptotic regimes predicted by Taylor [1921]. The macro-vortices are also responsible for an intense dispersion in the spanwise direction, yielding comparable values of the absolute diffusivities ($K_x^{(1)}$ and $K_y^{(1)}$), whereas the almost absence of long-lived coherent structures in the Deep flows leads to a stronger anisotropy.

As long as the transitional macro-vortices are the dominant flow features, the results obtained for the relative diffusivity $K^{(2)}$ reveal two distinct growth regimes as a function of the particle separation, for scales smaller than the injection length scale here coinciding with the size of the transition region, $K^{(2)}$ increases as it would for a direct enstrophy cascade process, whereas for scale larger than the injection scale $K^{(2)}$ increases at a rate compatible with an inverse energy cascade. The latter finding is supported by observations of vortex merging events in the case of Shallow flows.

For relatively low values of r_h , i.e. for Intermediate flows, the dynamics of particle pairs is strongly influenced by the flow intensity measured as function of a suitable Froude number. The dispersion regimes for subcritical Intermediate flows are in agreement with those obtained for Shallow flows (enstrophy cascade for $r < L_i$ and inverse energy cascade for $r > L_i$), whereas, once the Froude number is increased beyond the critical value of 1, the relative diffusivity is characterized by one single regime compatible with enstrophy cascading suggesting the dominance of large-scale shearing rather than of transitional macro-vortices.

Decreasing further the value of r_h , i.e. reaching the Deep flow conditions, since the topographic forcing is no longer effective in triggering the formation of the macro-vortices, one single regime is obtained for both subcritical and supercritical flows. The values of the exponent of the growth laws suggest the

presence of direct enstrophy cascade for $Fr > 1$, whereas for $Fr < 1$ direct energy cascade dominates the dynamics of mixing.

For the latter case, the distinction between the Richardson type mixing and shear dispersion, characterized by the same exponent of the growth of $K^{(2)}$, has been performed by analyzing the high-order moments of the Probability Density Functions of the separations. A value of the kurtosis close to 3 is related to a Gaussian distribution of the pair separation indicating that the subcritical Deep flows are characterized by a shear dispersion.

In a third stage, starting from the long-term behaviour of the absolute dispersion, diffusivity coefficients are computed. The results suggest that both $K_x^{(1)}$ and $K_y^{(1)}$ monotonically increase with the decrease of the flow depth, i.e. for increasing r_h . This can be associated to the generation of 2D macrovortices that are mainly observed at the transition region, where the flow-depth jump between the main channel and the floodplains is located. The macrovortices are responsible for an increased non-uniformity of the surface Eulerian velocity field and, thus, of the Lagrangian particle trajectories, leading to higher mixing coefficients. On the contrary, in the deep-flow condition the free-surface velocity fields are more uniform, yielding lower values of the coefficients. In particular, the longitudinal turbulent diffusivity is much lower than the transversal coefficient. The anisotropy of the coefficient is, in this case, rather pronounced.

Plotting the same results as function of the Froude number, displays, again, a monotonic growth of the mixing coefficients with Fr . However, deep and shallow flows are clearly separated and the latter ones, for the same Froude number, are always characterized by larger values of both $K_x^{(1)}$ and $K_y^{(1)}$. Intermediate flows are placed between the two limiting cases.

A comparison between the present results and several previous data has been performed for the transversal mixing coefficient and, whenever possible, also for the longitudinal turbulent coefficient. Regarding $K_y^{(1)}$, most of the measurements have been obtained in flume experiments with rectangular cross-sections, which should be closer to the deep-flow condition of the present analysis. Indeed, despite a considerable scatter, on average the previous data fit better with the deep flow cases. Coherently, the experiments performed

with non-rectangular cross-sections show a behavior similar to the one observed in the present experimental campaign.

Regressions for the mixing coefficients $K_x^{(1)}$ and $K_y^{(1)}$ have been provided, retaining the dependence on both the flow depth ratio and the Froude number. These relationship might be of interest for numerical simulations based on the shallow-water advection diffusion equation applied to several applications of water quality management.

Results on diffusivities are proposed to satisfy both theoretical and practical modeling purposes, i.e. those of: i) collecting information to be compared with recent theoretical studies that focus on the differences existing in mixing processes between the main channel and the floodplains, with diffusivities depending on flow regimes and transversal location, i.e. main channel and floodplains, and ii) producing synthetic data to be used in practical, simplified computations of mixing that make use of one single overall value of diffusivity for the entire flow cross-section. The latter approach is still very much used once numerical simulation and evaluation for practical problems, such those faced by environmental engineering, are performed.

Appendix A

Lagrangian and Eulerian integral quantities of the whole set of experiments

TABLE A.1: Relevant Lagrangian and Eulerian integral quantities of the whole set of experiments

Exp. Name	r_h [-]	Fr [-]	E_L^* [m ² /s ²]	T_{uL}^* [s]	T_{vL}^* [s]	L_{uL}^* [m]	L_{vL}^* [m]	E_E^* [m ² /s ²]	T_{uE}^* [s]	T_{vE}^* [s]	T_T [-]
<i>Shallow flows</i>											
EXP101	3.69	0.88	0.001126	4.0206	0.4421	0.1349	0.0148	0.001427	4.1507	0.4904	0.0950
EXP102	3.23	0.91	0.001364	3.8013	0.3188	0.1404	0.0118	0.001699	3.9274	0.4190	0.1090
EXP04	3.69	0.87	0.001316	1.2488	0.1684	0.0453	0.0061	0.001414	4.1766	0.2690	0.2908
EXP06.1	3.10	0.92	0.001241	1.2396	0.1465	0.0437	0.0052	0.001401	4.0331	0.1585	0.3257
EXP010	4.42	0.73	0.000943	1.2340	0.2160	0.0379	0.0066	0.001019	4.3962	0.6238	0.2767
EXP011	3.50	0.77	0.001438	0.8759	0.1901	0.0332	0.0072	0.001656	4.0856	0.3379	0.3910
EXP012	3.40	0.80	0.001264	1.3119	0.1995	0.0466	0.0071	0.002280	4.0648	0.4022	0.2113
EXP201	4.16	0.60	0.000399	3.4787	0.3684	0.0694	0.0074	0.000504	11.0929	1.4211	0.1737
EXP202	3.60	0.62	0.000409	3.1638	0.3600	0.0640	0.0073	0.000549	10.8788	1.3098	0.2005
EXP203	3.36	0.64	0.000440	3.3460	0.4185	0.0702	0.0088	0.000529	10.8231	1.1654	0.1948
EXP204	3.08	0.65	0.000458	3.1524	0.4492	0.0675	0.0096	0.000584	10.5168	1.2757	0.2163
EXP001	3.69	0.44	0.000202	1.5931	0.7407	0.0226	0.0105	0.000241	8.2112	0.9079	0.6346
EXP002	3.43	0.46	0.000091	2.0198	0.9157	0.0192	0.0087	0.000079	9.1400	1.8571	0.4587
EXP003	3.05	0.47	0.000090	2.8517	0.7300	0.0271	0.0069	0.000076	9.0556	1.3710	0.3272
<i>Intermediate flows</i>											

Continued on next page

Table A.1 – *Continued from previous page*

Exp. Name	r_h [-]	Fr [-]	E_L^* [m ² /s ²]	T_{uL}^* [s]	T_{vL}^* [s]	L_{uL}^* [m]	L_{vL}^* [m]	E_E^* [m ² /s ²]	T_{uE}^* [s]	T_{vE}^* [s]	T_T [-]
EXP103	2.62	0.97	0.000505	4.3555	0.5117	0.0979	0.0115	0.000598	4.4370	0.5327	0.0944
EXP104	2.29	1.03	0.000435	4.2171	0.8945	0.0880	0.0187	0.000533	4.2865	0.7623	0.1082
EXP105	2.15	1.05	0.000504	4.0335	0.8769	0.0906	0.0197	0.000621	4.1102	0.5530	0.1186
EXP106	2.07	1.07	0.000631	3.0521	0.6168	0.0767	0.0155	0.000757	3.1571	0.4383	0.1418
EXP107	2.03	1.07	0.000624	2.9748	0.6405	0.0743	0.0160	0.000761	3.1010	0.4217	0.1487
EXP06.6	2.92	0.94	0.000975	1.4206	0.1014	0.0444	0.0032	0.001045	4.1898	0.1399	0.2883
EXP07	2.71	0.96	0.000627	1.8842	0.1332	0.0472	0.0033	0.000639	4.4087	0.1899	0.2146
EXP10	2.32	1.02	0.000481	1.7625	0.3171	0.0386	0.0070	0.000968	4.3356	0.5746	0.2590
EXP12	2.11	1.06	0.000496	1.6093	0.4772	0.0358	0.0106	0.000619	3.2908	0.3588	0.2628
EXP13	2.02	1.07	0.000668	1.5634	0.5063	0.0404	0.0131	0.001302	3.0648	0.3298	0.2606
EXP013	2.36	0.84	0.000347	2.4633	0.2385	0.0459	0.0044	0.000436	4.5913	1.0029	0.1506
EXP014	2.30	0.87	0.000409	1.6821	0.2518	0.0340	0.0051	0.000417	3.0060	0.6953	0.2161
EXP015	2.10	0.92	0.000727	1.3271	0.2075	0.0358	0.0056	0.000738	2.6511	0.6265	0.2850
EXP205	2.57	0.69	0.000367	3.6030	0.3118	0.0691	0.0060	0.000417	10.8472	1.3190	0.1949
EXP206	2.40	0.71	0.000321	3.0163	0.2016	0.0541	0.0036	0.000377	5.6998	0.9195	0.2230
EXP207	2.26	0.73	0.000326	2.6958	0.2093	0.0487	0.0038	0.000392	4.2514	0.6814	0.2433
EXP208	2.16	0.74	0.000340	2.6557	0.2684	0.0489	0.0049	0.000399	4.1548	0.5984	0.2496

Continued on next page

Table A.1 – *Continued from previous page*

Exp.	r_h	Fr	E_L^*	T_{uL}^*	T_{vL}^*	L_{uL}^*	L_{vL}^*	E_E^*	T_{uE}^*	T_{vE}^*	T_T
Name	[-]	[-]	[m ² /s ²]	[s]	[s]	[m]	[m]	[m ² /s ²]	[s]	[s]	[-]
EXP209	2.04	0.76	0.000361	2.5942	0.1990	0.0493	0.0038	0.000437	4.1062	0.6083	0.2552
EXP004	2.61	0.50	0.000112	2.4703	0.3950	0.0261	0.0042	0.000099	4.3513	0.2518	0.3325
EXP005	2.40	0.51	0.000106	2.3586	0.2538	0.0242	0.0026	0.000091	4.1502	0.3021	0.3387
EXP006	2.20	0.53	0.000119	2.0601	0.2515	0.0225	0.0027	0.000117	3.7111	0.2777	0.3995
<i>Deep flows</i>											
EXP108	1.95	1.09	0.000742	2.8216	0.5657	0.0769	0.0154	0.000900	2.9520	0.3239	0.1591
EXP109	1.86	1.11	0.000764	2.5225	0.5872	0.0697	0.0162	0.000957	2.7497	0.2755	0.1759
EXP110	1.82	1.12	0.000818	2.4143	0.4879	0.0691	0.0140	0.001028	2.6479	0.2394	0.1848
EXP112	1.28	0.14	0.000128	8.0753	0.3181	0.0913	0.0036	0.000179	12.5836	0.7280	0.1220
EXP14	1.96	1.09	0.000695	1.4211	0.4231	0.0375	0.0112	0.000793	3.0008	0.2512	0.3005
EXP16	1.85	1.15	0.000912	1.4239	0.4231	0.0430	0.0128	0.002154	2.6424	0.2549	0.2644
EXP17	1.82	1.13	0.000783	1.2175	0.5089	0.0341	0.0142	0.000931	2.6143	0.2634	0.3558
EXP017	1.85	0.96	0.001136	1.0174	0.1556	0.0343	0.0052	0.001226	2.4007	0.3511	0.3331
EXP018	1.82	0.99	0.001548	1.0888	0.1254	0.0428	0.0049	0.001954	2.2659	0.3117	0.3155
EXP210	1.89	0.78	0.000471	2.5864	0.2111	0.0561	0.0046	0.000568	3.8975	0.5730	0.2534
EXP211	1.83	0.79	0.000510	2.6535	0.1903	0.0599	0.0043	0.000606	3.8099	0.3809	0.2451
EXP212	1.73	0.81	0.000599	2.5977	0.2091	0.0636	0.0051	0.000716	3.6902	0.4447	0.2454

Continued on next page

Table A.1 – *Continued from previous page*

Exp.	r_h	Fr	E_L^*	T_{uL}^*	T_{vL}^*	L_{uL}^*	L_{vL}^*	E_E^*	T_{uE}^*	T_{vE}^*	T_T
Name	[-]	[-]	[m ² /s ²]	[s]	[s]	[m]	[m]	[m ² /s ²]	[s]	[s]	[-]
EXP213	1.68	0.82	0.000679	2.4911	0.2051	0.0649	0.0053	0.000828	3.5203	0.2990	0.2555
EXP007	1.97	0.55	0.000172	1.9276	0.1437	0.0253	0.0019	0.000172	3.6659	0.2271	0.3799
EXP008	1.83	0.56	0.000263	1.5502	0.0985	0.0251	0.0016	0.000406	3.0661	0.1658	0.4369
EXP009	1.77	0.57	0.000319	1.7301	0.1325	0.0309	0.0024	0.000801	2.6982	0.1471	0.2556

Bibliography

- Adrian, R., Christensen, K., and Liu, Z. (2000). Analysis and interpretation of instantaneous turbulent velocity fields. *Exp. in Fluids*, 29:275–290.
- Arnold, U., Hottges, J., and Rouv, G. (1989). Turbulence and mixing mechanisms in compound open channel flow. In *Proc. 23rd IAHR Congress*, pages A–133 – A–140, Ottawa, Canada. IAHR.
- Babiano, A., Basdevant, C., Le Roy, P., and Sadourny, R. (1987). Single-particle dispersion, lagrangian structures function and lagrangian energy spectrum in two-dimensional incompressible turbulence. *J. Mar. Res.*, 45:107–131.
- Babiano, A., Basdevant, C., Le Roy, P., and Sadourny, R. (1990). Relative dispersion in two-dimensional turbulence. *J. Fluid Mech.*, 214:535–557.
- Batchelor, G. (1969). Computation of the energy spectrum in homogeneous two-dimensional turbulence. *Phys. Fluids Suppl.*, II 12:233–239.
- Bennett, A. (1984). Relative dispersion: Local and nonlocal dynamics. *J. Atm Sc.*, 41:1881–1886.
- Bennett, A. (1987). A lagrangian analysis of turbulent diffusion. *Rev. Geophys.*, 4:799–822.
- Boffetta, G., Lacorata, G., Redaelli, G., and Vulpiani, A. (2001). Detecting barriers to transport: A review of different techniques. *Physica D*, 159:58–70.

- Bousmar, D., Proust, N. R. S., Paquier, A., Morel, R., and Zech, Y. (2005). Upstream discharge distribution in compound-channel flumes. *J. Hydraulic. Eng. ASCE*, 131(5):1408–1413.
- Chau, K. (2000). Transverse mixing coefficient measurements in an open rectangular channel. *Advances in Environmental Research*, 4(4):287–294.
- Chu, V., Wu, J., and Khayat, R. (1991). Stability of transverse shear flow in shallow open channels. *J. Hydr. Engng*, 117(10):1370–1388.
- Davis, R. (1982). On relating eulerian and lagrangian velocity statistics: single particles in homogeneous flows. *J. Fluid Mech.*, 114:1–26.
- Davis, R. (1983). Oceanic property transport, lagrangian particle statistics and their prediction. *J. Mar. Res.*, 41:163–194.
- Deng, Z., Singh, V., and Bengtsson, L. (2001). Longitudinal dispersion coefficient in straight rivers. *Journal of Hydraulic Engineering*, 127(11):919–927.
- Elder, J. (1959). The dispersion of marked fluid in turbulent shear flow. *Journal of Fluid Mechanics*, 5(04):544–560.
- Elhmaïdi, D., Provenzale, A., and Babiano, A. (1993). Elementary topology of two-dimensional turbulence from a lagrangian viewpoint and single-particle dispersion. *J. Fluid Mech.*, 257:533–558.
- Er-El, J. and Peskin, R. (1981). Relative diffusion of constant-level balloons in the suthern hemisphere. *J. Atm Sc.*, 38:2264–2274.
- Fischer, H. (1975). Discussion of "simple method for predicting dispersion in streams". *Journal of the Environmental Engineering Division*, 101(3):453–455.
- Fischer, H., List, E., Koh, R., Imberger, J., and Brooks, N. (1979). *Mixing in inland and coastal waters*. Academic Press.
- Fraselle, Q., Arnould, T., Lissoir, X., Bousmar, D., and Zech, Y. (2008). Investigating diffusion and dispersion in compound channels using low-cost tracer. In *Proc. River Flow 2008 Int. Conf. on Fluvial hydraulics*, pages 529–538, Cesme, Turkey.

- Ghidaoui, M. and Kolyshkin, A. (1999). Linear stability analysis of lateral motions in compound open channels. *Journal of Hydraulic Engineering, ASCE*, 125 (8):871–880.
- Guala, M., Liberzon, A., Tsinober, A., and Kinzelbach, W. (2007). An experimental investigation on lagrangian correlations of small-scale turbulence at low reynolds number. *J. Fluid Mech.*, 574:405–427.
- Guymer, I. and Spence, K. (2009). Laboratory study of transverse solute mixing during over-bank flows. In *Proc. of 33rd IAHR Congress: Water Engineering for a Sustainable Environment*.
- Holley, E. and Abraham, G. (1973). Field tests of transverse mixing in rivers. *Journal of the Hydraulics Division*, 99(12):2313–2331.
- Hua, B. L. and Kline, P. (1998). An exact criterion for the stirring properties of nearly two-dimensional turbulence. *Physica D*, 113(1):98–110.
- Jirka, G. (2001). Large scale flow structures and mixing processes in shallow flows. *J. Hydr. Res.*, 39:567–573.
- Knight, D. and Hamed, M. (1984). Boundary shear in symmetrical compound channel. *Journal of the Hydraulics Division, ASCE*, 110 (10):1412–1430.
- Knight, D. and Sellin, R. (1987). The serc flood channel facility. *Journal of the Institution of Water and Environmental Managment*, 1 (2):198–204.
- Knight, D. and Shiono, K. (1990). Turbulence measurements in a shear layer region of a compound channel. *Journal of Hydraulic Research, IAHR*, 28 (2):6141–156.
- Kraichnan, H. (1966). Dispersion of particle pairs in homogeneous turbulence. *Phys. Fluids*, 9:1937–1943.
- Kraichnan, H. (1967). Inertial ranges of two dimensional turbulence. *Phys. Fluids*, 10:1417–1423.
- Kraichnan, H. (1976). Eddy viscosity in two and three dimensions. *J. Atmos. Sci.*, 33:1521–1536.

- LaCasce, J. (2008). Statistics from lagrangian observations. *Progress in Oceanography*, 77:129.
- Lau, Y. L. and Krishnappan, B. G. (1977). Transverse dispersion in rectangular channels. *Journal of the Hydraulics Division*, 103(10):1173–1189.
- Leith, C. (1968). Diffusion approximation for two-dimensional turbulence. *Phys. Fluids*, 11:671–673.
- Lekien, F., Coulliette, C., Mariano, A., Ryan, E., Shay, L., Haller, G., and Marsden, J. (2005). Pollution release tied to invariant manifolds: A case study for the coast of florida. *Physica D: Nonlinear Phenomena*, 210(1-2):1–20.
- Lesieur, M. (1990). *Turbulence in Fluids*. Kluwer Academic Publishers, Dordrecht.
- Lin, J. (1972). Relative dispersion in the enstrophy cascading inertial range of homogeneous two dimensional turbulence. *J. Atmos. Sci.*, 29:394–396.
- Luo, J., Ushijima, T., Kitoh, O., Lu, Z., and Liu, Y. (2007). Lagrangian dispersion in turbulent channel flow and its relationship to eulerian statistics. *Int. J. Heat and Fluid Flow*, 28:871–881.
- Manson, J. R. and Wallis, S. G. (2004). Fluvial mixing during floods. *Geophysical Research Letters*, 31(14):L14502.
- Melander, M., Zabusky, N., and McWilliams, J. (1988). Symmetric vortex merger in two dimension: causes and condition. *J. Fluid Mech.*, 195:303–340.
- Meyer, L. and Rehme, K. (1994). Large scale turbulence phenomena in compound rectangular channels. *Experimental Thermal and Fluid Science, Elsevier Science, New-York*, 8:286–304.
- Miller, A. and Richardson, E. (1974). Diffusion and dispersion in open channel flow. *Journal of the Hydraulics Division*, 100(1):159–171.
- Mobbs, F. (1968). Spreading and contraction at flows. *J. Fluid Mech.*, 33:227–240.

- Myers, W. (1978). Momentum transfer in a compound channel. *Journal of Hydraulic Research, IAHR*, 16 (2):139–150.
- Myers, W. and Brennan, E. (1990). Flow resistance in compound channels. *Journal of Hydraulic Research, IAHR*, 28 (2):141–155.
- Myers, W. and Elsayy, E. (1975). Boundary shear in channel with flood plain. *Journal of the Hydraulics Division, ASCE*, 101 (7):933–946.
- Nezu, I. and Nakagawa, H. (1997). Space-time correlation structures of horizontal coherent vortices in compound open-channel flows by using particle-tracking velocimetry. *Journal of Hydraulic Research, IAHR*, 35 (2):191–208.
- Nezu, I., Onitsuka, K., and Iketani, K. (1999). Coherent horizontal vortices in compound open channel flows. In Singh, V. P., Seo, I. W., and Sonu, J. H., editors, *Hydraulic Modeling*, pages 17–32. Water Resources Pub.
- Nikora, V., Nokes, R., Veale, W., Davidson, M., and Jirka, G. (2007). Large-scale turbulent structure of uniform shallow free-surface flows. *Environ Fluid Mech.*, 7:159–172.
- Nokes, R. I. and Wood, I. R. (1988). Vertical and lateral turbulent dispersion: Some experimental results. *Journal of Fluid Mechanics*, 187:373–394.
- Okoye, J. (1970). Characteristics of transverse mixing in open-channel flows. Technical report, California Institute of Technology, Pasadena, California, USA.
- Okubo, A. (1970). Horizontal dispersion of floatable particles in the vicinity of velocity singularities such as convergences. *Deep-Sea Res.*, 17:445–454.
- Piattella, A., Brocchini, M., and Mancinelli, A. (2006). Topographically-controlled, breaking wave-induced macrovortices. part 3. the mixing features. *J. Fluid Mech.*, 559:81–106.
- Provenzale, A. (1999). Transport by coherent barotropic vortices. *Ann. Rev. Fluid Mech.*, 31:55–93.

- Raffel, M., Willert, C., and Kompenhans, J. (1998). *Particle image velocimetry, a practical guide*. Springer, Berlin Heidelberg New York.
- Rutherford, J. C. (1994). *River mixing*. Wiley.
- Sellin, R. (1964). A laboratory investigation into the interaction between the flow in the channel of a river and that over its flood plain. *La Houille Blanche*, 7:793–802.
- Seo, I. and Cheong, T. (1998). Predicting longitudinal dispersion coefficient in natural streams. *Journal of Hydraulic Engineering*, 124(1):25–32.
- Shiono, K. and Knight, D. (1991). Turbulent open-channel flows with variable depth across the channel. *J. Fluid Mech.*, 222:617–646.
- Socolofsky, S. and Jirka, G. (2004). Large-scale flow structures and stability in shallow flows. *J. Environ. Eng.Sci.*, 3:451–462.
- Soldini, L., Piattella, A., Brocchini, M., Mancinelli, A., and Bernetti, R. (2004). Macrovortices-induced horizontal mixing in compound channels. *Ocean Dyn.*, 54:333–339.
- Spence, K., Guymer, I., West, J., and Sander, B. (1998). Transverse mixing of solute and suspended sediment from a river outfall during over-bank flow. In *Proc. of 7th Int. Symp. on River Sedimentation and 2nd Int. Symp. on Environmental Hydraulics*, pages 363 – 368, Hong Kong, China.
- Spence, K., Potter, R., and Guymer, I. (1997). Transverse solute mixing from river outfalls during overbank flows. In *Proc. 3rd Int. Conf. on River Flood Hydraulics*, pages 485 – 494, South Africa, 485 - 494. HR Wallingford Ltd.
- Stephenson, D. and Kolovopoulos, P. (1990). Effects of momentum transfer in compound channels. *J. Hydraulic. Eng. ASCE*, 116:1512–1522.
- Stocchino, A., Besio, G., Angiolani, S., and Brocchini, M. (2011). Lagrangian mixing in straight compound channel. *J. Fluid Mech.*, 675:168–198.
- Stocchino, A. and Brocchini, M. (2010). Horizontal mixing of quasi-uniform, straight, compound channel flows. *J. Fluid Mech.*, 643:425–435.

- Tabeling, P. (2002). Two-dimensional turbulence: a physicist approach. *Physics Report*, 362:1–62.
- Taylor, G. (1921). Diffusion by continuous movement. *Proc. Lond. Math. Soc.*, 20:196–212.
- van Prooijen, B. and Uijttewaal, W. (2002). A linear approach for the evolution of coherent structures in shallow mixing layers. *Phys. Fluids*, 14(12):4105–4114.
- Webel, G. and Schatzmann, M. (1984). Transverse mixing in open channel flow. *Journal of Hydraulic Engineering*, 110(4):423.
- Weiss, J. (1991). The dynamics of enstrophy transfer in two-dimensional hydrodynamics. *Physica D*, 48:272–294.
- Wood, I. R. and Liang, T. (1989). Dispersion in an open channel with a step in the cross-section. *Journal of Hydraulic Research*, 27(5):587–601.
- Wormleaton, P. and Merrett, D. (1990). An improved method of the calculation for steady uniform flow in prismatic main channel/flood plain sections. *Journal of Hydraulic Research, IAHR*, 28 (2):157–174.
- Zeng, Y., Huai, W., and Guymer, I. (2008). Transverse mixing in a trapezoidal compound open channel. *Journal of Hydrodynamics, Series B*, 20(5):645–649.

Acknowledgements

I would like to express my special appreciation and thanks to my supervisors. I am indebted to Dr. Alessandro Stocchino for giving me this opportunity and for encouraging my research. I am deeply grateful to Dr. Giovanni Besio for guiding me, without his persistent help, support and incitements this thesis would not have been possible. I would like to express my gratitude to Prof. Ian Guymer for accepting to read my work, his careful review has been useful and precious for the final version of my thesis. I would also to thank all the Professors of the Department of Civil, Chemical and Environmental Engineering, who have always given me time, material and suggestions.

Ed eccoci finalmente a scrivere queste ultime righe. Non è stato facile arrivarci. Le salite, i passi indietro e la mancanza di fiducia che potesse davvero esistere questo lavoro hanno reso il percorso lungo e faticoso. Ma ci siamo, ed è anche con un po' di nostalgia che mi lascio indietro questa intensa ed importante esperienza.

Il primo grazie va ai miei compagni di viaggio. Marco, il primo con cui ho iniziato il cammino. Con il tuo entusiasmo e la tua voglia di fare mi hai aiutata e nonostante le incomprensioni mattutine il tuo brava in un momento difficile mi ha aiutata ad alzare la testa "solo i compagni di cordata sanno quanto è dura la montagna", sono sicura che tu con il tuo "fuoco" potrai davvero scalare ogni vetta.

Chiara, con te ho iniziato questa avventura ed insieme abbiamo vissuto il primo convegno, le prime trasferte ed i giorni più intensi e duri di tutto il dottorato, avrei davvero voluto arrivare al traguardo insieme.

Julia, vicino a me nei giorni più importanti di tutto il viaggio, hai riempito il cammino di risate, parole del giorno, caffè per staccare la testa e passioni da inseguire.

Ed eccoci ad Andrea sicura che, essendoti già stufato di leggere questa pagina, non sarai neppure arrivato a leggere il tuo nome...Grazie perchè sei tu quello che mi ha raccolto sempre da "under the table" nei momenti più bui del cammino. Grazie perchè hai da sempre cercato di convincermi che sono in gamba

e sei stato il miglior compagno di sfoghi e caffè. Mi mancheranno le nostre diversità, le nostre chiacchiere ed i nostri confronti. Mattia, Manny, l'ultimo della lista, ma l'amico che ha condiviso con me tutto. Dalle mie mattinate post notti insonni, dalle mie lacrime nascosta in cucina ai mie sfoghi di non potercela fare. E tutto sempre con un'attenzione ed una presenza che solo un vero amico può dedicarti. Oggi siamo qui, siamo insieme, ed insieme ci mettiamo sulle spalle questo zaino e cominciamo il vero viaggio.

Grazie a voi bimbe. Ovunque il futuro mi porterà voi sarete accanto a me ogni giorno. Grazie per ogni buongiorno, per ogni parola di incoraggiamento, per ogni abbraccio e per ogni risata. Ognuna di voi ha fatto un'inestimabile differenza in questo mio viaggio. Grazie perchè crediamo e abbiamo fiducia l'una nell'altra. Ogni successo, ogni traguardo è di tutte noi.

Rita, Anita, Sarah e Caterina...stiamo crescendo e farlo accanto a voi rende tutto più semplice. Grazie perchè nessuno come voi è stato in grado di capirmi, aiutarmi, sorreggermi e correggermi ad ogni passo indietro.

Papà, mamma. Sono arrivata a questo traguardo e anche se ho cominciato a camminare un po' più da sola so che voi siete sempre alle mie spalle pronti a sorreggermi, a farmi andare avanti quando decido di fermarmi, capaci di risolvere ogni mio piccolo problema. Grazie, come sempre, per esserci e per essere dei meravigliosi nonni oltre che genitori.

Valentina, perchè da te ogni giorno imparo come si può raggiungere qualunque vetta ed insieme essere una mamma meravigliosa, dolce e forte. Filippo ed Emanuele, 'Chio e Meme', la gioia più bella che potessi mai regalarmi.

Non potrò mai smettere di ringraziare Andrea, Tommaso e Luisa. Siete la mia famiglia. Mi avete sorretto, avete creduto in me ed aiutato con il vostro affetto. E grazie ancora a Luisa per il dono di essere diventata zia di una cucciola meravigliosa...sono sicura che insieme riusciremo a realizzare i nostri desideri. Mari, sei accanto a noi ad ogni nostro passo, ad ogni difficoltà e sei presente in tutte le nostre gioie. Sei con me anche oggi.

Marzio. È a te che dedico questo traguardo. Sei da sempre il mio punto di riferimento, mio esempio, fratello maggiore ed amico. A te mi sono appoggiata quando avrei voluto mollare e tu sei stato capace di farmi alzare la testa e stringere i denti. Questa tesi non esisterebbe senza le ore a parlare con te. Ed infine Matteo, ti devo tutto. Ancora un traguardo con te al mio fianco.

*Hai asciugato ogni mia lacrima, hai creduto in me ogni giorno, fin dai primi “non posso farcela” fino agli ultimi “cosa sarà di me”. Mi aiuti e mi sorreggi ogni istante della mia vita, grazie per ogni singolo “sono orgoglioso di te”.
Martina, hai dato un senso alla mia vita, da quando scappavo da te con il pensiero e tu eri già con me. Sei la ragione di ogni mio giorno.*